

Highly Accelerated MRI:  
Prior Data Assisted Compressed Sensing for Lung Tumour Tracking

by  
Eugene Yip

A thesis submitted in partial fulfillment of the requirements for the degree of

Doctor of Philosophy

in

Medical Physics

Department of Oncology  
University of Alberta

© Eugene Yip, 2017

## Abstract

Hybrid magnetic resonance imaging (MRI) and radiation therapy devices are capable of imaging in real-time to track intrafractional lung tumour motion during radiotherapy. In the real time tumour tracking treatment scheme, MR images are acquired in real time, then the tumour target is localized using an automatic contouring algorithm, allowing the radiation beam to follow the moving tumour. Highly accelerated magnetic resonance (MR) imaging methods can yield large increases in acquisition speed at the cost of some increase in reconstruction time. If employed effectively, they can potentially reduce system delay time and/or improves imaging spatial resolution, provide flexibility in imaging parameters and allow for the imaging of multiple slices without reducing frame rate.

The aim of this thesis is to develop and validate an MR acceleration strategy which can be used to improve real time tumour tracking. First, an in-house tumour auto-contouring software is validated against a gold standard in both phantom and patient data. Once validated, the auto-contouring algorithm is used to validate the MR acceleration strategy developed.

The novel MR acceleration strategy, Prior Data Assisted Compressed Sensing (PDACS), combines the advantages of 2D compressed sensing and the view-sharing strategy. Like 2D compressed sensing, it uses L1 regularization to reconstruct images from undersampled k-space. However, the acceleration achievable with 2D-CS is quite limited, as the line-by-line data acquisitions restricts random sampling to only the phase encode direction in k-space. PDACS, improves the reconstruction by adding previously acquired, motion averaged data into the CS reconstruction via an additional penalty term. Our results have shown that this method is superior to 2D-CS, in terms of reduced artifact power and improved tumour tracking metrics.

However, PDACS relies on prior data acquired at the beginning of a dynamic imaging sequence, and thus is dependent on the stability of the baseline MR signal. For shorter duration (i.e. 1 minute) dynamic scans, PDACS is shown to be adequate. However, for longer duration scans (3 minutes), PDACS results in a gradual decline in image quality due to drifts in MR signal. An improved implementation, sliding window PDACS, varies the sampling pattern and allows for “prior data” to be continuously refreshed. Using this improved implementation, sliding window PDACS is shown to successfully remove the negative effect of signal drifts from longer scans.

## Acknowledgements

First and foremost, I would like to thank my family, especially my mother, who has provided me with love and support for so many years; and Natalie Hilbrecht - I am truly fortunate to have her by my side.

Next, I would like to acknowledge my supervisor, Gino Fallone, who provided me with this unique research opportunity with his vision in the linac-MR project, which will undoubtedly lead to a device that will make a significant impact to improve lives of cancer patients. I am also grateful to my co-supervisors, Satyapal Rathee and Keith Wachowicz for providing me with invaluable guidance and advice. I would also like to acknowledge the other members of my committee: Nick De Zanche, Atiyah Yayha and Richard Thompson for contributing their knowledge and expertise. I would also like to thank Ron Sloboda for chairing my candidacy and final exams, and Steven Beyea of Dalhousie University for providing valuable feedback for this work.

I would like to acknowledge all my collaborators, especially Jay Yun, with whom I have shared co-authorship in 5 publications thus far. I would also like to acknowledge the radiation oncologists I collaborated with: Zsolt Gabos, Sarah Baker and Don Yee. I am grateful for the wonderful team of medical physicists at the Cross Cancer Institute who have taught me so much. Additionally, I would like to thank the administrators, IT staff and machinists for all of their assistance through my degree.

I would also like to acknowledge the many current and former student colleagues in the medical physics department, for providing me with advice, insights and much laughter. In particular, many stimulating discussions with Amr Heikal have helped formulate some of key ideas behind this thesis. It has been a pleasure to have the wonderful comradery with Andrei Ghila, Hali Morrison, Danielle Anderson, Devin Baillie, Simon Ferguson, Shima Yaghoobpour Tari, Dong Chang Lee, Katie Gagnon, Moti Raj Paudel, Dan Michael Santos, Jean David Jutras, Brie Cawston-Grant, Mike Reynolds, Brian Morrell, Brendan Dobberthien, Radim Bartra and many others.

Finally, I would like to acknowledge the Canadian Institute of Health Research, the Alberta Innovates-Health Solutions and the Killam Trusts, for their generous financial support.

# Table of Content

<b>Abstract .....</b>	<b>ii</b>
<b>Acknowledgements .....</b>	<b>iii</b>
<b>Table of Content .....</b>	<b>iv</b>
<b>List of Tables .....</b>	<b>xi</b>
<b>List of Figures .....</b>	<b>xii</b>
<b>List of Acronyms .....</b>	<b>xx</b>
<b>Chapter 1 Introduction .....</b>	<b>1</b>
1.1 Background .....	1
1.2 Modern Radiation Therapy .....	2
1.2.1 Target Volumes – Basic Definitions .....	2
1.3 Image Guidance in Radiation Therapy.....	4
1.3.1 Image Guidance Based on 2D Imaging and Fiducial Markers.....	5
1.3.2 Image Guidance by Direct Imaging of Soft Tissues.....	5
1.3.3 Linac-MR Hybrid Systems .....	7
1.4 Respiratory Motion in Radiation Therapy .....	8
1.4.1 Encompassing the Entire Volume of Motion (ITV).....	9

1.4.2 Breath-hold Methods .....	10
1.4.3 Gating Methods .....	10
1.4.4 Tumour Tracking Methods.....	11
1.5 Real Time Tumour Localization .....	12
1.5.1 Non MRI technologies.....	12
1.5.2 Advantage of Real time MR Imaging of the Lung.....	13
1.6 Objectives.....	13
1.7 Thesis Organization.....	15
<b>Chapter 2 Theory .....</b>	<b>16</b>
2.1 Magnetic Resonance Physics .....	16
2.1.1 Spins in a Magnetic Field.....	16
2.1.2 Statistical Mechanics and Net Magnetization .....	17
2.1.3 Magnetic Precession.....	18
2.1.4 Bloch's equation and MR Relaxation .....	19
2.1.5 Rotating Frame of Reference.....	20
2.1.6 RF ( $B_1$ ) Tipping Pulse .....	21
2.1.7 $T_2$ and $T_2^*$ .....	21
2.1.8 MR Signal Detection .....	22
2.2 Imaging Principles.....	23
2.2.1 Fourier Transform.....	23

2.2.2 Magnetic Field Gradients .....	24
2.2.3 Slice Selection .....	24
2.2.4 Frequency Encoding and Quadrature Detection.....	25
2.2.5 Phase Encoding.....	27
2.2.6 2D Signal Equation and $k$ -space.....	28
2.3 Imaging Sequences: Spin Echo .....	29
2.3.1 Spin Echo Sequence .....	29
2.3.2 Turbo Spin Echo Sequences .....	31
2.4 Imaging Sequences: Gradient Echo Imaging.....	32
2.4.1 Spoiled Gradient Echo Sequence .....	32
2.4.2 SSFP-FID and SSFP-Echo .....	33
2.4.3 Balanced SSFP .....	34
2.5 Signal, Noise, Contrast.....	36
2.5.1 Signal-to-Noise Ratio .....	36
2.5.2 Contrast to Noise Ratio.....	37
2.6 Effects of Changing Main Magnetic Field Strength .....	38
2.6.1 SNR Dependence on $B_0$ .....	38
2.6.2 Relaxation Values Dependence on $B_0$ .....	39
2.7 $k$ -space Sampling.....	41
2.7.1 Field of View and the Nyquist Criterion .....	42

2.7.2 Spatial Resolution and Voxel Size .....	43
2.8 MR Acceleration .....	44
2.8.1 Regular Under-sampling and Parallel Imaging .....	45
2.8.2 Compressed Sensing.....	52
2.8.3 Split Bregman Solver for Compressed Sensing .....	58
2.9 Dynamic MR Acceleration.....	59
2.9.1 Exploiting Temporal Redundancy: Viewsharing .....	60
2.9.2 Exploiting Temporal and Spatial Domain Serially.....	63
2.9.3 Exploiting Temporal and Spatial Redundancy Jointly .....	64
2.10 Summary .....	67

## **Chapter 3 Validation of a tumour autocontouring algorithm 68**

3.1 Introduction .....	68
3.1.1 Artificial Neural Network Based Tumour Tracking Algorithm.....	68
3.1.2 Preparatory Steps and User Input. ....	69
3.1.3 Parameter Optimization .....	69
3.1.4 Main Processes .....	70
3.2 Validation Study – Methods.....	71
3.2.1 Phantom Experiment Setup .....	71
3.2.2 The MRI Protocol for Phantom Data Acquisition.....	74
3.2.3 Phantom Image Post Processing.....	75

3.2.4 Patient Study – Data Acquisition.....	76
3.2.5 Patient Data - Image Post Processing.....	77
3.2.6 Contour Comparisons.....	78
3.2.7 Intra-observer and Inter-observer variability experiment.....	79
3.3 Results.....	80
3.3.1 Auto-Contouring Results.....	81
3.3.2 Intra-observer/Inter-observer Reliability.....	82
3.4 Discussion.....	84
3.5 Summary.....	87

## **Chapter 4 Prior Data Assisted Compressed Sensing.....88**

4.1 Introduction.....	88
4.2 Methods.....	89
4.2.1 Original CS Method.....	89
4.2.2 Spatial-Temporal CS.....	90
4.2.3 Prior Data Assisted CS (PDACS).....	91
4.2.4 Retrospective Study Based on <i>in-vivo</i> Data.....	92
4.2.5 MR Data Acquisition/Manipulation.....	92
4.2.6 Generation of Sampling Patterns.....	93
4.2.7 Evaluate of Overall Image Reconstruction Quality (Artifact Power).....	99
4.2.8 Evaluation of Tumor Tracking Accuracy.....	99

4.2.9 Distinction between “Recent” vs. “Outdated” prior data .....	100
4.2.10 3T vs Pseudo 0.5T Experiments .....	100
4.3 Results .....	100
4.3.1 Image Evaluation – Global Image Quality (Artifact Power).....	100
4.3.2 Tumour Tracking Accuracy.....	102
4.4 Discussion .....	105
4.5 Effect of Outdated Prior Data on PDACS and Viewshare.....	108
4.6 Summary .....	109

## **Chapter 5 Sliding Window PDACS.....110**

5.1 Introduction .....	110
5.2 Methods.....	112
5.2.1 Sliding Window Sampling Patterns.....	112
5.2.2 Sliding Window Strategies 1 – Sliding Window Averaging.....	114
5.2.3 Sliding Window Strategies 2– Sliding Window with Navigator Guidance .....	115
5.2.4 Evaluating Decline in Image Quality due to the Outdated Prior Data .....	117
5.3 Results .....	118
5.3.1 Artifact Power – 3 T SNR .....	118
5.3.2 Tumour Tracking Error – 3 T SNR .....	119
5.3.3 Image Reconstruction Error – Pseudo 0.5T SNR.....	119
5.3.4 Tumour Tracking Error – pseudo 0.5T SNR.....	120

5.4 Discussion .....	121
5.5 Summary .....	125
<b>Chapter 6 Conclusions and Future Direction .....</b>	<b>127</b>
<b>References .....</b>	<b>130</b>

## List of Tables

Table 3-1 – Lung Tumour and Normal Lung Parenchyma Contrast Parameters measured on the 3T scanner compared to literature values at 0.5T as used in the phantom designed to mimic 0.5T MR contrast in a 3T scanner. ....	73
Table 3-2 – Measured SNR and CNR of the Phantom Tumour model in the pseudo 0.5 T images. ....	76
Table 3-3 – Measured Tumour SNR, Area, and Maximum extent of motion for the 4 patients. .	78
Table 3-4 – Dice’s Coefficient and Centroid Displacement Error of Autocontours compared against Standard. ....	81
Table 3-5 – Intra-observer variability .....	82
Table 3-6 – Inter observer variability .....	83
Table 4-1 - Optimal weights $\lambda_1$ for CS, determined by the 2-step algorithm for this study .....	97
Table 4-2. Optimal weights $\lambda_1, \lambda_2$ for PDACS, determined by the 2-step algorithm for this study. ....	98

## List of Figures

Figure 1-1: Schematic Diagram representing the various volumes described by ICRU reports. GTV represents the visible tumour in the image. CTV includes the GTV and a margin to account for microscopic disease. ITV includes CTV and the internal margins that account for organ motion. PTV includes a further set up margin accounting for mechanical uncertainties and set up errors. The treatment volume is the actual volume of tissue that received the prescribed dose, and the irradiated volume also includes any healthy tissues that have received significant dose with regards to normal tissue tolerance. .... 4

Figure 1-2 – Current prototype of the Linac-MR system developed at the Crossed Cancer Institute. ([www.linac-mr.ca](http://www.linac-mr.ca)) ..... 8

Figure 1-3 – Comparing the real time imaging strategies for tracking lung tumours..... 13

Figure 2-1: Sequence diagram for a spin echo sequence. RF describes the radiofrequency pulse,  $G_x, G_y, G_z$  describes the x, y, z gradients, and Acq. describes the acquired signal. TE is the echo time, and TR is the repetition time. The lower magnitude RF pulse is  $90^\circ$  excitation and the higher magnitude RF pulse is  $180^\circ$  re-focusing pulse that falls mid-way between  $90^\circ$  excitation pulse and the center of the acquired FID, Acq..... 30

Figure 2-2: Sequence diagram of the spoiled gradient echo sequence. Random gradients are employed to spoil the remaining transverse magnetization at the end of each TR interval. .... 32

Figure 2-3: Sequence diagram for the SSFP-FID sequence (Top) and the SSFP-echo sequence (Bottom). They are mirror image of each other ..... 34

Figure 2-4: Sequence diagram for the balanced SSFP sequence..... 36

Figure 2-5: Sample spectral density for protons in 3 different environments. Blue curve represents protons in a tightly bound environment, green curve represents protons in free water,

and the red curve represents water in most tissues, which is an intermediate between the other two extreme cases. .... 40

Figure 2-6: A demonstration of how various reductions of  $N_{pe}$  affect the fully sampled image in the first row. Second row represents the acquisition of central 25% of  $k$ -phase encode lines while maintaining  $\Delta ky$  and FOV, resulting in a loss in resolution. Third row represents 25% sampling over the entire  $k$ -space while increasing  $\Delta ky$  by 4 folds in order to maintain FOV, which leads to aliasing versions of base image within the FOV. Un-sampled locations are zero filled to maintain nominal resolution. .... 44

Figure 2-7 – A schematic diagram, describing a hypothetical 2 coil system positioned around a digital phantom. .... 46

Figure 2-8 - First row: Theoretical Sensitivity maps for coil1 (left) and coil 2(right). Second row: detected signal for each coil when  $k$ -space is fully sampled and Third Row: detected signal for each coil when  $k$ -space is under-sampled by 50% along the phase encode direction. .... 47

Figure 2-9 – A map describing the absolute value of the denominator  $S1S2\Delta - S2S1\Delta$  Noise amplification becomes a problem when this value is low (blue). .... 49

Figure 2-10 - The linear combination of 4 coil sensitivity profiles is used to simulate spatial harmonics on the right, as described in a figure adapted from Blaimer *et al*<sup>46</sup> ..... 51

Figure 2-11 Left: randomly acquired  $k$ -space points with the center of  $k$ -space acquired with higher frequency. Compared to the under-sampling pattern of Figure 1-3, the artifact from random under-sampling manifests itself as incoherent noise. .... 54

Figure 2-12 - Top Row: from left to right,  $k$ -space sampling pattern of 4x regular under-sampling, 4x random under-sampling in 1D and 4x random under-sampling in 2D. Bottom row: corresponding PSF analysis ( $k$ -space) for each pattern. Regular under-sampling 4 foldover

points with similar intensity to the main peak. In 1D random under-sampling, those peaks are evenly spread along one axis, whereas in 2D random, it is further spread out along both axes. CS performs best when the interference peaks are low. .... 55

Figure 2-13 - A demonstration of the L-curve method, adapted from by Kim et al.<sup>51</sup> ..... 57

Figure 2-14 - From left to right: CS reconstructed image from figure 3-1 using optimal CS weight (lower left corner of L-curve), very low weight (upper left corner of L curve) and very high weight (lower right corner of L-curve). .... 57

Figure 2-15 – *k*-space acquisition scheme of MR fluoroscopy..... 61

Figure 2-16 - *k*-space acquisition scheme of MR fluoroscopy. .... 61

Figure 2-17 – Demonstration of a potential pitfall of KEYHOLE imaging. The left image represents the base image, whereas the middle image represents the fully sampled dynamic image. The right image represents a keyhole dynamic in which the central 25% of *k*-space acquired but the remainder of *k*-space is shared from the base image. The high frequency component from the base image manifests itself as artifacts..... 62

Figure 2-18 *k*-space acquisition scheme of TRICKS..... 63

Figure 2-19 – GRAPPA compared to T-GRAPPA. In T-GRAPPA, *k*-space points from previous dynamic serves as ACS used to determine coil weight for GRAPPA reconstruction. .... 64

Figure 2-20 – Left the UNFOLD technique, Right: k-T BLAST technique, adapted from Tsao<sup>53</sup>.  
..... 65

Figure 3-1 – (a) A dynamic MR image containing the tumour (red arrow), which is zoomed in, and displayed with the manually defined (b) ROI<sub>STD</sub> (c) background..... 69

Figure 3-2: The multi-step process in which the tumour shape is determined from the image: (a) The expanded ROI<sub>STD</sub> from which the algorithm determines the tumour region. (b) The neural

network contrast enhancement. (c) Thresholding by Otsu’s method. (d) Removal of small discontinuous islands, e) smoothing and f) Dilation/Erosion. .... 70

Figure 3-3: A schematic diagram describing the motion phantom. .... 72

Figure 3-4 – S-I Motion Pattern applied to the phantom. A sine pattern and 3 patient patterns, based on a Cyberknife™ study<sup>70</sup> is used. .... 74

Figure 3-5 – Left : High Resolution (0.4 mm) reference scan allows for visualization of edge of tumour, Right, lower resolution (3.1mm) dynamic scans acquired at 4 fps. .... 75

Figure 3-6: Fully sampled images of our 6 patients. Red arrows indicate the location of lung tumour. .... 77

Figure 3-7 – Noise added, pseudo 0.5 T equivalent images of our 6 patients. .... 78

Figure 3-8: Degree of Superior Inferior (Green, Solid) and Anterior Posterior (Blue, Dashed) tumor motion of 6 patients. .... 80

Figure 3-9 Intra-observer variations, ( $DC_{INTRA}$ , blue) and Inter-observer variations ( $DC_{INTER}$ , gray) for all 6 patients is plotted next to autocontouring accuracy in terms of Dice’s coefficient, ( $DC_{AUTO}$ , orange). Error bars represents 95% confidence interval.  $DC_{AUTO}$  is significantly larger than  $DC_{INTRA}$  in patients 1 and 5, while significantly lower in patients 2 and 4.  $DC_{AUTO}$  is significantly larger than  $DC_{INTER}$  in patients 1, 2 and 6 and significantly lower in patients 4 and 5. .... 84

Figure 3-10: Example contours of the most difficult case encountered in our data (patient 5). Top Left – Image to be contoured, with ambiguous region shown by the red arrow. Top right,  $ROI_{STD}$  contoured by the radiation oncologist. Bottom left  $ROI_{AUTO}$  contoured by the automatic algorithm, missing part of the ambiguous region. Bottom left  $ROI_{STD2}$ , contours drawn by the same oncologist on the identical image/window/level on a different day. .... 86

Figure 4-1 – Sampling Pattern in k-space used for 2D – CS and PDACS reconstruction ..... 95

Figure 4-2 A plot describing the search for the optimal  $\lambda_1, \lambda_2$  values. Dots represent a tested pair of  $\lambda_1, \lambda_2$ , with the color and size of the dots representing the artifact power. Once the minimum is found in the rough search (left), a finer search (right) is performed in the neighbouring region. .... 96

Figure 4-3 - Examples of reconstructed images based on the fully sampled image in Figure 2, top row, left. First Row: Reconstructed image at 2x acceleration (50% sampling), Left, 2D-CS; Centre, Viewshare; Right, PDACS; Second Row: reconstructed at 5x acceleration (20% sampling), Second Row: Left: 2D-CS, Centre, Viewshare; Right, PDACS. Red arrows indicate presences of noise like artifacts. .... 101

Figure 4-4 - Left: Aggregate artifact power for the three patients at the original 3T SNR images. Right: Aggregate artifact power in the pseudo 0.5 T SNR images. Please note the difference in y axis. Error bars indicate 95% confidence interval as determined from the standard error of the mean. .... 102

Figure 4-5 - Top Row: Zoomed in fully sampled images of the tumour as it undergoes breathing motion from inhale to exhale (Images 62, 65, 69). Bottom Row: Identical Images reconstructed with PDACS 4x acceleration. Tumour is indicated by red arrow..... 103

Figure 4-6 - Averaged Dice's coefficients, aggregated for 5 patients for all images reconstructed at the original 3T SNR (left) and the pseudo 0.5T SNR (right) with the increasing acceleration factor. Error bars indicate 95% confidence interval as determined from the standard error of the mean. .... 104

Figure 4-7 - Mean Centroid Displacement Error, averaged over 5 patients for all images reconstructed at the original 3T SNR (left) and the pseudo 0.5T SNR (right) with an increasing

acceleration factor. Error bars indicate 95% confidence interval as determined from the standard error of the mean. .... 105

Figure 4-8 - A schematic diagram demonstrating the benefit of speeding up acquisition time at the expense of increasing reconstruction time. As reconstruction of images from different slices are independent processes that can be performed in parallel, the accelerated scenario results in images that are updated at 150ms instead of 750ms in the first scenario ..... 108

Figure 4-9 – Mean artifact power for all patients for 3T dynamic images 21-220, 221-430, 431-650. Progressive increase is artifact power observed for PDACS and viewsharing, where prior data is used, but not in CS where prior data is not used. .... 109

Figure 5-1 – Monitoring the change in bSSFP signal over time using the difference image. Top row, Column 1: initial magnitude image. Top row, Columns 2 – 4: difference image generated by subtracting images 101, 201, and 301 from the initial image. Bottom Row, Columns 1- 4: difference image generated by subtracting images 401, 501, 601, and 701 from the original image..... 111

Figure 5-2 - Left: the original PDACS sampling pattern (25%) which uses identical sampling patterns for all image dynamic in which the non-sampled k-space locations are not updated, and the sliding window pattern in which all k-space locations are updated..... 113

Figure 5-3 The probability redistribution process, applied in a simple case of 5 k-space locations, the algorithm starts with equal probability in all locations at  $p_1$  (0.2), the Monte Carlo process determines a sampling pattern from it, after which the probability from the sampled location is redistributed to the non-sampled location, resulting in probability distribution  $p_2$ . This process ensures good temporal spacing between sampling points while maintaining incoherent sampling required for Compressed Sensing. .... 114

Figure 5-4 – Left – sliding window averaging method, each circle represents a k-space line. All data that corresponds to an unsampled location of current data (filled circle) is averaged and applied in reconstruction. Right – sliding window with navigator, the data within the sliding window is ranked based on navigator similarity – with the closest available match in each location used as prior data..... 115

Figure 5-5 – Left, a 2D Fourier transform of the full k-space, Right, the equivalent profile resulted from a 1D FT of the central K-space line..... 116

Figure 5-6- Actual tumour superior-inferior centroid position(top, blue) for a single patient as determined by contouring vs. approximate diaphragm position (bottom, green) as determined by the maximum correlation calculations of the navigator profiles. .... 117

Figure 5-7 – Quantitative comparison of the 3 acceleration methods for 3 T images. First row, Artifact power for 2 – 5x acceleration are shown. Second Row: Centroid Displacement Error (in mm) is shown. Third row, Dice’s Coefficients are shown. Image groups 1, 2, 3 represent a binned average of image 1-210, 211-420, 421 - 630. Error bars indicate 95% confidence intervals..... 118

Figure 5-8 – Quantitative comparison of the 3 acceleration method for pseudo 0.5 T images. First row, Artifact power for 2 – 5x acceleration are shown. Second Row: Centroid Displacement Error (in mm) is shown. Third row, Dice’s Coefficients are shown. Image groups 1, 2, 3 represent a binned average of image 1-210, 211-420, 421 630. Error bars indicate 95% confidence intervals. .... 120

Figure 5-9 – Qualitative comparisons of representative images (chosen similar phase) from groups 1 in 3 (left to right). 2.5 accelerated images from Non Sliding window (row 2), Sliding window with navigator (row 3) and sliding window with averaging (row 4) are shown.

Progressive increase in artifacts is easily observed in row 2, which are not observed in the sliding window methods. .... 121

Figure 5-10 – Pseudo 0.5T image (#506) for the same patient shown in Figure 5-9 at 2.5x acceleration, reconstructed using sliding window with navigator (left), sliding window averaging (centre) and non-sliding window (right). Noise measurement is performed by calculating the standard deviation (SD) in the white box. .... 123

## List of Acronyms

<b>2D-CS</b>	Two Dimensional Compressed Sensing
<b>3D-CRT</b>	Three Dimensional Conformal Radiation Therapy
<b>4D-CT</b>	Four Dimensional Computed Tomography
<b>ACS</b>	Auto Calibration Signal
<b>AP</b>	Anterior Posterior
<b>BEV</b>	Beam's Eye View
<b>bSSFP</b>	Balanced Steady State Free Precession
<b>CBCT</b>	Cone Beam Computed Tomography
<b>CCI</b>	Crossed Cancer Institute
<b>CERR</b>	Computational Environment for Radiotherapy Research
<b>CNR</b>	Contrast to Noise Ratio
<b>CPU</b>	Central Processing Unit
<b>CS</b>	Compressed Sensing
<b>CT</b>	Computed Tomography
<b>CTV</b>	Clinical Target Volume
<b>DC</b>	Dice's Coefficient
<b>DCT</b>	Discreet Cosine Transform
<b>DIBH</b>	Deep Inspiration Breath Hold
<b>dMLC</b>	Dynamic Multi Leaf Collimator
<b>EPID</b>	Electronic Portal Imaging Device

<b>FFE</b>	Fast Field Echo
<b>FFT</b>	Fast Fourier Transform
<b>FID</b>	Free Induction Decay
<b>FLASH</b>	Fast Low Angle Shot
<b>FOV</b>	Field of View
<b>FSE</b>	Fast Spin Echo
<b>GRAPPA</b>	Generalized Autocalibrating Partial Parallel Acquisition
<b>GTV</b>	Gross Tumour Volume
<b>IGRT</b>	Image Guided Radiation Therapy
<b>IM</b>	Internal Margin
<b>IMRT</b>	Intensity Modulated Radiation Therapy
<b>ITV</b>	Internal Target Volume
<b>kV</b>	Kilovoltage
<b>Linac</b>	Linear Accelerator
<b>LR</b>	Left Right
<b>MIP</b>	Maximum Intensity Projection
<b>MLC</b>	Multi Leaf Collimator
<b>MR</b>	Magnetic Resonance
<b>MRI</b>	Magnetic Resonance Imaging
<b>MV</b>	Megavoltage
<b>MVCT</b>	Megavoltage Computed Tomography

<b>NMR</b>	Nuclear Magnetic Resonance
<b>OBI</b>	On Board Imaging
<b>PD</b>	Proton Density
<b>PDACS</b>	Prior Data Assisted Compressed Sensing
<b>PDF</b>	Probability Density Function
<b>PET</b>	Positron Emission Tomography
<b>PICCS</b>	Prior Image Constrained Compressed Sensing
<b>PTV</b>	Planning Target Volume
<b>RARE</b>	Rapid Acquisition with Relaxation Enhancements
<b>RF</b>	Radiofrequency
<b>RHS</b>	Right Hand Side
<b>ROI</b>	Region of Interest
<b>RT</b>	Radiation Therapy
<b>RTPS</b>	Radiation Treatment Planning System
<b>RTTT</b>	Real Time Tumour Tracking
<b>SAR</b>	Specific Absorption Ratio
<b>SBRT</b>	Stereotactic Body Radiation Therapy
<b>SD</b>	Standard Deviation
<b>SE</b>	Spin Echo
<b>SENSE</b>	Sensitivity Encoding
<b>SI</b>	Superior Inferior

<b>SM</b>	Set-up Margin
<b>SMASH</b>	Simultaneous Acquisition of Spatial Harmonics
<b>SNR</b>	Signal to Noise Ratio
<b>SPECT</b>	Single Photon Emission Computed Tomography
<b>SSFP</b>	Steady State Free Precession
<b>SW-PDACS</b>	Sliding Window Prior Data Assisted Compressed Sensing
<b>TE</b>	Echo Time
<b>TR</b>	Repetition Time
<b>TRICKS</b>	Time Resolved Imaging of Contrast Kinetics
<b>TSE</b>	Turbo Spin Echo
<b>TV</b>	Total Variations

# Chapter 1 Introduction

## 1.1 Background

Cancer is the leading cause for death in Canada<sup>1</sup>, responsible for approximately 30% of deaths amongst Canadians. It is estimated that in 2015, there will be approximately two hundred thousand new cases of cancer in Canada<sup>1</sup>, with the majority of new cases (51%) being lung, breast, colorectal and prostate cancers. Of the various types of cancers, lung cancer is particularly deadly, being responsible for more deaths than the other three major types combined<sup>1</sup> (27%). The economic impact of cancer is substantial, with an estimated total direct and indirect economic cost<sup>2</sup> of 22.5 billion, or 1.5% of Canada's Gross Domestic Product.

For several decades, an intensive scientific effort has been underway to develop and improve methods to prevent, diagnose and treat cancer. Medical Physicists have made significant contributions to new technological developments that have improved survival rates and quality of life for cancer patients. Two particular areas of cancer care in which physicists play a major role are radiation therapy (RT), and medical imaging.

Radiation therapy is the clinical application of ionization radiation, such as high energy photons, for the treatment of disease<sup>3</sup>. In cancer treatment, ionizing radiation destroys cancer cells by damaging its DNA. Currently, approximately half of all cancer patients will receive adjuvant radiation treatment, with either curative or palliative intent. The goal of radiation therapy is to deliver a high dose of radiation to a specific target volume while minimizing the dose to the surrounding healthy tissues. Therapeutic radiation can be delivered internally via radioactive implants, as in the case of brachytherapy, or can be delivered with an external beam.

Over the previous century, a variety of technologies have been developed to deliver external beam radiation. The Coolidge tube was developed early in the 20<sup>th</sup> century, capable of generating peak energy of 140 kilovolts (kV) in 1913 and 200kV in 1920. Radiation beams of megavoltage (MV) energy were achieved in the 1940's with the Betatron unit. The Cobalt-60 radio-isotope based tele-therapy system, developed in Canada, was used to treat cancer patients for the first time in 1951; these systems are still commonly used in developing countries. In 1953, the first medical linear accelerator (linacs) was built in England and reached clinical status in the 1960's. Today, the vast majority of radiation therapy treatments in the developed world

are delivered using Linac technologies. Linacs typically emit higher energy photons compared to Cobalt-60 (i.e. 6 – 18 MVs x-rays vs.  $\sim 1.25$  MeV). The benefits of higher energies include reduced skin dose, sharper beam penumbras, and greater beam penetration<sup>4</sup>.

Medical imaging is the clinical application of low energy radiation, nuclear magnetic resonance and ultrasound waves to image patients for anatomical and physiological diagnosis of disease. Medical Imaging has broad range of applications in cancer ranging from early detection and diagnosis to treatment planning, verification and response assessment. Two-dimensional (2D) imaging modalities such as radiography, mammography and fluoroscopy, are still commonly used in clinics today. More advanced modalities which are capable of three-dimensional (3D) imaging include computed tomography (CT), single photon emission computed tomography (SPECT), positron emission tomography, (PET), ultrasound and magnetic resonance imaging (MRI).

## **1.2 Modern Radiation Therapy**

While imaging and therapy have traditionally been separate disciplines within medical physics, the advancement in imaging technologies has contributed to improvements in RT. The developments of 3D imaging modalities in the 1970's (CT and MRI) have led to a major improvement in the radiation therapy (RT) process, known as 3D conformal radiation therapy (3D-CRT)<sup>3</sup>. In the 3D-CRT process, the physician identifies a specific 3D target volume in these images. The radiation treatment planning system (RTPS) employs a number of different radiation treatment beam orientations to conform the high radiation dose to a complex shape of the target volume. More recently, Intensity Modulated Radiation Therapy (IMRT) has introduced radiation beams with non-uniform intensity distribution within the exposed portal. The beam intensity patterns are obtained through an iterative algorithm for plan optimization<sup>5</sup>, and are implemented using dynamic multi-leaf collimator (dMLC) for beam delivery<sup>6</sup>. IMRT allows for further conformation of dose to the target volume while maintaining tolerable doses to surrounding healthy organs and tissues. IMRT represents the state of the art technology available today for conforming radiation dose to the shape of a tumor.

### **1.2.1 Target Volumes – Basic Definitions**

IMRT based treatment plans have very sharp dose fall off away from the intended treatment volume. Therefore, the positional accuracy of the treatment volume with respect to the beam

geometry is of paramount importance. Several important concepts and standard terminology for this topic, as defined by the International Commission of Radiation Units and Measurements (ICRU) in a series of reports including 50<sup>7</sup>, 62<sup>8</sup>, and 71<sup>9</sup> are introduced in this section. These definitions, among other issues, specifically address the uncertainty in positioning both the patient and the treatment volume within.

On an image, the **Gross Tumour Volume (GTV)** is the visible extent and location of the malignant growth; GTV may include the primary tumour site, metastatic lymph nodes and other metastases. However, due to limitations of imaging modalities, microscopic malignant cells cannot be adequately visualized, therefore, a **clinical target volume (CTV)** is defined by the physician to include both the GTV and the suspected extent of microscopic diseases that surrounds it. The ideal goal of radiation therapy is to deliver a uniform, therapeutic dose of radiation to this volume spanned over a large number (typically 30) of daily fractions.

There are several sources of uncertainty in the radiation therapy process that hinders in achieving this ideal goal. These uncertainties occur in 1) the daily set-up of patient, 2) the mechanical components of radiation therapy machine and 3) organ motions. These uncertainties make it difficult to exactly align the CTV to the treatment beam in each fraction. To account for the uncertainties due to internal organ motions, an **internal margin (IM)** is added to CTV to yield an **internal target volume (ITV)**. To account for the mechanical tolerances of linacs and day-to-day positioning uncertainty in setting up the patient, a **set-up margin (SM)** is further added to yield the **Planning Target Volume (PTV)**. It should be noted that the term **PTV margin** describes the all margins added to the CTV, which includes both the IM and the SM. Of the three factors that contribute to the PTV margin, the mechanical tolerance of the radiation therapy treatment machine is the least contributing factor. The uncertainty in the daily patient setup can be reduced by employing some form of imaging which is, at least, capable of imaging bony anatomy of the patient in the treatment position. For some tumour sites, the most significant, and also the most difficult to circumvent factor is the internal organ motion. It is important to distinguish between two types of organ motions: *inter*-fractional organ motion, which is the organ motion that occurs in the timescale of the days of treatment (such as a shrinking of the tumour as a response to treatment and weight loss) and *intra*-fractional organ motion, which is the type of motion the occurs during treatment, such as due to cardiac or respiratory motion,

swallowing etc. A PTV margins must account for all of these uncertainties. Due to limitations of irradiation techniques, the **Treated Volume**, or volume of tissues receiving the prescribed dose, is usually larger and of a simpler shape compared to the desired PTV. Finally, the **irradiated volume** also includes healthy tissues that receive significant dose in respect to their sensitivity to radiation *i.e.* the tolerance dose. A schematic diagram showing the various target volumes is shown in Figure 1-1.

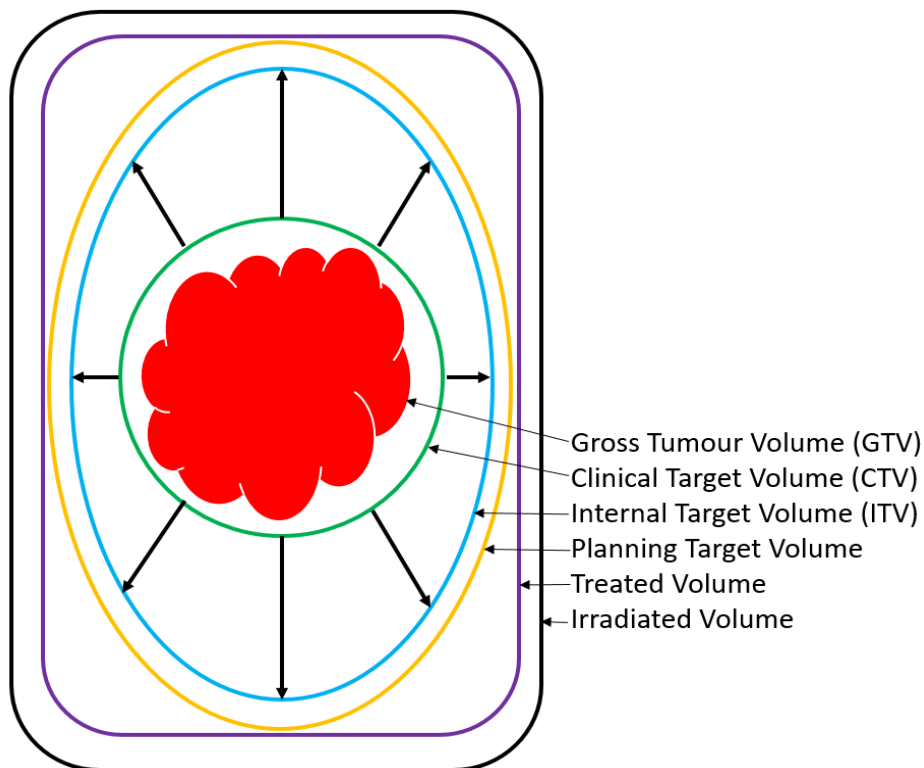


Figure 1-1: Schematic Diagram representing the various volumes described by ICRU reports. GTV represents the visible tumour in the image. CTV includes the GTV and a margin to account for microscopic disease. ITV includes CTV and the internal margins that account for organ motion. PTV includes a further set up margin accounting for mechanical uncertainties and set up errors. The treatment volume is the actual volume of tissue that received the prescribed dose, and the irradiated volume also includes any healthy tissues that have received significant dose with regards to normal tissue tolerance.

### 1.3 Image Guidance in Radiation Therapy

The main advantage of modern radiotherapy (i.e. via IMRT) of delivering a high dose to the CTV while sparing normal tissues cannot be fully realized if there is a large PTV margin (IM and SM). Therefore, considerable research has focused on developing methods to reduce these margins. One major effort has been the incorporation of imaging devices with radiation therapy treatment units. The form of RT in which patient imaging in treatment position is used daily to

align the patient (or the CTV if visible), with the treatment beam(s) for the purpose of reducing PTV margin is known as the image guided radiation therapy (IGRT).

### **1.3.1 Image Guidance Based on 2D Imaging and Fiducial Markers**

A relatively simple addition to the linac that allows 2D radiographic projection imaging, akin to the conventional radiography, is a portal imaging device. In this approach, a film or a digital detector, such as an electronic portal imaging device (EPID) is used to acquire an image using the x-ray photons of the treatment beam<sup>10</sup>. The significant drawback of portal imaging using MV photons is the extremely poor soft tissue contrast in the patient image. This limits the use of portal imaging to visualizing bony structures and air pockets. Most tumours are far away from bony markers and their independent motion relative to bones makes it an ineffective approach to reduce PTV margins<sup>11</sup>; aligning the bones in the portal images to those in the reference planning image does not ensure the alignment of the PTV incorporating soft tissue tumour. To improve the utility of portal images, implanted fiducial markers are inserted near or inside the tumour. Measured locations of the fiducials in the portal images then serve as the surrogate of tumour position in the patient, which can be used for daily alignment of the tumour with the treatment beams' geometry. If the fiducial based guidance is successful then it can potentially reduce the PTV margins; however, there are several issues with this approach including: 1) fiducial insertion is an invasive procedure and can result in infection<sup>12</sup>; 2) not all treatment sites are amenable to fiducial insertion; 3) fiducials can migrate from their initial location during the treatment<sup>13</sup>; resulting in a poor correlation between fiducial and tumour position, and finally 4) the fiducials' images do not provide any information regarding the tumour's shape and volume changes. Further improvement to this approach is provided by the introduction of peripheral kV energy x-ray units into the treatment room<sup>14</sup>. While soft tissue contrast remains limited in kV projection images, bony contrast and the contrast of radio-opaque fiducial markers are significantly improved, while the additional radiation dose to the patient resulting from MV imaging is reduced.

### **1.3.2 Image Guidance by Direct Imaging of Soft Tissues**

To overcome some of the shortcoming of fiducial marker based IGRT techniques, other devices have been developed to directly image the tumour and the surrounding tissues. Ultrasound imaging devices have been proposed as an in-room imaging modality for soft tissue

visualization. However, the utility of ultrasound imaging is limited to the visualization of soft-tissue, albeit poorly, in pelvic and abdominal regions<sup>14</sup>. The image quality is strongly correlated with the operators' skill and experience level. In addition, the operator is required to operate the probe during the imaging process which makes it difficult to use this system while the radiation beam is on. Thus, the system is limited to pre-treatment image guidance and not suitable for real-time IGRT.

Diagnostic CT devices have also been introduced into the treatment room which allows for limited soft tissue imaging<sup>14</sup>. In these systems, the patient will be transferred in and out of the CT gantry using a couch, or the CT imaging unit itself may be moved into position using rails<sup>15</sup>. Unfortunately, patient position and inter organ location within may alter during the transition from CT imaging and beam delivery. Moreover, many soft-tissue solid tumour are poorly visualized in CT imaging. Another alternative approach is to acquire cone-beam volumetric CT (CBCT) images by integrating a kV source and an active matrix flat panel imaging detector onto the linac gantry<sup>16</sup>, orthogonal to the treatment beam direction. The disadvantage of a gantry mounted cone-beam imaging system is scattered radiation that degrades the quality of CT images obtained from these systems<sup>14</sup>. Additional weight on the gantry may cause it to sag, reducing the mechanical accuracy of the overall treatment system<sup>14</sup>. Full integration of the treatment unit and imaging device is achieved with the Tomotherapy device<sup>17</sup>. In this system, a 6 MV linac is mounted on a ring shaped gantry and it rotates continuously while the patient translates through the axis of rotation of the gantry. From the perspective of the patient, the treatment beam is delivered in a helical manner. Conceptually, the tomotherapy unit can be thought of as a CT unit in which the kV source is replaced with a 6MV Linac. The tomotherapy unit can operate in CT imaging mode, in which the linac is operated at reduced energy of 3.5 MV, to provide pre-treatment cross-sectional images of the bony anatomy of the patient; however soft-tissue contrast in these images is significantly poorer than the diagnostic CT images.

Many of these IGRT methods are beneficial in reducing the patient set up errors (SM) in terms of aligning bones. In that sense, the inter-fractional displacement of bony anatomy is reduced that provides some reduction of PTV margins. However, due to limits in soft tissue contrast in MV/kV projection imaging and the inability to perform CBCT (or CT on rails or MVCT) in real

time, they are generally ill suited to directly image the moving tumours in real-time while the treatment beam is delivering radiation.

### **1.3.3 Linac-MR Hybrid Systems**

One exciting development in IGRT technology is the integration of a radiation therapy and magnetic resonance imaging devices. The Viewray system<sup>18</sup> consists of the integration of three Cobalt-60 sources with a low field (0.3T), double donut magnet. Another system<sup>19</sup>, currently in development, by Philips Medical Systems and Elekta, uses a linear accelerator which irradiates through a 1.5T cylindrical magnet. The current prototype of the Linac-MR system<sup>20</sup> developed at the Cross Cancer Institute (CCI), based in Edmonton, Alberta, Canada, consists of 6 MV Linac mounted on a gantry along with 0.5T bi-planar magnet (Figure 1-2). MR images offer vastly superior soft tissue contrast compared to the imaging systems mentioned previously. Improved visualization of tumour and surrounding soft tissues may further reduce set up uncertainties. Since MR imaging uses non-ionizing radiofrequency (RF) pulses, no additional radiation dose will be delivered to the patient for daily positioning, which can be significant<sup>21</sup>. Another potential benefit of the Linac-MR system is large flexibility in MR imaging sequences, including some sequences that are capable of generating several images per second. Therefore, the system can, in principle, provide real time, intra-fractional tracking of moving tumours using volumetric images of the tumours and surrounding tissues. This application is not possible with the other systems mentioned in the previous section. The Linac-MR unit represents a major

breakthrough in IGRT technology.

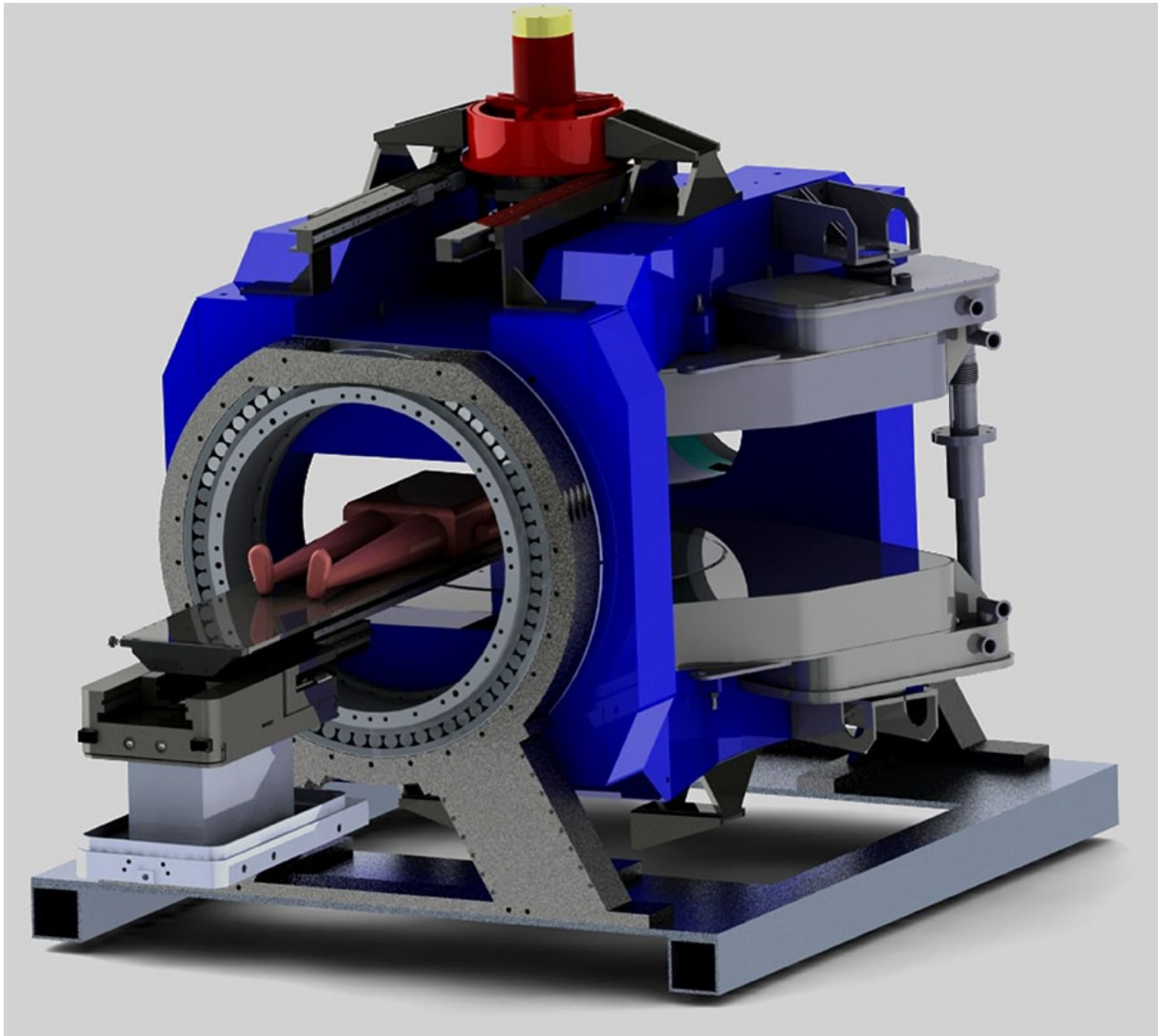


Figure 1-2 – Current prototype of the Linac-MR system developed at the Crossed Cancer Institute. ([www.linac-mr.ca](http://www.linac-mr.ca))

## 1.4 Respiratory Motion in Radiation Therapy

Lung cancer is the deadliest of all types of cancers<sup>1</sup>. For the treatment of lung cancer, radiation therapy is used both as primary treatment, or adjuvant to surgery and/or chemotherapy. Using a technique known as stereotactic body radiation therapy (SBRT), a very high dose of radiation is given in very few fractions; a treatment procedure that, in some cases, can be given as an

alternative to surgery for smaller tumours. The organ motion caused by the patient's respiration creates a considerable challenge in both conventional lung RT and SBRT. Various studies of lung tumour motion have observed a complex 3D trajectory, with the superior-inferior (SI) direction carrying the predominant motion. Reports of range of tumour motion vary widely, with the maximum motion reported being 50 mm in the SI direction, 24 mm in the anterior posterior (AP) direction and 16 mm in the left right (LR) direction<sup>22</sup>. In addition to lung, significant respiratory motion also is reported for abdominal organs such as pancreas, liver, kidney and the diaphragm. This section covers some of the common strategies in addressing respiration motion in radiation therapy.

#### **1.4.1 Encompassing the Entire Volume of Motion (ITV)**

In order to deliver the prescribed radiation dose to the CTV in the presence of organ (tumour) motion, a larger, motion encompassing ITV can be contoured instead. Imaging techniques have been used to create images with tumours that appear to encompass the entire volume bounding the motion trajectory. Free-breathing, slow CT scans are used to image the moving tumour so that the image is acquired over several phase of respiration<sup>23</sup>. This causes the tumour signal in the image to be blurred out over the entire volume of motion. The motional blurring also worsens the resolution of the image, which may lead to increasing inter and intra-observer variability in the radiation oncologists' contouring<sup>22</sup>. Another approach is to acquire CT images while the patients are holding their breath. Two sets of images are acquired: one at inhalation and the other at exhalation. After the appropriate image fusion and registration, a maximum intensity projection (MIP) from the two image sets is generated, creating the motion encompassing ITV<sup>24</sup>. Breath-hold technique creates less blurred images than the slow CT method, but this procedure requires twice the scan time and radiation dose<sup>22</sup>. This approach is not suitable for patients with compromised lung function who cannot hold breath for scan duration<sup>22</sup>. In a typical 4D-CT scan, due to the inherent imaging speed limitation by the rotation of the gantry, the different slices in a single 3D acquisition will be in a different phases of the breathing cycle. Therefore, in a typical in 4D-CT scan, about 8-25 complete CT data sets are reconstructed, and the 3D volumes are "sorted" in the correct phases during post processing<sup>22</sup>. Using these 3D volumes in different breathing phases, the 3D trajectory of the moving tumour can be reconstructed. The accuracy of 4D-CT (artifacts in the images) is affected by any

variations in the patient's breathing pattern<sup>22</sup>, and the radiation delivered to patient is increased when collecting data for all phases. As 4D-CT images are reconstructed after data is acquired for several breathing cycles, it is not a true real time imaging modality.

Defining a sufficient large ITV to encompass the entire range of tumour motion will ensure that the CTV receives the prescribed dose. However, the major disadvantage of this method is the irradiation of larger volume makes it difficult to lower the dose to the healthy lung.

### **1.4.2 Breath-hold Methods**

Another way of managing respiratory motion is to train patients to hold their breath during both treatment planning CT imaging and radiation delivery. In a deep inspiration breath hold (DIBH) position<sup>25</sup>, intra-fraction motion of the internal organs is reduced and the critical organs are located away from the PTV due to increased lung volume. Therefore, the critical organs are better protected as a result. A spiro-meter monitors the level of inspiration in the patient to improve reproducibility. For radiotherapy treatment planning, three CT scans are required, a free breathing CT scan, a spirometer monitored DIBH CT scan, and a spirometer inhalation scan. Treatment planning is performed on the DIBH CT scan while the free breathing and the inhalation image sets are used for quality assurance, and to generate an alternative treatment plan if the DIBH is unsuccessful. In general, the applicability of breath-hold technique is limited by patient compliance. In the DIBH study, 60% of lung cancer patients were not able to maintain their breath with the required degree of reproducibility for the DIBH treatment<sup>22</sup>.

### **1.4.3 Gating Methods**

Respiratory gating is another approach to address breathing motion. The concept of "gating" is to only deliver radiation when the tumour is located in a specified window in the respiratory cycle. There are numerous gating techniques available<sup>22</sup>, and they are performed using either an external motion detectors or internal fiducial markers. A gated set of CT images are typically required during the CT simulation session for gated therapy. Fiducial markers or the external tumour motion surrogates are used to generate a "respiratory signal" that is assumed to correlate with respiratory phases of lung motion. When the respiratory signal is within the preset gating window (i.e. gate width), the CT scanner acquires a single CT slice. The time required to acquire this single slice should be matched with the gate width. If the scan time is too short

compared to this gate width, the image will not fully encapsulate the motion within the gating window, resulting in a tumour that appears too small to account for the motion within the gating window. If the scan-time is too long compared to gate width, the opposite is true; the image captures motion that does not belong in the gating window, resulting in a tumour that appears too large. The gating process is time consuming because only a single slice of the 3D volume is acquired per breathing cycle. For beam delivery, a similar procedure is performed, with the radiation beam being delivered when the respiration signal falls within the gating window. As these methods use fiducial markers, more typically the external motion monitoring devices, as a surrogate for the tumour motion, these suffer from all the limitations as mentioned in section 1.3.1<sup>22</sup>. Compared to motion encompassing methods, a gating technique avoids the need for an ITV, and therefore it significantly reduces PTV margins and dose to normal tissues. This improvement does come with a cost; as the beam is only on for a narrow portion of the breathing cycle, the treatment time will be significantly increased<sup>22</sup>.

#### **1.4.4 Tumour Tracking Methods**

Perhaps the most useful approach is to track the moving tumours. In this approach, the moving tumour is imaged in real-time and the radiation beam is always aligned with the tumour. This procedure is commonly called tumour tracking. In principle, this approach eliminates the main disadvantages from the other techniques<sup>22</sup>. Compared to the tumour encompassing/ITV methods, the ability for the beam to follow the tumour trajectory can substantially reduce PTV margins. Patient compliance will be significantly less challenging as breath-hold is not required. Since radiation is continuously delivered while being repositioned to tumour in real time, tumour tracking methods will not increase the treatment time to the degree of the gated methods.

There are several aspects of real time tumour tracking. Firstly, the position of the tumour must be determined in real time. Secondly, all tumour tracking devices will have a significant delay time between imaging and radiation delivery (imaging time, computer processing time, multi-leaf collimator motion (MLC) delay etc.). This must be in some ways compensated by an efficient and accurate prediction algorithm to track tumour location during the latency. The accuracy of these prediction algorithms rapidly worsens with the increased delay time, therefore a delay time of more than 0.5 seconds is not considered suitable for tumour tracking<sup>22</sup> Thirdly, the beam must be repositioned in real time, either by motion of the Linac head, or by movement

of the MLC. Lastly, any dosimetric effects of breathing (such as the change in air volume) that is not captured by the static treatment planning images may lead to second-order dosimetry errors. The degree of impact of these effects require further investigation<sup>22</sup>.

## **1.5 Real Time Tumour Localization**

### **1.5.1 Non MRI technologies**

There are currently several technologies available for performing real time tracking of tumour in radiation therapy. The Calypso system<sup>26</sup> does not actually track the tumour with imaging, but relies on RF transponder as an external surrogate to predict the location of the tumour<sup>27</sup>, however, the complex and non-stationary correlation between these surrogates and the actual tumour could lead to uncertainties. Direct imaging of the tumour will eliminate these uncertainties but acquiring an image every 0.5 second is a considerable challenge. Full 3D visualization using cone beam computed tomography (CBCT) is not currently feasible in real time. In the absence of full 3D imaging, the most useful imaging plane for tracking tumor is the Beam's Eye View (BEV) plane, because any tumour motion captured in this this plane has the greatest impact on tumour dose caused mainly due to the geographic miss. In terms of currently available technology, the EPID imager on the Linac can, in principle, capture BEV images in fluoroscopy mode at MV energies in real time (Figure 1-3, left). However, MV images are of little value for visualizing tumours as the tissue contrast is very poor. The addition of kV sources can improve tissue contrast for fluoroscopy. However, due to interference with the MV beam, it is not possible to capture BEV kV images during MV irradiation. The On Board Imaging (OBI) devices added on conventional linacs are only capable of capturing kV images on a plane orthogonal to BEV (Figure 1-3, center left), missing one of the key dimension of motion. More specialized devices designed for motion tracking, such as the robot based Cyberknife system<sup>28</sup>, or the gimbal based VERO system<sup>29</sup>, both use two separate, oblique kV energy sources, positioned at 45 degree angle to the beam axis (Figure 1-3, center right),. In principle, by performing fluoroscopy simultaneously, the device can track the tumour in all the relevant directions. However, kV fluoroscopy still has limited contrast, if the tumour cannot be accurately visualized in either of the two views, parts of the motion cannot be captured, and PTV must be expanded to compensate. In some cases, radio-opaque fiducial markers are used instead, which comes with all of the associated disadvantages mentioned previously.

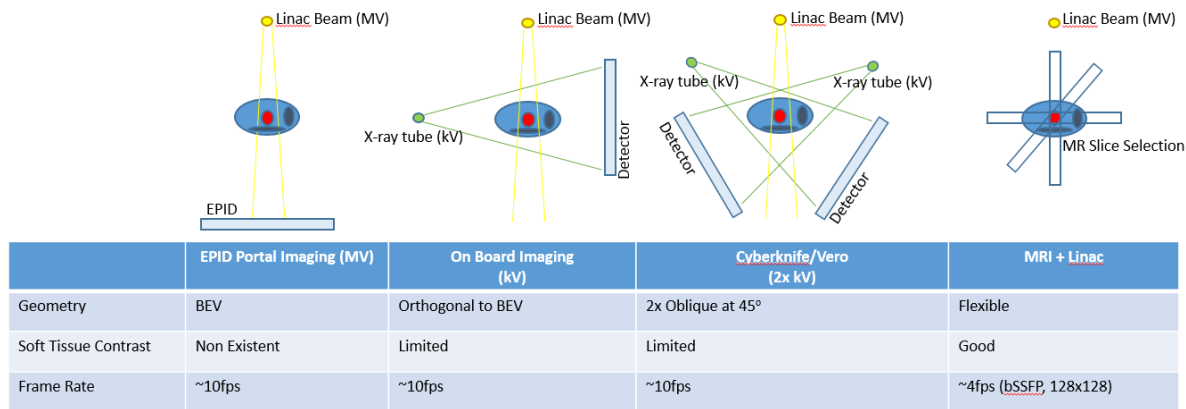


Figure 1-3 – Comparing the real time imaging strategies for tracking lung tumours.

### 1.5.2 Advantage of Real time MR Imaging of the Lung

Real time fluoroscopy, which is based on transmission of x-rays, captures images that contain superposition of all structures (i.e. bone, lung, tissue) between the x-ray source and the detector. The presence of structures above and below the tumour results in poor overall contrast. On the other hand, in MRI, only signals from only a user-defined imaging volume are detected, yielding a 2D slice in any orientation, with excellent soft tissue contrast compared to fluoroscopy. The geometric flexibility is particularly useful for tracking tumours, as it allows, BEV plane to be imaged, capturing the relevant motion of tumours (Figure 1-3, right). Fast MRI sequences have been developed such that 2D images, at modest resolutions can be acquired at the speed of several frames per second. The basic principles of MRI and fast sequences will be discussed in detail in the next chapter.

## 1.6 Objectives

While dynamic MRI provides real time imaging capability with vastly superior contrast compared to fluoroscopy, the achievable frame rate and spatial resolution is modest. The main goal of this thesis is to devise a novel acceleration strategy for real time MR tracking of lung tumours. The ability to increase MR acquisition speed will have many potential benefits: including 1) a reduction in the system delay time of the tumour tracking process, 2) an increase in frame rate that may improve the precision of the real time tumour location, 3) an increase in image spatial resolution and 4) the potential to acquire multiple slices while still be under the maximum delay time of 0.5 s, as recommended by TG-76<sup>22</sup>.

The novel strategy devised, called Prior Data Assisted Compressed Sensing (PDACS), is a method designed to take advantage of spatial-temporal redundancies in dynamic MR sequences that can be used for tracking tumour motions. In essence, this method aims to reconstruct images that provide tumour contours using partial data acquisition. This method relies on drawing from a pool of prior data, acquired at the beginning of the sequence to aid in reconstruction of dynamic images of a plane.

A key indicator of the quality of any accelerated MR image is the ability to generate accurate tumour contours. A novel neural-network based tumour tracking algorithm<sup>30</sup> has been developed at the CCI. In this thesis, a validation study of the new acquisition/reconstruction methods using this tumour tracking algorithm is performed, against a gold standard, using a motion phantom as well as for lung cancer patients. Once this algorithm is validated, it is used to evaluate the PDACS algorithm.

The PDACS algorithm is evaluated by performing a retrospective study. Six patients with lung cancer are recruited with ethics approval. A free breathing, dynamic MR scan is performed on each patient. These fully sampled images serve as a useful standard for testing our algorithm. MR acceleration with partial k-space is simulated by removal of k-space data from these fully sampled standard data sets. Reconstruction of these partial k-space data is compared against the original, fully sampled datasets using various quantitative metrics.

Due to the instability in the MRI system, relying on outdated prior data may lead to negative consequences in long dynamic sequences. These effects are explored, and potential solutions, which use a sliding window to refresh the prior data, are presented.

While the overall goal of the thesis is algorithm development, we propose following hypotheses in this work:

1. The auto-contouring algorithm is capable of extracting contours of tumours from real time MR images. These contours are accurate when compared to a gold standard, in terms of Dice's coefficient and centroid positions.
2. The inclusion of motion averaged prior data in compressed sensing improves image quality, in terms of the global and local performance indicators, including artifact power, auto-

contouring Dice's coefficient and centroid displacement error, compared to conventional compressed sensing.

3. A reconstruction algorithm that allows for the prior data pool to be constantly refreshed using more recent data further improves compressed sensing image quality, in terms of indicators stated above, especially for the long duration dynamic scans.

## **1.7 Thesis Organization**

This thesis is organized in the following manner. Chapter 1 contains introductory background information on image guided radiation therapy and the benefits of MR/Linac hybrid systems, as well as the potential of real time tumour tracking. Chapter 2 contains the basic physics of magnetic resonance imaging, as well as it introduces the various image acceleration strategies currently available, including compressed sensing. Chapter 3 describes the validation of the neural network based tumour tracking algorithm developed at the CCI. Parts of this chapter have been published as a co-authored article in the journal *Medical Physics*. Additional experiments including intra and inter-observer variation experiments is included. Chapter 4 describes the novel MR acceleration strategy PDACS, and an important weakness of the method. Parts of this chapter have been published as a first authored article in the journal *Medical Physics*. Chapter 5 presents a modified version of PDACS, which uses a sliding window that mitigates this weakness. Parts of this chapter have been accepted for publication as a first authored article in the journal *Medical Physics*. Chapter 6 includes a conclusion and possible future directions for this research.

## Chapter 2 Theory

### 2.1 Magnetic Resonance Physics

#### 2.1.1 Spins in a Magnetic Field

The atomic nuclei are made of elementary particles (i.e. protons, neutrons) which contain a fundamental property known as magnetic spin. Atoms with nuclei containing an odd number of protons and/or an odd number of neutrons possess an intrinsic angular momentum, which gives rise to a magnetic dipole moment<sup>31</sup> vector,  $\boldsymbol{\mu}$

$$\boldsymbol{\mu} = \gamma \mathbf{S} = \gamma \hbar \mathbf{I} \quad (2.1)$$

where  $\gamma$  is a constant known as the gyromagnetic ratio ( $2.68 \times 10^8$  rad/s/T or 42.6 MHz/T for  $^1\text{H}$  protons),  $\mathbf{S}$  is the spin angular momentum,  $\hbar$  is Planck's Constant ( $1.055 \times 10^{-34}$  J.s.), and  $\mathbf{I}$  is known as the spin operator. For atomic nuclei with a non-zero magnetic dipole moment, nuclear magnetic resonance (NMR) occurs in the presence of external magnetic fields. The magnetic moment interacts with the external magnetic field, which gives rise to the energy<sup>31</sup>

$$E = -\boldsymbol{\mu} \cdot \mathbf{B} \quad (2.2)$$

where vector  $\mathbf{B}$  is the external magnetic field. If the magnetic field is applied in the z direction, that is,  $\mathbf{B} = B_0 \hat{\mathbf{z}}$ , then the energy can be calculated as

$$E = -\mu_z B_0 = -\gamma S_z B_0 = -\gamma \hbar I_z B_0 \quad (2.3)$$

From quantum mechanics it is known that  $S_z$ , the z-component of spin angular momentum, can exist only in certain quantized states, or  $\hbar I_z$ , where  $I_z$  is the spin quantum projection number. For a spin  $\frac{1}{2}$  particle such as a proton, used almost exclusively in clinical MRI,  $I_z$  can only take two possible values:  $+1/2$  or  $-1/2$ . This gives rise to a high energy "spin down" state,  $E_+$ , and a low energy "spin up" state  $E_-$ , with an energy difference of

$$\Delta E = \gamma \hbar B_0 \quad (2.4)$$

### 2.1.2 Statistical Mechanics and Net Magnetization

For each of the energy states,  $E_+$  and  $E_-$ , the fraction of particles occupying an energy state is described by the Boltzmann's distribution, which can be expressed as<sup>32</sup>

$$\frac{N_+}{N} = \frac{e^{\frac{-E_+}{k_b T}}}{Z} \quad (2.5)$$

$$\frac{N_-}{N} = \frac{e^{\frac{-E_-}{k_b T}}}{Z} \quad (2.6)$$

and

$$Z = e^{\frac{-E_+}{k_b T}} + e^{\frac{-E_-}{k_b T}} \quad (2.7)$$

is the partition function for this two state system.  $N$  is the total number of particles and,  $N_+$  and  $N_-$  are the number of particles with the energies  $E_+$  and  $E_-$ , respectively. The constant  $k_b$  is the Boltzmann's constant, and  $T$  is the temperature of the sample. Using these equations, one can calculate the ratio between these two states as follows<sup>32</sup>

$$R = \frac{N_-}{N_+} = e^{\frac{\Delta E}{k_b T}} \quad (2.8)$$

In the case where the magnetic field is at 3.0 T and a body temperature of  $T = 310\text{K}$ ,  $\frac{\Delta E}{k_b T} = 2.0 \times 10^{-5}$ ,  $R$  can be approximated, using the Taylor's series, as

$$R = e^{\frac{\Delta E}{k_b T}} \approx 1 + \frac{\Delta E}{k_b T} = 1.000020 \quad (2.9)$$

The excess amount of low energy "spin up" state will give rise to a net magnetization, given as

$$\begin{aligned} M_0 &= m(N_+ - N_-) = m(N_+ + N_-) \frac{(N_+ - N_-)}{(N_+ + N_-)} \\ &= mN \frac{R - 1}{R + 1} \end{aligned} \quad (2.10)$$

Substitution in equation 2.8, one can derive the equation

$$M_0 = mN \frac{e^{\frac{\Delta E}{k_b} - 1}}{e^{\frac{\Delta E}{k_b} + 1}} = mN \tanh\left(\frac{\Delta E}{2k_b T}\right) \quad (2.11)$$

As the argument in the hyperbolic tangent is small, the expression further simplifies to

$$M_0 \approx mN \frac{\Delta E}{2k_b T} \quad (2.12)$$

In most MR scanners, there is a strong main magnetic field applied in one direction, or,  $\mathbf{B} = B_0 \hat{\mathbf{z}}$ . If this is true, we can substitute Equation 2.1 and 2.4 into equation 2.12, which gives us the expression

$$M_0 \approx N\gamma^2 \hbar^2 \frac{B_0}{4k_b T} \quad (2.13).$$

One can observe that the magnetization of the sample is linearly dependent on the main magnetic field strength  $B_0$ . MR scanners typically operate with a strong magnetic field  $B_0$ . Even MR scanners colloquially described as "low field", such as a 0.5 T magnet, still operates at 10000x the earth's magnetic field strength.

### 2.1.3 Magnetic Precession

The interaction between magnetization vector and an external magnetic field can be described classically by the differential equation<sup>31</sup>

$$\frac{d\mathbf{M}}{dt} = \gamma \mathbf{M} \times \mathbf{B} \quad (2.14)$$

where  $\mathbf{M}$  is the vector describing the magnetization of the sample and  $\mathbf{B}$  is the magnetic field vector. Assuming again that in the MR scanner where  $\mathbf{B} = B_0 \hat{\mathbf{z}}$ , equation 2.14 can be separated into 3 components, as

$$\begin{aligned} \frac{dM_x}{dt} &= \gamma M_y B_0 \\ \frac{dM_y}{dt} &= -\gamma M_x B_0 \end{aligned} \quad (2.15)$$

$$\frac{dM_z}{dt} = 0$$

The solution of these equations yields the expressions

$$M_x(t) = M_x(0)\cos(\omega_0 t) + M_y(0)\sin(\omega_0 t)$$

$$M_y(t) = -M_x(0)\sin(\omega_0 t) + M_y(0)\cos(\omega_0 t) \quad (2.16)$$

$$M_z(t) = M_z(0)$$

If there are transverse magnetization components present, such that  $M_x$  or  $M_y$  is greater than zero, these equations describe a "spinning top" like motion known as the Larmor precession about the z axis. The frequency,

$$\omega_0 = \gamma B_0 \quad (2.17)$$

is known as the Larmor frequency. However, at the equilibrium position where  $\mathbf{M} = M_0 \hat{\mathbf{z}}$ , there are no transverse magnetization components, such that  $M_x(0) = 0$ ,  $M_y(0) = 0$ , and no spin dynamic occurs. Transverse magnetization can be generated by perturbation of the system with a radiofrequency (RF) pulse, which will be described in section 2.1.6.

#### 2.1.4 Bloch's equation and MR Relaxation

While external perturbation causes MR magnetization to precess, the system will gradually return to thermal equilibrium. This process is known as relaxation. By adding relaxation terms to Equation 2.14 yields the Bloch's equation, given as<sup>31</sup>

$$\frac{d\mathbf{M}}{dt} = \gamma \mathbf{M} \times \mathbf{B} - \frac{M_x \mathbf{x} + M_y \mathbf{y}}{T_2} - \frac{(M_z - M_0) \mathbf{z}}{T_1} \quad (2.18)$$

In Equation 2.18, there are two separate relaxation terms describing the relaxation in transverse plane and z-direction. The middle term describes transverse, spin-spin ( $T_2$ ) relaxation, in which the individual spins interacts with one another and lose coherence at a rate described by the  $T_2$  relaxation time. The last term describes the longitudinal, spin-lattice ( $T_1$ ) relaxation, a process

where spins lose energy to its surrounding environment, at a rate described by the  $T_1$  relaxation time. Separating the Bloch's equation into 3 components yields

$$\begin{aligned}\frac{dM_x}{dt} &= \gamma M_y B_0 - \frac{M_x}{T_2} \\ \frac{dM_y}{dt} &= -\gamma M_x B_0 - \frac{M_y}{T_2} \\ \frac{dM_z}{dt} &= \frac{M_0 - M_z}{T_1}\end{aligned}\tag{2.19}$$

with the solution

$$\begin{aligned}M_x(t) &= [M_x(0)\cos(\omega_0 t) + M_y(0)\sin(\omega_0 t)]e^{-\frac{t}{T_2}} \\ M_y(t) &= [-M_x(0)\sin(\omega_0 t) + M_y(0)\cos(\omega_0 t)]e^{-\frac{t}{T_2}} \\ M_z(t) &= M_0 + (M_z(0) - M_0)e^{-\frac{t}{T_1}}\end{aligned}\tag{2.20}$$

### 2.1.5 Rotating Frame of Reference

The equations describing MR physics can be greatly simplified if these are expressed in a frame of reference that is rotating about the z-axis at the Larmor frequency. In this frame of reference, there is no precession from the static field, so the effective static  $B_0$ , or  $B_{eff} = 0$ , the cross product term in the Bloch equation is zero. The solutions of the Bloch equations are greatly simplified to<sup>31</sup>

$$M_x(t) = M_x(0)e^{-\frac{t}{T_2}}\tag{2.21}$$

$$M_y(t) = M_y(0)e^{-\frac{t}{T_2}}$$

$$M_z(t) = M_0 + (M_z(0) - M_0)e^{-\frac{t}{T_1}}$$

Generally, equations describing MR signals will be expressed in the rotating frame of reference.

### 2.1.6 RF ( $B_1$ ) Tipping Pulse

As mentioned previously, the net magnetization in equilibrium does not precess, however, MR magnetization within a sample can be made to precess by applying a transverse  $B_1$  RF field to the sample. In the rotating frame of reference, the magnetization vector  $\mathbf{M}$  can be rotated out of its equilibrium position, along z direction in the rotating frame of reference, by the application of a magnetic field  $B_1$  in a direction orthogonal to the z-axis (i.e. either in x or y direction). The angle of rotation,  $\alpha$  of the magnetization vector  $\mathbf{M}$  is described by the equation<sup>32</sup>

$$\alpha = \gamma B_1 \tau \quad (2.22)$$

where  $\tau$  is the time during of RF ( $B_1$ ) pulse (RF pulse at the Larmor frequency), the rotation angle  $\alpha$  is sometimes called the ``flip angle``. After the magnetization has rotated away from equilibrium, it undergoes precession and relaxation as described by the Bloch's equation. The transverse component of the magnetization can be detected by placing one or more receiver coils along either x or y direction. Generally, the signal induced in the receiver coil is the largest for a flip angle of  $90^\circ$ . The time-dependent voltage detected by the receiver coil after the application of a single  $B_1$  pulse is called the free-induction decay (FID).

### 2.1.7 $T_2$ and $T_2^*$

After a  $90^\circ B_1$  pulse is applied to a sample, the observed signal decay is known as free induction decay (FID). One might expect the FID to occur at a rate ( $T_2$ ) described by equation 2.29 and 2.30. However, the observed decay time is generally shorter than this expected value. This phenomenon is due to the local magnetic field inhomogeneity within the sample caused by small spatial variations in the  $B_0$  field. These small differences in  $B_0$  cause the spins to precess at slightly different Larmor frequencies, which causes the signal to decay at rate described by<sup>32</sup>

$$\frac{1}{T_2^*} = \frac{1}{T_2} + \gamma\Delta B \quad (2.23)$$

where  $T_2^*$  represents the shortened relaxation time, and  $\Delta B$  represents local field inhomogeneity. The term  $\gamma\Delta B$  is sometimes denoted as  $1/T_2'$ .  $T_2^*$  relaxation is therefore a combination of two different effects. Irreversible thermodynamic processes cause  $T_2$  decay whereas inhomogeneity in the external magnetic field and magnetic susceptibility differences cause reversible  $T_2'$  decay. The effect of  $T_2'$  dephasing can be reversed by applying a 180° RF pulse following the 90° excitation RF pulse which leads to the formation of a ``spin-echo``.

### 2.1.8 MR Signal Detection

The voltage induced in these coils can be described by Faraday`s law, which states that<sup>32</sup>

$$V = -\frac{d\Phi}{dt} \quad (2.24)$$

where  $\Phi$  describes the magnetic flux, which is expressed as

$$\Phi = NAB_x = \mu_oNAM_x \quad (2.25)$$

where  $N$  is the number of loops in the coil,  $A$  is the cross sectional area of the sample, and  $B_x = \mu_oM_x$  is the magnetic field in the x direction,  $\mu_o = 4\pi \times 10^{-7}H/m$  is the permeability of vacuum, and  $M_x$  magnetization in the x-direction. After a 90 degree excitation pulse where all the magnetization is on the y axis (i.e.  $M_x(0) = 0, M_y(0) = M_T(0), M_z(0) = 0$ ), the x-component from equation 2.20 simplifies to:

$$M_x = M_T \sin(\omega_0 t) \quad (2.26)$$

Where  $M_T = M_T(0)e^{-\frac{t}{T_2}}$  is the magnitude of the transverse (x,y) component of the magnetization. Therefore, the voltage induced in the coil is given as follows.

$$V = -\mu_oNA \frac{dM_x}{dt} \quad (2.27)$$

where

$$\frac{dM_x}{dt} = \left[ M_T \omega_0 \cos(\omega_0 t) + \frac{dM_T}{dt} \sin(\omega_0 t) \right] \quad (2.28)$$

The first term describes the contribution from precession (proportion to  $\omega_0$ , which is  $\sim 128$  MHz for a 3 T scanner), which is many orders magnitude larger than the second term that describes the contribution from transverse relaxation (proportion to  $1/T_2$  which is in the order of a few Hz for most tissues). Ignoring the 2<sup>nd</sup> term, the voltage induced in the coil is

$$V = -\mu_0 N A M_T \omega_0 \cos(\omega_0 t) \quad (2.29)$$

One can therefore observe that the amount of induced voltage is proportional to  $B_0^2$  as both the net magnetization  $M_T$  and the Larmor frequency  $\omega_0$  are linearly dependent on  $B_0$

## 2.2 Imaging Principles

The previous section discussed the use of an RF pulse to tip away the net magnetization of the sample from z-axis to the transverse plane and the signal induction by the transverse magnetization within a receiver coil. However, in order to visualize anatomy in 2D or 3D images, spatial localization of samples that produce MR signal must be performed.

### 2.2.1 Fourier Transform

The Fourier transform is an important mathematical operation that decomposes a function into its constituent frequencies, and is also an important concept in for MR imaging. The Fourier transform in 1-D is defined as follows

$$F(k) = \int_{-\infty}^{+\infty} dx f(x) e^{-2\pi i x k} \quad (2.30)$$

The function  $f(x)$  describes the variation of image intensities in spatial domain whose Fourier transform is given by the function  $F(k)$ . Both functions are assumed, in general, to be complex. Conceptually,  $F(k)$  is the frequency spectrum of  $f(x)$ . The original function  $f(x)$  can be mathematically recovered from  $F(k)$  by applying the inverse Fourier transform, described as,

$$f(x) = \int_{-\infty}^{+\infty} dk F(k) e^{2\pi i x k} \quad (2.31)$$

Equations 2.30-2.31 are the Fourier transform pairs in 1D, but these two formulations generalize to N-dimensions with straight forward extensions.

### 2.2.2 Magnetic Field Gradients

MR signals can be spatially localized by the application of linearly spatially varying magnetic fields since the Larmor frequency is linearly proportional to the total magnetic field at a point. An MR imaging device typically contains a set of gradient coils that produce linear magnetic field gradient in the three orthogonal directions. The effect of magnetic field gradients can be mathematically described as<sup>31</sup>

$$\Delta B(x, y, z) = \mathbf{r} \cdot \mathbf{G} = xG_x + yG_y + zG_z \quad (2.32)$$

where  $\Delta B$  is the additional magnetic field strength at a point  $(x, y, z)$  due to the application of linear gradient, the vector  $\mathbf{r}$  is position vector, and  $\mathbf{G}$  is magnetic field slope vector, also known as gradient strength. It is worth noting that while the gradient field  $\Delta B$  varies in the three orthogonal directions, this additional magnetic field is oriented in z-direction, parallel to  $B_0$ . Combining the main magnetic field to the gradient field yields the expression

$$\mathbf{B}(\mathbf{r}) = \hat{\mathbf{z}}(\mathbf{r} \cdot \mathbf{G} + B_0) \quad (2.33)$$

### 2.2.3 Slice Selection

In tomographic imaging, one of the three spatial dimensions is usually localized by selecting a slice (i.e. a 2D plane) or a set of slices to be imaged. In MR imaging, this is achieved through the application of a slice selective RF pulse in conjunction with gradients in any desired direction. A slice selective gradient can be applied such that the magnetization in a plane within the sample, perpendicular to vector  $\mathbf{G}$ , will precess at the same Larmor frequency. Since it is not practical to select an infinitesimally thin plane, a rectangular slice profile can be obtained by applying a *sinc* shaped RF pulse in time domain. With relatively small flip angles ( $< 90^\circ$ ), the slice profile can be approximated by taking the Fourier transform of the RF pulse shape. The *sinc* and

rectangular functions are Fourier transform pairs. The width of the rectangular function,  $\Delta\omega$  is related to the physical slice thickness,  $d$ , described by the following expression<sup>32</sup>.

$$d = \frac{\Delta\omega}{\gamma G} \quad (2.34)$$

Where the frequency bandwidth,  $\Delta\omega$ , is the difference between the maximum and the minimum precession frequencies within the rectangular slice. In some applications, other factors, such as RF energy deposition are of greater importance compared rectangular slice profile. In these cases, other RF pulse shapes (i.e. Gaussian) are used, resulting in non-rectangular slice profiles.

Finally, it should be noted that the Fourier transform relationship between the RF time domain pulse and the shape of the slice profile is only valid for the small flip angles. At larger flip angles ( $> 90^\circ$ ), the Fourier transform relationship is no longer valid, which requires specifically designed pulses to achieve the desired slice profile<sup>33</sup> (i.e. Shinnar – Le Roux method).

#### 2.2.4 Frequency Encoding and Quadrature Detection

If a linearly varying magnetic field with known gradient is applied in a direction (e.g. x-direction) orthogonal to the slice selective direction (e.g. z-direction) during acquisition, the detected time domain FID will comprise a range of frequencies. With the gradient  $G$  applied in the x-direction, the magnetization in the x-direction of the selected plane will precess at a range of frequencies. In particular, the Larmor frequency at  $x$  is  $\omega_0 + \gamma xG$ , and the voltage induced is given as follows<sup>32</sup>

$$V(t) = \int dx P(x) \cos(\omega_0 + \gamma xG) t \quad (2.35)$$

where  $P(x)$  is the projection of 2-D magnetization of the selected plane onto the x-direction. In quadrature detection, this induced voltage is split into two components each obtained by multiplication with a reference signal oscillating at the natural Larmor frequency. The reference signals of the two components are  $90^\circ$  out of phase with one other as

$$V_1(t) = V(t) \cos(\omega_0 t) = \int dx P(x) [\cos(2\omega_0 + \gamma xG) t + \cos(\gamma xG) t] \quad (2.36)$$

$$V_2(t) = V(t) \sin(\omega_0 t) = \int dx P(x) [\sin(2\omega_0 + \gamma x G) t - \sin(\gamma x G) t] \quad (2.37)$$

For each of two signal components, the high frequency component of the signal is removed by means of a low-pass filter.

$$V_1(t) = \int dx P(x) \cos(\gamma x G t) \quad (2.38)$$

$$V_2(t) = \int dx P(x) \sin(\gamma x G t) \quad (2.39)$$

The two components are generally described as the “real” and “imaginary” component of the detected signal. The two 90° out of phase signals allow one to distinguish whether the frequency is positive or negative. The combination of the two signals is a generally a complex signal given as follows.

$$C(t) = V_1(t) - iV_2(t) \quad (2.40)$$

which can be expressed as, using Euler’s formula

$$C(t) = \int dx P(x) e^{-i\gamma x G t} \quad (2.41)$$

By making the substitution  $k = \gamma G t$  in Equation 2.41, one gets the expression

$$C(k) = \int dx P(x) e^{-ikx} \quad (2.42)$$

A simple application of an inverse Fourier transform in eq.2.42 one can recover the spatially localized signal

$$P(x) = \frac{1}{2\pi} \int dk C(k) e^{ikx} \quad (2.43)$$

In summary, in frequency encoding, a magnetic field gradient is applied during data acquisition. Spatial information is recovered by the inverse Fourier transform of the resulting time-domain quadrature detected signal.

## 2.2.5 Phase Encoding

From Equation 2.41, we can extract the important physical quantity

$$\phi = \gamma x G t \quad (2.44)$$

which is known as phase. Spatial information in the direction orthogonal to the frequency encoding direction can be localized by manipulating the phase of the magnetization within the selected plane. This is known as phase encoding process which varies the phase along the phase encoding direction (i.e. y-direction) by the application of another linearly varying gradient.

For simplicity, let us say that the total magnetization is to be spatially localized at 3 different points,  $-y$ ,  $0$ ,  $y$ , with an associated magnetization of  $m_{-y}$ ,  $m_0$  and  $m_y$ , at these points, respectively. In order to achieve this, 3 frequency encoding steps, with y-direction gradients of magnitudes,  $G_y = -g$ ,  $0$  and  $g$  are applied after the slice selective z-gradient, but prior to frequency encoding gradient applied during acquisition of the time domain FID. The phase can be determined by eq. 2.44. In the first experiment, the encoding gradient  $g$  will create the phase of  $\phi = -\theta$ ,  $0$ , and  $\theta$ , where  $\theta = \gamma y g T$ , for  $m_{-y}$ ,  $m_0$  and  $m_y$ . The projection from the first experiment is

$$p_{+g} = m_{-y}e^{-i\theta} + m_0 + m_ye^{i\theta} \quad (2.45)$$

The 2<sup>nd</sup> experiment, there is no phase, the projection is therefore simply

$$p_0 = m_{-y} + m_0 + m_y \quad (2.46)$$

For the 3<sup>rd</sup> experiment, the gradient of  $-g$ , the projection is

$$p_{-g} = m_{-y}e^{i\theta} + m_0 + m_ye^{-i\theta} \quad (2.47)$$

We can define the matrix notations

$$\mathbf{F} = \begin{bmatrix} e^{i\theta} & 1 & e^{-i\theta} \\ 1 & 1 & 1 \\ e^{-i\theta} & 1 & e^{i\theta} \end{bmatrix} \quad (2.48)$$

$$\mathbf{m} = \begin{bmatrix} m_g \\ m_0 \\ m_{-g} \end{bmatrix} \quad (2.49)$$

$$\mathbf{p} = \begin{bmatrix} p_g \\ p_0 \\ p_{-g} \end{bmatrix} \quad (2.50)$$

Equations 2.45-2.47 can be written in matrix form

$$\mathbf{P} = \mathbf{F}\mathbf{m} \quad (2.51)$$

The goal is to recover the spatially localized matrix  $\mathbf{m}$  from the acquired projections  $\mathbf{P}$ , by using matrix inversion as follows.

$$\mathbf{m} = \mathbf{F}^{-1}\mathbf{P} \quad (2.52)$$

Three phase encoding gradient steps are not sufficient to generate acceptable images. For maximum computational efficiency, the number of phase encoding steps in MR imaging experiment is typically chosen as  $2^N$  numbers such as 64, 128, 256, and 512. The phase encoding gradients are chosen such that the phase increases linearly from negative maximum to positive maximum in a step-by-step manner. For 256 phase encodes (i.e. 256 frequency encoded data acquisition each with a different phase encode gradient), the elements of the matrix  $\mathbf{F}$  are defined as

$$F_{jk} = \frac{1}{\sqrt{256}} e^{-i\frac{2\pi jk}{256}} \quad (2.53)$$

The matrix  $\mathbf{F}$  and inversion matrix  $\mathbf{F}^{-1}$  are the forward and inverse discrete Fourier transform operators. The spatially localized signal (image) is a 2D inverse Fourier transform of the series of projections.

### 2.2.6 2D Signal Equation and $k$ -space

The more general formulation of time varying signal (i.e. gradient modified FID), after slice selection gradient along the  $z$  direction, and the time varying gradients along the  $x$  and  $y$  directions, is the expression known as the 2D signal equation<sup>31</sup> given as follows.

$$S(t) = \iint dx dy P(x, y) e^{-i(k_x(t)x + k_y(t)y)} \quad (2.54)$$

Where

$$k_x(t) = \gamma \int_0^t G_x(\tau) d\tau \quad (2.55)$$

and

$$k_y(t) = \gamma \int_0^t G_y(\tau) d\tau \quad (2.56)$$

Where  $k_x$  and  $k_y$  define the two orthogonal axes of  $k$ -space. Note that the time integral of the gradients  $G_x$  and  $G_y$  effectively determines  $k$ -space trajectory. In the most conventional MR studies, a sequence of varying gradients are applied, acquiring sufficient data to cover a 2D  $k$ -space,  $M(k_x, k_y)$ . MR images are reconstructed by performing a 2D inverse Fourier transform. The next section describes a few examples of such sequences.

## 2.3 Imaging Sequences: Spin Echo

### 2.3.1 Spin Echo Sequence

This section introduces several basic MRI sequences. As noted previously, an FID signal from a  $90^\circ$  RF pulse leads to  $T_2^*$  related signal losses caused by local magnetic field inhomogeneity. However, this loss is recoverable by a sequence known as the spin-echo experiment. In the spin echo experiment, the  $90^\circ$  RF excitation pulse is followed by a  $180^\circ$  RF refocusing pulse after a time  $t$ . The polarity of spins dephasing due to the local magnetic field inhomogeneity is now reversed causing them to re-phase in time. At a time precisely at  $2t$  after the  $90^\circ$  RF pulse, also known as the echo time ( $TE$ ), the phase coherence is again at the maximum, and the FID signal formed from this coherence is called an echo.

However, the de-phasing from spin-spin interaction ( $T_2$ ) is not recoverable. If only one refocusing pulse is applied, the signal dependence on  $TE$  is given as follows<sup>32</sup>,

$$S(TE) = M_0 e^{\frac{-TE}{T_2}} \quad (2.57)$$

where  $M_0$  magnetization as defined as equation 2.13. Each spin echo signal, with appropriate phase and frequency encoding gradients, represents a single line in  $k$ -space along the frequency encode direction. Multiple excitations (with different magnitudes of phase encode gradients) are required to acquire a full 2D  $k$ -space in order to generate a 2D image. The time interval between excitations is known as the repetition time (TR). Due to repeated excitations, longitudinal relaxation time ( $T_1$ ) has an impact on the overall signal. Prior to the initial excitation,  $M_z$  is at its maximum point at thermal equilibrium. A  $90^\circ$  pulse flips the magnetization vector onto the x-y plane, and  $M_z = 0$ . The spin-lattice relaxation occurs, with a time constant  $T_1$ , between consecutive excitation pulses at time intervals of TR.  $T_1$  and TR determine how much of the  $M_z$  magnetization will recover and available for the subsequent excitations. Eventually, a steady state level of  $M_z$  is achieved at the beginning of each excitation. The amount of signal available is described by

$$S(TE, TR) = M_0 \left( 1 - 2e^{-\frac{-(TR - \frac{TE}{2})}{T_1}} + e^{-\frac{TR}{T_1}} \right) e^{-\frac{TE}{T_2}} \quad (2.58)$$

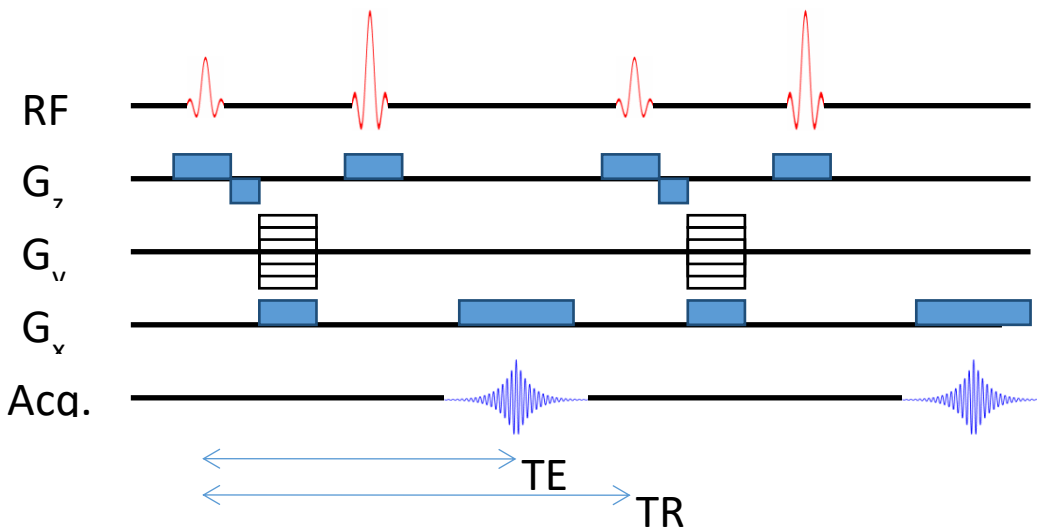


Figure 2-1: Sequence diagram for a spin echo sequence. RF describes the radiofrequency pulse,  $G_x, G_y, G_z$  describes the x, y, z gradients, and Acq. describes the acquired signal. TE is the echo time, and TR is the repetition time. The lower magnitude RF pulse is  $90^\circ$  excitation and the higher magnitude RF pulse is  $180^\circ$  re-focusing pulse that falls mid-way between  $90^\circ$  excitation pulse and the center of the acquired FID, Acq.

While  $T_1$  and  $T_2$  time constants are the inherent property of the MR sample,  $TE$  and  $TR$  times are parameters chosen by the user in the MRI experiment. The effect of spin-spin relaxation ( $T_2$ -relaxation) in the image is minimized when  $TE \ll T_2$ , while the effect of spin-lattice relaxation ( $T_1$ -relaxation) is minimized when  $TR \gg T_1$ . Hardware limits, such as gradient strength (i.e. magnitude of the slope of the linearly varying magnetic field) of an MR system, limits the minimum  $TE$ , while scan time limits the maximum  $TR$ , as the total scan time required for a spin echo sequence to generate an image is given as follows.

$$\text{Scan Time} = N_{pe} * TR \quad (2.59)$$

Where  $N_{pe}$  is the number of phase encode lines, or the number of  $k$ -space lines.

### 2.3.2 Turbo Spin Echo Sequences

At times after the data acquisition at  $t = TE$ , the spin system in the slice plane both de-phases due to  $T_2^*$  and diminishes due to  $T_2$ -relaxation; however, there may still be adequate spin population left in the slice plane. If one then applies another phase encode gradient and a refocusing RF pulse, one can acquire another line of the  $k$ -space without flipping a renewed spin system that has relaxed in the direction orthogonal to slice plane (i.e. z-direction). This step can be repeated as long as there is adequate spin population remains in the slice plane allowing multiple  $k$ -space lines within the same  $TR$ . This approach is known as the turbo spin echo (TSE) approach. This sequence has different names among different vendors including the Fast Spin Echo (FSE) or Rapid Acquisition with Relaxation Enhancements (RARE). This sequence acquires the FID of each phase-encode with a different TE value. Therefore, the relationship of pixel values and relaxation time is not simple<sup>32</sup>. However, in applications where quantitative information about relaxation times is not important, TSE sequence offers high quality SE like images while significantly reducing the imaging time. The scan time for such a scan is

$$\text{Scan Time} = \frac{N_{pe}}{\text{TSE Factor}} * TR \quad (2.60)$$

Where the TSE factor represents the number of echoes acquired per excitation, i.e. in each  $TR$ .

## 2.4 Imaging Sequences: Gradient Echo Imaging

### 2.4.1 Spoiled Gradient Echo Sequence

To further reduce the data acquisition time for an image, a whole family of gradient echo based sequences has been developed. In a gradient echo sequence, only RF excitation pulse of a specified flip angle is used in a fixed interval of time ( $TR$ ). The magnetization undergoes relaxation before the next excitation. After some initial pulses, the spin system gradually reaches a steady state in which each RF pulse produces the same amount of magnetization in the transverse plane. Instead of refocusing spins by  $180^\circ$  RF pulse, echoes are formed by the dephasing and re-phasing of spins by the application of the reversed frequency encoding gradient. As there is no  $180^\circ$  refocusing, the  $T_2'$  effect is not reversed. As a result, gradient echo sequence is  $T_2^*$  weighted rather than  $T_2$  weighted. A version of the spoiled gradient echo sequence with gradient spoiling is shown in Figure 2-4. RF pulses with phase cycling are another means to achieve spoiling. The purpose of spoiling is to remove the remaining transverse signal at the end of each excitation to create  $T_1$  weighting in the image. This sequence is also known as  $T_1$ -FFE or FLASH. The signal acquired in the spoiled gradient echo sequence is described by the following expression<sup>33</sup>.

$$S = \frac{M_0 \sin \theta (1 - e^{-TR/T_1})}{(1 - \cos \theta e^{-TR/T_1})} e^{-\frac{TE}{T_2^*}} \quad (2.61)$$

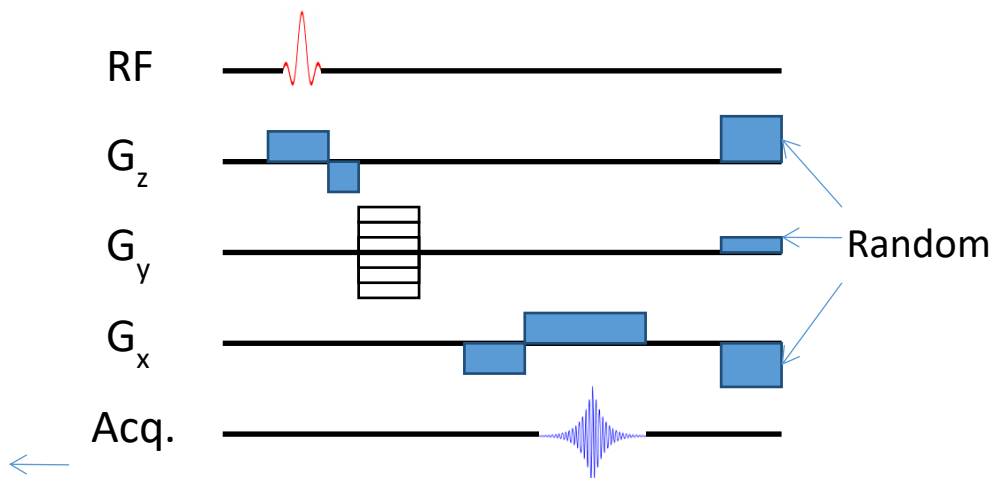


Figure 2-2: Sequence diagram of the spoiled gradient echo sequence. Random gradients are employed to spoil the remaining transverse magnetization at the end of each TR interval.

It should be noted that the scan time of a gradient echo sequence can be expressed with the same expression as spin echo sequence as follows.

$$\text{Scan Time} = N_{pe} * TR \quad (2.62)$$

However, the scan time of gradient echo sequences can be significantly reduced by using a much shorter TR with a small flip angle. When TR is short, a 90° RF pulse will not provide maximum signal, as there is not enough time for the longitudinal component to recover. An optimal flip angle to generate maximum signal in steady state is known as the Ernst angle, described as follows<sup>33</sup>.

$$\alpha_{opt} = \arccos(e^{-\frac{TR}{T_1}}) \quad (2.63)$$

#### **2.4.2 SSFP-FID and SSFP-Echo**

Compared to the spoiled gradient echo sequence, which sacrificed some signal for enhanced T<sub>1</sub> contrast, an unspoiled, steady state free precession (SSFP) sequence makes a greater amount of signal available than spoiled gradient echo. A necessary step in the SSFP sequence is a re-winder phase encoding gradient (G<sub>y</sub> in Figure 2-3). Two different signals can be acquired from SSFP sequence. The SSFP-FID is formed from the FID of each excitation pulse. SSFP-FID has more signal but less T<sub>1</sub> contrast compared to the spoiled gradient echo. On the other hand, the SSFP-echo, a time reversed FID, that appears before each excitation pulse due to the refocusing effect of consequence RF pulses. SSFP-echo sequence has more T<sub>2</sub> contrast compared to SSFP-FID. An example of SSFP-FID and SSFP-echo sequence is shown in Figures 2-5

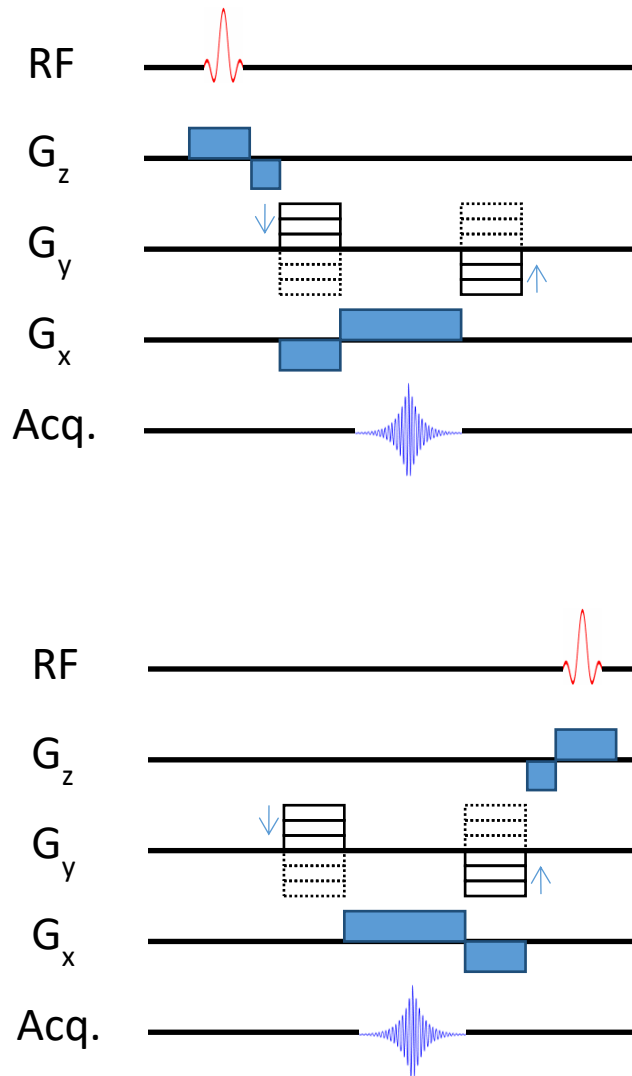


Figure 2-3: Sequence diagram for the SSFP-FID sequence (Top) and the SSFP-echo sequence (Bottom). They are mirror image of each other

### 2.4.3 Balanced SSFP

Balanced SSFP (bSSFP) incorporates a SSFP sequence in which the net area under gradients on any axis is zero in each  $TR$  interval, as shown in Figure 2-6. The signal peaks from the SSFP-FID and the SSFP-echo will coincide in-time with each other to create a signal that is a coherent sum of the two separate signals. Thus a signal larger in magnitude is produced compared to the other SSFP sequences. The signal of a bSSFP sequence can be expressed as follows<sup>33</sup>.

$$S = M_0 \sin\theta \frac{1 - E_1}{1 - (E_1 - E_2)\cos\theta - E_1 E_2} e^{-\frac{TE}{T_2}} \quad (2.64)$$

Where  $E_1$  and  $E_2$  are equal to  $e^{-\frac{TR}{T_1}}$  and  $e^{-\frac{TR}{T_2}}$  respectively. In cases where  $TR \ll T_2$ , the equation simplifies to

$$S = \frac{M_0 \sin\theta}{T_1/T_2 (1 - \cos\theta) + (1 + \cos\theta)} e^{-\frac{TE}{T_2}} \quad (2.65)$$

Due to the  $T_1/T_2$  term in the denominator of Eq. 2.65, bSSFP is often described to have  $T_2/T_1$  contrast weighting. Also, one can observe from the term “ $e^{-\frac{TE}{T_2}}$ ” that the bSSFP sequence is  $T_2$  weighted rather than being  $T_2^*$  weighted<sup>33</sup>. Proof of  $T_2$  weighting was given by Scheffler and Hennig<sup>34</sup> for the case where  $TE = TR/2$ , a condition satisfied in most applications of bSSFP. The optimal flip angle for maximum signal for bSSFP is given as follows<sup>33</sup>.

$$\theta_{max} = \arccos\left(\frac{T_1 - T_2}{T_1 + T_2}\right) \quad (2.66)$$

Another important characteristic of this sequence is the presence of banding artifacts. Local field inhomogeneity creates unwanted phase to be accumulated during each TR cycle. A low signal region (a band) occurs when the accumulated phase is  $180^\circ$ . As phase accumulation is proportional to  $TR$ , a shorter  $TR$  is an effective method to reduce banding artifacts. Due to the presence of increased field inhomogeneity at high fields scanners, banding artifacts can be quite severe in high field MRI. Balanced, SSFP sequence is inherently more suitable for imaging at lower static magnetic fields.

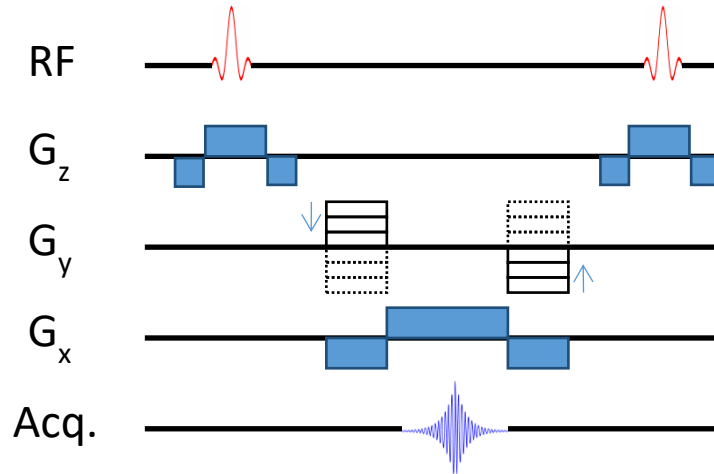


Figure 2-4: Sequence diagram for the balanced SSFP sequence.

## 2.5 Signal, Noise, Contrast

### 2.5.1 Signal-to-Noise Ratio

The discussion in the previous sections was confined to the magnitude of the MRI signal available in each of the MRI sequence. However, the presence of noise in the acquired signal is an important factor as the noise in the data propagates as noise in the MR images. Large random fluctuations in MRI images are detrimental to the image quality. Noise in the acquired FID arises from Brownian (thermal) motion of electrons in a conductive material, which is also known as resistance noise<sup>31</sup>. Noise arises from both resistance in the coil and the imaged sample. In the presence of such noise, an important indicator of image quality is the signal to noise ratio (SNR) defined as follows.

$$\text{SNR} = \frac{\text{Signal Amplitude}}{\text{standard deviation of noise}} \quad (2.67)$$

Where the ‘signal magnitude’ is usually the mean pixel intensity of a region of interest in the image, and the standard deviation of noise is measured by calculating the standard deviation in a region of the image with uniform signal. Recall that in quadrature detection, MR signal is a complex quantity with real and imaginary components required for Fourier transform. After Fourier transform, complex images with real and imaginary components are generated. While real and imaginary images have little physical meaning individually, they can be combined to calculate magnitude and phase images. The scalar magnitude images are the images most commonly used in clinical MRI. However, one must be careful in measuring noise from the

magnitude images. Due to the manner in which magnitude signal is calculated, the noise in the magnitude images follows a probability distribution resembling a Rician distribution (non-negative). If noise is measured in the magnitude images of a uniform phantom in regions where  $SNR > 2$ , the Rician and Gaussian distributions are approximately equal and no correction would be needed<sup>35</sup>. As patients are generally non-uniform, the noise would be best measured in a region outside the patient image where there is no signal. In such instances ( $SNR < 2$ ), the Rician distribution becomes a Rayleigh distribution, and the measured standard deviation will not be representative of the noise in the high SNR region of interest within the patient image. A correction factor, thus, must be applied. The noise characteristics for phased array coils are more complicated, and are beyond the scope of this work.

The problem of noise bias can be avoided if noise is measured in a zero signal region in the real or imaginary images where negative values are allowed.

The overall SNR depends on many factors, which can be summarized in the following equation<sup>31</sup>.

$$SNR \propto \Delta x \Delta y \Delta z \sqrt{\text{total readout interval}} f(\rho, T_1, T_2) \quad (2.68)$$

Where,  $\Delta x$ ,  $\Delta y$ ,  $\Delta z$ , represents the voxel dimension, the readout interval term describes the number of excitations and the number of encoding steps on each dimension, and the  $f(\rho, T_1, T_2)$  is a sequence dependent function, such as eq. 2.58 for spin echo images, eq.2.61 for FLASH and eq. 2.64 for bSSFP sequences. The proton density term  $\rho$  is built into  $M_0$  in those equations.

### 2.5.2 Contrast to Noise Ratio

The key objective in many applications of MR imaging is to distinguish between diseased and healthy tissues. The signal in both the diseased and healthy areas will fluctuate due to the noise. The difference in the mean signals of two types of tissue is known as contrast. However, this mean signal difference must be larger than the standard deviation of the noise in order for the two tissues to be visually distinguished; the larger the signal difference compared to noise standard deviation the better is visualization. The concept of contrast to noise ratio (CNR) is

thus introduced as a quantitative measure of image quality. Assuming uniform noise over the imaging field of view, CNR is defined as

$$\text{CNR} = \frac{\text{Signal Difference}}{\text{standard deviation of noise}} = \Delta\text{SNR} \quad (2.69)$$

In the context of lung tumour tracking, CNR is an important quality that describes the ability of imaging system to distinguish a lung tumour from healthy lung parenchyma tissues in the presence of imaging noise. Tumour and normal tissues may exhibit differences in  $\rho$ ,  $T_1$  and  $T_2$ , giving rise to differences in SNR (eq. 2.68).

## 2.6 Effects of Changing Main Magnetic Field Strength

### 2.6.1 SNR Dependence on $B_0$

The effect of varying the main magnetic field strength ( $B_0$ ) on image quality is an important aspect of this thesis. Eq. 2.29 shows that the induced voltage in an MR experiment is proportional to both the sample's magnetization and the precession frequency which, in turn, are both linearly proportional to  $B_0$  (Eqs. 2.13 and 2.17). Thus the MR signal amplitude is proportional to  $B_0^2$ . However, MR noise also depends on  $B_0$ , but in a more complex manner. MR noise, as previously described, comes from two sources: resistance from the coil; and resistance from the body. Noise arising from the body has been shown to be proportional to  $B_0$ , whereas noise arising from the coil is known to be proportional to  $B_0^{\frac{1}{4}}$ <sup>31</sup>. If either coil noise or body noise is dominant, the relationship between SNR and  $B_0$  can be approximated as follows.

$$\text{SNR} \propto B_0 \quad (2.70)$$

$$\text{SNR} \propto B_0^{\frac{7}{4}} \quad (2.71)$$

Where expression 2.70 represents the SNR relation when resistance from the body is the dominant factor, while equation 2.71 represents the relationship when coil resistance is the dominant effect. In typical MR coils used for imaging patients, for lower field strength (i.e. roughly 0.2 T or less), coil noise dominates and equation 2.70 is used to estimate the relationship between SNR and  $B_0$ ; whereas for higher field strengths (i.e. roughly 0.2T or more), body noise dominates and equation 2.71 is used to estimate the relationship between SNR and  $B_0$ <sup>36</sup>. For

example, going from 3 T to 0.5 T would mean a reduction of SNR by a factor of 6. These relationships are often used to justify the modification of an image acquired at a higher field strength to simulate an image acquired at lower field. SNR can be downgraded by the addition of zero mean Gaussian random number to the image. This process does not modify the signal amplitude but increases noise, resulting in a reduction of SNR and CNR. The previous example of scaling from 3 T to 0.5 T will suggest that the noise be amplified by a factor of 6. This process will be described in this work as *linear SNR/CNR scaling* to  $B_0$ .

It should be noted that expressions 2.70 and 2.71 do not account for any potential changes in relaxation times of a tissue when the main magnetic field is lowered. This issue is described in details in the next section.

### 2.6.2 Relaxation Values Dependence on $B_0$

$T_1$  relaxation time is known to be dependent on  $B_0$ , while  $T_2$  relaxation time is known to be relatively independent of it<sup>37</sup>. The relaxation of spin system in MR experiment is largely caused by fluctuating magnetic fields at the sites of nuclear spins. The tumbling motion of a molecule can be characterized by its correlation time  $\tau_c$ , which is the average amount of time required by the molecule to rotate by approximately 1 radian. The spectral density function  $J(\omega) = \frac{\tau_c}{1+\omega^2\tau_c^2}$  describes the probability that a molecule  $\tau_c$  with is rotating at a frequency  $\omega$ . In systems where the fluctuations are rapid such as the case of liquid water, the spectral density is broad, whereas in systems where the fluctuations are very slow (such as water molecules bound in very tight spaces), the spectral density is narrow<sup>38</sup>. Most tissues are within the intermediate region between these two extremes. A few sample spectral density curves are shown in Figure 2-7.

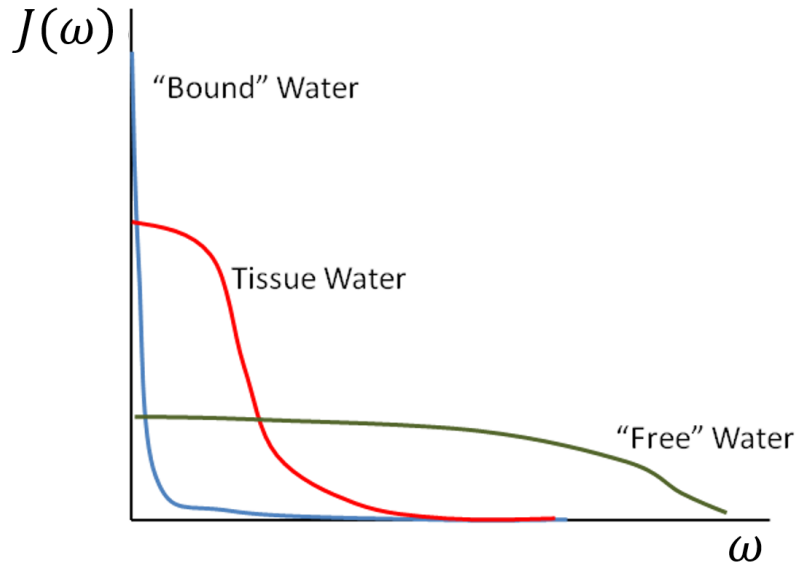


Figure 2-5: Sample spectral density for protons in 3 different environments. Blue curve represents protons in a tightly bound environment, green curve represents protons in free water, and the red curve represents water in most tissues, which is an intermediate between the other two extreme cases.

For NMR protons, spinning at Larmor frequency  $\omega_0$ ,  $T_1$  and  $T_2$  relaxation efficiencies are dependent on the tumbling frequencies of its environment. For pure substances, the relaxation times can be calculated from these spectral density curves using the Solomon-Bloembergen equations as follows<sup>38</sup>

$$\frac{1}{T_1} = \text{const} * [J(\omega_0) + 4J(2\omega_0)] \quad (2.72)$$

$$\frac{1}{T_2} = \text{const} * [3J(0) + 5J(\omega_0) + 2J(2\omega_0)] \quad (2.73)$$

When  $B_0$  is increased, the Larmor frequency will increase proportionally. The spectral density function has a lower value at higher frequency, which leads to an increase in  $T_1$ . For  $T_2$  relaxation, however, the effect is much less pronounced, because of the presence of the term -  $J(0)$  which is independent of  $B_0$ . In tissue relaxation studies with varying  $B_0$ ,  $T_1$  is generally modelled with the function<sup>37</sup>

$$T_1(\omega_0) = a\omega_0^b \quad (2.74)$$

where  $\omega_0$  is the Larmor frequency which scales linearly with  $B_0$ . Constants ‘a’ and ‘b’ differ for each types of tissues, and  $T_2$  is generally assumed to be constant<sup>37</sup>.  $T_2^*$ , as described previously, is dependent on local field inhomogeneity. In some tissues, such as the lung parenchyma, the magnetic susceptibility gradients between air and tissue are the main sources of local magnetic field inhomogeneity. The magnetic field inhomogeneity scales with  $B_0$ , as follows.

$$\Delta B = \Delta\chi B_0 \quad (2.75)$$

In these tissues, the local susceptibility differences  $\Delta\chi$  are significant, and increasing the field strength would have the effect of shortening  $T_2^*$  relaxation times. The dependence of relaxation values on field strength means that the Eqs. 2.67 and 2.68 do not completely describe the relationship between SNR and  $B_0$

## 2.7 *k*-space Sampling

In section 2.2.6, we briefly introduced the concept of the *k*-space domain, in which MRI coil data are collected, in the form of  $M(k_x, k_y)$ , prior to Fourier transform into MR images containing relaxation weighted proton density distributions. It should be noted that while the MR signal is continuous, the data are quantized and sampled at discrete locations. For a typical conventional MR sequence with regular sampling intervals, the sampled *k*-space data  $\widehat{M}$  can be expressed as<sup>31</sup>

$$\widehat{M}(k_x, k_y) = M(k_x, k_y) \left( \frac{1}{\Delta k_x \Delta k_y} \right) \text{III}_{2D} \left( \frac{k_x}{\Delta k_x}, \frac{k_y}{\Delta k_y} \right) \Pi_{2D} \left( \frac{k_x}{W_{k_x}}, \frac{k_y}{W_{k_y}} \right) \quad (2.76)$$

In this equation, the 2 dimension Dirac comb function,  $\text{III}_{2D} \left( \frac{k_x}{\Delta k_x}, \frac{k_y}{\Delta k_y} \right)$ , represents sampling density, with the spacing between each tooth of  $\Delta k_x$  along the  $k_x$  direction and of  $\Delta k_y$  along the  $k_y$  direction. On the other hand, the 2D rectangular function defines the maximum range of sampling, with the maximum width in  $k_x$  of  $W_{k_x} = 2 \left( k_{x,max} + \frac{\Delta k_x}{2} \right)$  and the maximum width in  $k_y$  of  $W_{k_y} = 2 \left( k_{y,max} + \frac{\Delta k_y}{2} \right)$ .

As stated previously, the image is reconstructed by taking a 2D Fourier transform of  $\widehat{M}(k_x, k_y)$ . In the images space, the multiplications equation 2.76 is now represented as convolutions, as follows.

$$\widehat{m}(x, y) = m(x, y) \otimes_{2D} \text{III}_{2D}(\Delta_{k_x} x, \Delta_{k_y} y) \otimes_{2D} \text{SINC}(W_{k_x} x) \text{SINC}(W_{k_y} y) \quad (2.77)$$

Where the desired image  $m(x, y)$  are now convolved with a dirac comb function of width  $1/\Delta_{k_x}$  and  $1/\Delta_{k_y}$ , which creates copies, or aliasing of the desired image, as well as the *sinc* functions which blur the images.

### 2.7.1 Field of View and the Nyquist Criterion

The field of view of a particular image is defined as the distance at which the image is replicated in real-space due to the COMB sampling in  $k$ -space, which is given as follows<sup>31</sup>.

$$\text{FOV}_x = \frac{1}{\Delta_{k_x}} = \frac{1}{\frac{\gamma}{2\pi} G_x \Delta t} \quad (2.78)$$

$$\text{FOV}_y = \frac{1}{\Delta_{k_y}} = \frac{1}{\frac{\gamma}{2\pi} \Delta G_y \tau} \quad (2.79)$$

The difference in  $\text{FOV}_x$  and  $\text{FOV}_y$  in 2.78 and 2.79 is due to the fact that readout gradient  $G_x$  is constant for the acquisition, hence the separation between sampling points in frequency encode direction (x-axis) is dependent on the time period  $\Delta t$  between subsequent A/D conversions. On the other hand, along the phase encode gradient direction (y-axis), the sampling period between phase encode lines is dependent on the increment changes in gradient strength  $\Delta G_y$ , which is turned on for a fixed time  $\tau$ .

In most commercial MRI systems, the readout direction is oversampled, as there is usually no time penalty for doing so, there is usually no aliasing along this direction. On the other hand, increasing sampling in the phase encode direction tend to increase the overall scan time (see Eqs 2.59 and 2.62). To prevent aliasing in the phase encode direction, the MR equivalent of the Nyquist Criterion is simply given as

$$d_y < \text{FOV}_y \quad (2.80)$$

where  $d_y$  represents the maximum length of the imaged object along the phase encode direction, since commercial systems allow the user to choose the FOV, one simply chooses a FOV larger than the imaged object to prevent aliasing, with potential implications on both the scan time and nominal voxel size, which is discussed in the next section.

### 2.7.2 Spatial Resolution and Voxel Size

The ability to resolve small object (i.e. spatial resolution) is related to the voxel size of the images. The voxel size of the image is typically characterized as follows<sup>31</sup>.

$$\Delta x = \frac{1}{W_{k_x}} = \frac{1}{\Delta_{k_x} N_{read}} = \frac{\text{FOV}_x}{N_{read}} \quad (2.81)$$

$$\Delta y = \frac{1}{W_{k_y}} = \frac{1}{\Delta_{k_y} N_{pe}} = \frac{\text{FOV}_y}{N_{pe}} \quad (2.82)$$

Recall from equations 2.59 and 2.62 that the scan time for spin echo and gradient echo sequences is given as follows.

$$\text{Scan Time} = N_{pe} * TR$$

Hence, scan time can be reduced by using a gradient echo sequence to shorten TR, or by reducing  $N_{pe}$ . The example shown in Figure 2-6 is a case where  $N_{pe}$  is quartered, by sampling only 1-quarter of central  $k$ -space. If the sampling period  $\Delta_{k_y}$  is maintained, voxel size will be quadrupled along that direction, while  $\text{FOV}_y$  is maintained, as shown in the blurred image in the second row of Figure 2-6. Alternatively,  $\Delta_{k_y}$  can be quadrupled to maintain the voxel size, but  $\text{FOV}_y$  will be quartered as a result, as shown in the aliased image in the 3<sup>rd</sup> row of Figure 2-6. By making the substitution to 2.82, we derive an intuitive relationship between the inherent trade off with respect to scan time, voxel size and FOV, expressed as follows.

$$\text{Scan Time} = TR \frac{\text{FOV}_y}{\Delta y}. \quad (2.83)$$

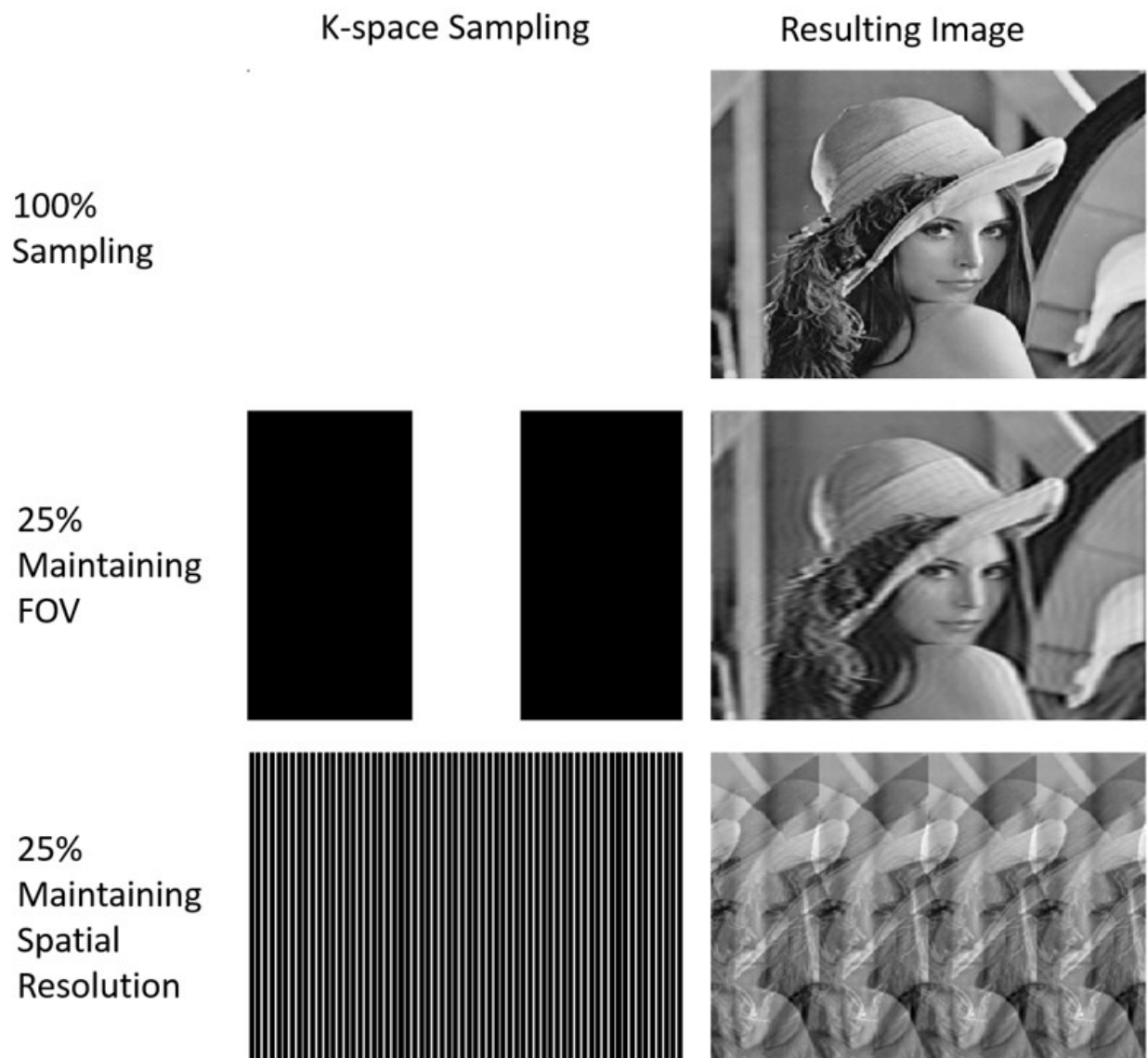


Figure 2-6: A demonstration of how various reductions of  $N_{pe}$  affect the fully sampled image in the first row. Second row represents the acquisition of central 25% of  $k$ -phase encode lines while maintaining  $\Delta_{k_y}$  and FOV, resulting in a loss in resolution. Third row represents 25% sampling over the entire  $k$ -space while increasing  $\Delta_{k_y}$  by 4 folds in order to maintain FOV, which leads to aliasing versions of base image within the FOV. Un-sampled locations are zero filled to maintain nominal resolution.

## 2.8 MR Acceleration

The fast sequences introduced in the previous section, such as turbo spin echo, or gradient echo techniques shorten MR acquisition time by acquiring the full  $k$ -space data in a more efficient manner, either via acquiring multiple lines of  $k$ -space within a single TR in the case of TSE or having very short TR's in the case of gradient echo. However, these fast techniques can be further sped up by reconstructing images with only partial  $k$ -space acquisition, which reduces

$N_{pe}$  and hence, the scan time. Generally speaking, the act of trading spatial resolution for speed (second row of Figure 2-6) is not considered to be an MR acceleration technique. Therefore, in this work, an MR acceleration technique is defined as means to increase  $k$ -space acquisition speed by partial  $k$ -space sampling while maintaining nominal spatial resolution i.e. the methods that increase  $\Delta_{k_y}$ .

In partial  $k$ -space sampling, the degree of under-sampling is inversely related to the acceleration factor. For example, if an image is acquired with only 50%  $k$ -space, the acceleration factor will be 2, if the image is acquired with 20%  $k$ -space, the acceleration will be 5x.

### **2.8.1 Regular Under-sampling and Parallel Imaging**

The aliased image in Figure 2-6 appears a very poor representation of the original fully sampled image. However, techniques have been developed such that aliasing artifacts that arise from regular under-sampling of  $k$ -space can be removed by the use of multiple element array coils. Since the 1980's<sup>39</sup> multiple array coils have been proposed as means to provide encoding information for MRI. The most ambitious proposal<sup>40</sup>, called massively parallel approach, phase encoding is completely replaced with as many coil elements. In this approach, to replace 128 phase encodes, one would require at least 128 different coil elements. Thus far, this has yet to become clinically feasible. Currently, a much more popular approach is to take advantage of the encoding power of a modest number of array coils (i.e. 6-8) to accelerate MR acquisition in a method known as the parallel imaging. There are two general approaches to solve this problem; one based is on unfolding the artifact in the image domain, the other is based on filling the missing  $k$ -space lines using encoding information from the coil elements.

Consider a very simple case of a 2 coil system shown in Figure 2-7.

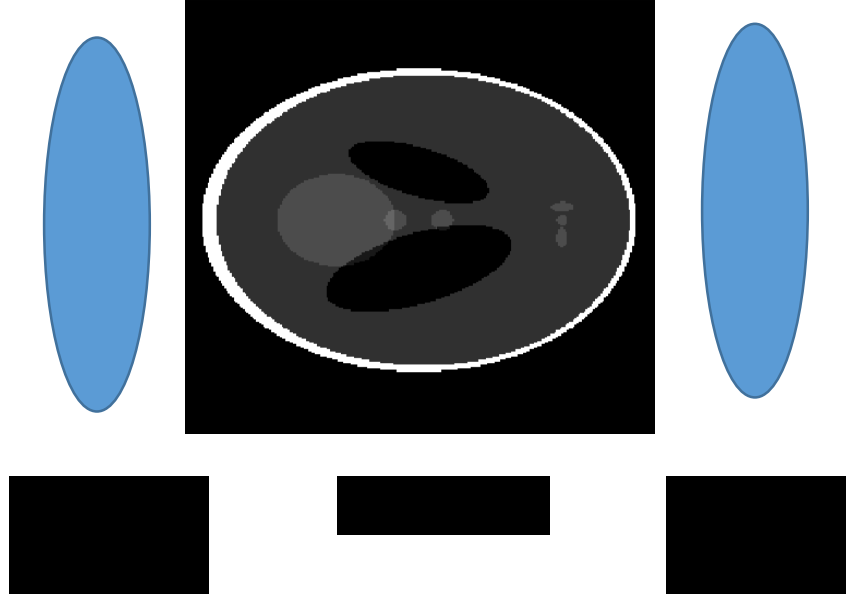


Figure 2-7 – A schematic diagram, describing a hypothetical 2 coil system positioned around a digital phantom. Each coil element is inherently more sensitive towards signals originating from regions that are closest to it. This is can be described by the coil’s sensitivity profile,  $S(x,y)$ . The reconstructed pixel value from the  $j^{\text{th}}$  element coil can be described as  $D_j(x,y) = S_j(x,y) * \rho(x,y)$ , where  $\rho(x,y)$  represents the “true” value of the pixel determined by the amount of magnetization present. The (theoretical) representation of  $D_j$ , and  $S_j$  of the system is shown in Figure 2-8.

### 2.8.1.1 Sensitivity Encoding (SENSE)

The following describes the simplest implementation of the image domain based acceleration strategy, SENSE<sup>41</sup>. Consider a regular under-sampling factor of 2, in which the missing k-space points are NOT filled with zeros, the resulting reconstruction is a reduced FOV image with the signal outside the FOV folded on to the other side of the image (Figure 2-2). Each point of detected signal is a contribution from two distinct points from the original image as shown below.

$$D_1(x,y) = S_1(x,y)\rho(x,y) + S_1(x,y \pm FOV/2)\rho(x,y \pm FOV/2) \quad (2.84)$$

$$D_2(x,y) = S_2(x,y)\rho(x,y) + S_2(x,y \pm FOV/2)\rho(x,y \pm FOV/2) \quad (2.85)$$

Note the  $\pm$  sign, if  $y < 0$ , the + sign is used, if  $y > 0$ , the negative sign is used. In this system of equations for a given pixel at  $(x,y)$ , the unknowns are  $\rho(x, y)$  and  $\rho(x, y \pm FOV/2)$ , while the remaining parameters are known. This is a system of two equations with two unknowns, which could be solved algebraically. This procedure will need to be repeated to solve for all values of  $\rho(x, y)$  to reconstruct the entire image.

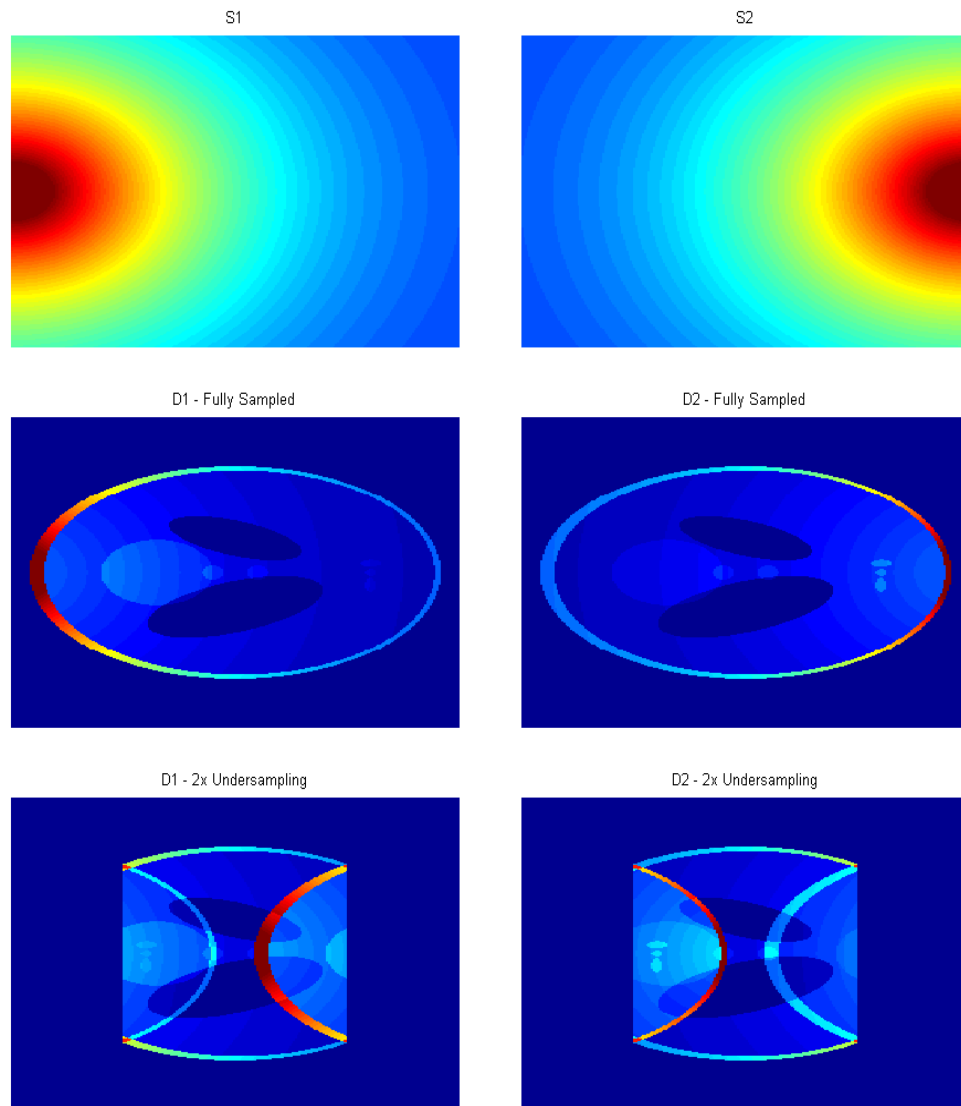


Figure 2-8 - First row: Theoretical Sensitivity maps for coil1 (left) and coil 2(right). Second row: detected signal for each coil when k-space is fully sampled and Third Row: detected signal for each coil when k-space is under-sampled by 50% along the phase encode direction.

### 2.8.1.2 Limits to Acceleration

With an acceleration factor of 2, the effective FOV is halved, and the maximum number of fold-over represented in a single point in the aliased image is 2. Hence, equation 2.1 is sufficient to unfold all the points in the image. However, if the acceleration factor is increased to an arbitrary number,  $N_f$ , there will be a maximum of  $N_f$  total fold-overs. The number of coils  $N_c$  will need to be greater or equal to  $N_f$ . The general expression for this system of equations is as follows.

$$\mathbf{D} = \mathbf{S}\boldsymbol{\rho} \quad (2.86)$$

Where  $\mathbf{D}$  is now a matrix with  $N_c \times 1$  matrix representing the data acquired from each coil element.  $\mathbf{S}$  is a  $N_c \times N_f$  matrix representing the sensitivity data for each coil at each fold-over location, and  $\boldsymbol{\rho}$  is a  $N_f \times 1$  matrix representing the unfolded data.  $\mathbf{D}$  and  $\mathbf{S}$  are known, and the SENSE problem becomes one inverting the matrix  $\mathbf{S}$  to solve for  $\boldsymbol{\rho}$ .

Another problem that arises from performing the SENSE reconstruction is the geometric positions of coils. Let's solve for equation 2.84/2.85 for  $\rho(x, y)$ . For brevity,  $D_1(x, y)$  is now expressed as  $D_1$  while  $D_1(x, y \pm FOV/2)$  is expressed as  $D_{1\Delta}$ , and so on, the solution for  $\rho(x, y)$  and  $\rho(x, y \pm FOV/2)$  are

$$\rho = \frac{D_1 S_{2\Delta} - D_2 S_{1\Delta}}{S_1 S_{2\Delta} - S_2 S_{1\Delta}} \quad \rho_{\Delta} = \frac{D_2 S_1 - D_1 S_2}{S_1 S_{2\Delta} - S_2 S_{1\Delta}} \quad (2.87)$$

Of course, these equations are unsolvable if the denominator is zero, which may or may not occur depending on the sensitivity information. However, an interesting phenomenon also occurs if the absolute value of denominator is very small. Intuitively, there should be no reason that the physical magnetization  $\rho$ , should be large solely due to coil sensitivities in  $S_1 S_{2\Delta} - S_2 S_{1\Delta}$ . It follows the numerator in the right hand side (RHS) must also be small (due to the similarity of the 2 terms in the numerator). However, a problem arises when the measurement matrix  $\mathbf{D}$  also contains noise. Suppose our detected signal  $D_k$  each have an associated uncertainty (noise), now expressed as  $D_k + \delta D_k$ , the first expression in 2.87 becomes the following.

$$\rho = \frac{D_1 S_{2\Delta} - D_2 S_{1\Delta}}{S_1 S_{2\Delta} - S_2 S_{1\Delta}} + \frac{\delta D_1 S_{2\Delta} + \delta D_2 S_{1\Delta}}{S_1 S_{2\Delta} - S_2 S_{1\Delta}} \quad (2.88)$$

Note that due to the rules of error propagation, the uncertainty term in the RHS now has a positive sign. It follows that noise is amplified when  $|S_1 S_{2\Delta} - S_2 S_{1\Delta}|$  is small. Figure 2-9 shows  $|S_1 S_{2\Delta} - S_2 S_{1\Delta}|$  calculated from the hypothetical sensitivity map in Figure 2-8.

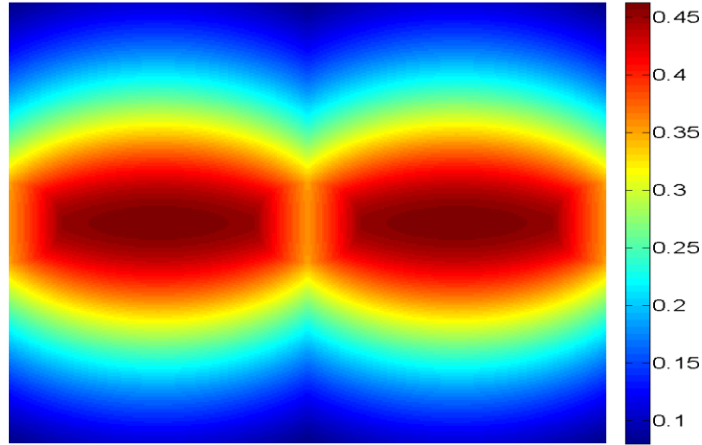


Figure 2-9 – A map describing the absolute value of the denominator  $S_1 S_{2\Delta} - S_2 S_{1\Delta}$ . Noise amplification becomes a problem when this value is low (blue).

From Figure 2-9, we can see that the regions with fold-over artifacts correspond where the denominator is relatively high in Figure 2-3, and hence the noise amplification is relatively mild. However, suppose the coil geometry is placed such that Figure 2-3 is rotated by 90 degrees – the fold-over will occur in a region with small denominator where noise amplification will be relatively large.

The notion that the quality of SENSE reconstruction (and hence SNR) is dependent on the geometric position of each pixels relative to distribution of coil elements is expressed as a term known as geometric factor,  $g^{41}$ . The SNR in SENSE reconstruction with an acceleration factor of R is expressed as follows.

$$SNR_{recon} = \frac{SNR_{full}}{g\sqrt{R}} \quad (2.89)$$

The “ideal” reduction of SNR due to reduction of sampling is represented by square root term in the denominator. This represents the loss in SNR due to the reduction of samples in the most ideal scenario. In SENSE, the geometric factor,  $g > 1$  represents an additional loss in SNR. As the acceleration factor approaches the number of coil elements, the  $g$  factor can become quite large in some regions of the image with many fold-over points.

### 2.8.1.3. *K-space based Parallel Imaging - SMASH*

A different approach to performing parallel MRI reconstruction operates in  $k$ -space, rather than in the image domain. To understand this technique, it is intuitive to look at the problem in reverse. Ideally, after the coil data has been combined, the ideal image one would get is simply  $\rho(x,y)$ . To further simplify the mathematics, only under-sampled direction is considered, i.e. the phase encode direction. The coil combined  $k$ -space point is related to the  $\rho(x,y)$  by a simple Fourier transform, or

$$D_c(k) = \int \rho(y) e^{i2\pi ky} dy \quad (2.90)$$

The adjacent points in  $k$ -space, along the phase encode direction is different by the virtue of a “phase encoding step”,  $\Delta k$

$$D_c(k + \Delta k) = \int \rho(y) e^{i2\pi ky} e^{i2\pi \Delta ky} dy \quad (2.91)$$

$$D_c(k + 2\Delta k) = \int \rho(y) e^{i2\pi ky} e^{i2\pi 2\Delta ky} dy \quad (2.92)$$

When  $k$ -space is fully sampled, both  $D_c(k)$  and  $D_c(k + \Delta k)$  are acquired. However, for an acceleration factor of 2, every second data point along the phase encode direction is missing. Simultaneous Acquisition of Spatial Harmonics, SMASH<sup>42</sup>, is a technique that attempts to estimate  $D_c(k + \Delta k)$  from  $D_c(k)$  using coil sensitivity data. The SMASH technique attempts to simulate the phase encoding information  $e^{i2\pi \Delta ky}$  by using linear combination of the coil sensitivity data. The complex exponentials  $e^{i2\pi \Delta ky}$  are simply *sines* and *cosine* functions.

Figure 2.4 shows that linear combinations of a 4-coil set up where the spatial harmonics are simulated by the coil sensitivity profiles.

The “phase encoding step”, or spatial harmonic, is replaced by the linear combination of sensitivity information as the following expression.

$$e^{i2\pi\Delta ky} = \sum_{j=1}^N W_j S(y) \quad (2.93)$$

Which is substituted in equation 2.91, yielding the following.

$$D_c(k + \Delta k) = \sum_{j=1}^N W_j \int S_j(y) \rho(y) e^{i2\pi ky} dy = \sum_{j=1}^N W_j D_j(k) \quad (2.94)$$

where  $D_j(k)$  is the acquired data for each individual coil. The weights  $W_j$  can be considered position invariant in  $k$ -space, which means the same weights can be used to estimate adjacent  $k$ -space points at any location of  $k$ -space. The determination of  $W_j$  is quite complicated and time consuming, requiring one to first acquire sensitivity profiles.

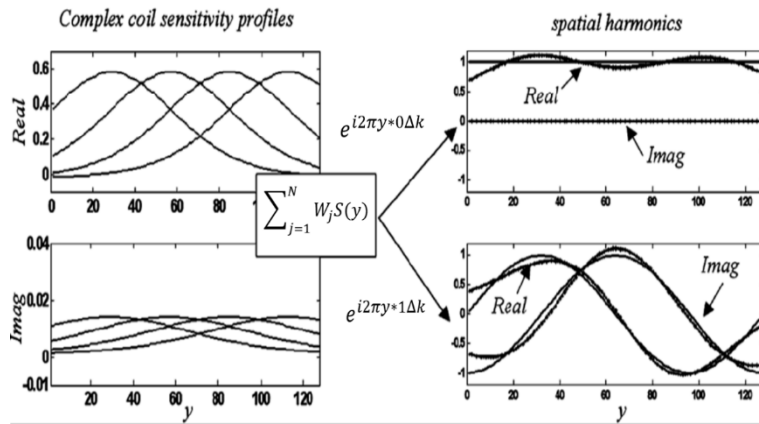


Figure 2-10 - The linear combination of 4 coil sensitivity profiles is used to simulate spatial harmonics on the right, as described in a figure adapted from Blaimer *et al*<sup>46</sup>.

#### 2.8.1.4. Auto-SMASH/VD SMASH/GRAPPA

Auto calibrated SMASH is a very convenient method to perform SMASH by eliminating the need to estimate sensitivity profiles. AUTO-SMASH<sup>43</sup> takes advantage of the positional invariance of the calibration weights, by acquiring small amount of “missing data” near the center of  $k$ -space, called the auto calibration signal (ACS), which replaces the left hand side of equation 2.94, as follows.

$$ACS = \sum_{j=1}^N W_j D_j(k) \quad (2.95)$$

Since both ACS and  $D_j(k)$  are known,  $W_j$  can be estimated by performing a best fit optimization. Variable Density (VD) SMASH<sup>44</sup> improves the accuracy of weight estimation by acquiring multiple ACS in different regions of k-space.

GRAPPA<sup>45</sup> is an improvement over SMASH in that instead of attempting to simulate combine coil data,  $D_c(k + \Delta k)$ , it attempts to simulate missing  $k$ -space in each coil individually, or  $D_j(k + \Delta k)$ . Simulation for each coil, separately, will require a different set of coil weights, which is determined from the ACS acquired from each individual coil. Compared to SENSE, GRAPPA tend to be more robust against local inaccuracies in coil sensitivity maps<sup>46</sup>. A particular relevant examples is the lung, where low signal and tissue inhomogeneity<sup>46</sup> makes it difficult to make an accurate measurement of the sensitivity maps<sup>46</sup>.

### 2.8.2 Compressed Sensing

Image compression methods, such as the JPEG, are widely used for efficient storage of image data. In JPEG compression, the image can be stored with a fraction of the data needed while maintaining an arbitrarily high degree of fidelity. In JPEG compression, a discrete cosine transform (DCT) or Wavelet transform is performed on the image. In this transformed domain, the DCT data is represented with relatively few pixels with high values while many pixels with very low values close to zero are discarded. This property is known as *sparsity*. JPEG compression takes advantage of this property by throwing away many of these low value pixels, while the remaining high DCT value are stored and subsequently re-transformed to recover the image domain data.

Recently there has been great interest in the MRI community to take advantage this data compressibility during data acquisition in a method called Compressed Sensing (CS)<sup>47</sup>. If it is possible to reconstruct a high fidelity image by simply acquiring the few important data points in the sparse domain, then MR data acquisition speed can be significantly increased. However, it is

immediately obvious that this is not a trivial problem for several reasons: Firstly, even if MR images are known to have sparse representation, there is no way to know, *a priori*, which pixels are the important. Secondly, MRI signal is detected in  $k$ -space, which in itself is not a sparse representation.

### 2.8.2.1 – Compressed Sensing

Compressed Sensing theory<sup>48</sup>, in the context of MRI, states that it is indeed possible to acquire an accurate image reconstruction from a small subset of  $k$ -space data if the following conditions are met:

- 1) The desired MR image has a sparse representation in a known domain;
- 2) Under-sampling of  $k$ -space is performed in such a manner that its resulting aliasing artifact is incoherent (noise like)
- 3) Nonlinear reconstruction that enforces sparsity and data consistency is utilized.

Most clinical MRI images, with the exception of angiography images, are not sparse in the image domain. However, the sparsifying transform used for JPEG compression (DCT, Wavelet) are suitable for MR images.

### 2.8.2.2 - Incoherent Artifacts

As shown in the Figure 2-6, regularly spaced under-sampling of  $k$ -space leads to the foldover artifacts that are dealt with using parallel imaging. However, a random sampling of  $k$ -space

leads to artifact that is noise like as shown in Figure 2-7



Figure 2-11 Left: randomly acquired  $k$ -space points with the center of  $k$ -space acquired with higher frequency. Compared to the under-sampling pattern of Figure 1-3, the artifact from random under-sampling manifests itself as incoherent noise.

### 2.8.2.3 – Sampling Strategies

One way to quantify the incoherence of artifacts generated by a particular  $k$ -space under-sampling pattern is to study its point spread function<sup>47</sup>. PSF analysis (Figure 3-3) starts with an impulse function in the image domain and transforms the impulse into  $k$ -space. Under-sampling is performed, and the image is transformed back into the image domain. Coherent artifacts appear as large side peaks along with the original peak, while incoherent artifacts are essentially spread out. For CS to be effective, the maximum height of these secondary peaks must be kept as small as possible.

Another factor to consider in choosing an under-sampling scheme is that the center of  $k$ -space contains most of the energy of the image. Empirically, it has been shown that often CS performs best with a variable density random under-sampling with a high probability in the central  $k$ -space and decreasing probability in the periphery, as shown in Figure 2-12.

In most instances, under-sampling is only performed along the phase encoding direction. Therefore, in a 2D images, random under-sampling can only be performed in the phase encode direction, which is less effective in terms of spreading the side lobes (Figure 3-3, center), In 3D acquisitions, however, phase encoding is used in both the z and the y directions - which allows for a sampling pattern similar to that shown in Figure 2-12.

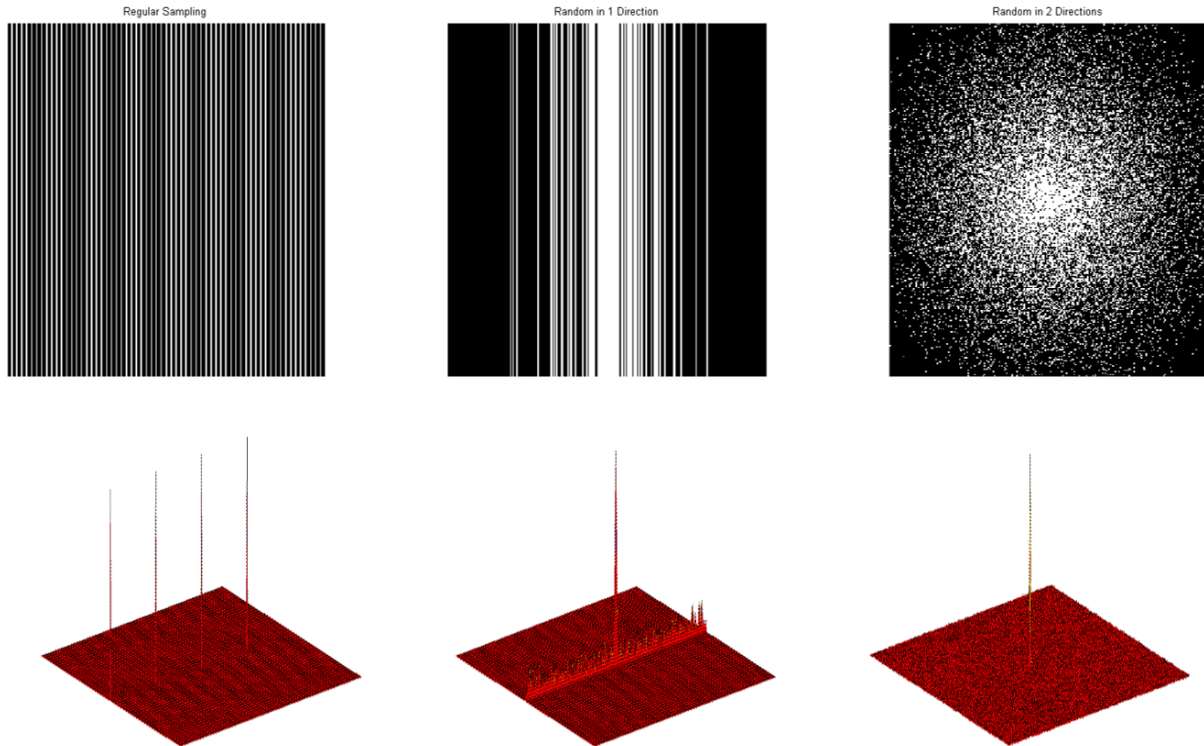


Figure 2-12 - Top Row: from left to right, k-space sampling pattern of 4x regular under-sampling, 4x random under-sampling in 1D and 4x random under-sampling in 2D. Bottom row: corresponding PSF analysis (k-space) for each pattern. Regular under-sampling 4 foldover points with similar intensity to the main peak. In 1D random under-sampling, those peaks are evenly spread along one axis, whereas in 2D random, it is further spread out along both axes. CS performs best when the interference peaks are low.

### 2.8.2.3 - Regularized Reconstruction

Before the discussion of CS reconstruction, it is important to review the mathematical concepts of  $L_p$  norm, which is defined as follows.

$$\|x\|_p = (|x_1|^p + |x_2|^p + \dots + |x_n|^p)^{\frac{1}{p}} \quad (2.96)$$

When  $p = 0$ , the  $L_0$  norm simply sums the number of non-zero elements of the system. In the case where  $p = 1$ , the  $L_1$  norm is simply the sum of all the elements in the image, whereas the  $L_2$  norm, is the root sum of squares of the system

The CS reconstruction attempts to iteratively solve the following inverse convex optimization problem<sup>47</sup>.

$$\mathit{arg\ min}_{\tilde{\rho}} \left( \|\mathcal{F}\{\tilde{\rho}\}|_{k_s} - \mathbf{D}(k_s)\|_2^2 + \lambda \|\Psi\tilde{\rho}\|_1 \right) \quad (2.97)$$

where  $\Psi$  is the sparsifying transform, such as the total variations<sup>47</sup>, wavelet<sup>47</sup>, DCT<sup>47</sup>, Shearlet<sup>49</sup>, and Coutourlet<sup>50</sup>,  $\tilde{\rho}$  is the solution (in the imaging domain),  $\mathbf{D}$  is the measured data,  $\mathcal{F}\{\ \}|_{k_s}$  is the Fourier transform operator, followed by the application of a mask that keeps the sampled locations  $k_s$  values only, and  $\lambda$  represents arbitrary weighting factor between the two terms. The first term in the penalty function is an L<sub>2</sub> norm whose minimization promotes data consistency. On the other hand, minimization of the L<sub>1</sub> term, also known as the regularization term  $\|\Psi\tilde{\rho}\|_1$ , promotes sparsity in the domain of  $\Psi\tilde{\rho}$ . It should be noted that the L<sub>0</sub> norm, which is the number of non-zero elements, is essentially the definition of sparsity. It is therefore more intuitive to promote sparsity by minimizing L<sub>0</sub> norm. However, L<sub>0</sub> minimization problems tend to be very computationally intensive as its constrained cost function is non-convex in expected solution space. L<sub>2</sub> minimization, on the other hand, is guaranteed to be convex and easily solved. However, this process does not promote sparsity very well as it penalizes the high valued pixels rather than driving low valued pixels to zero. L<sub>1</sub> norm on the other hand has been demonstrated to be a reasonably good approximation of L<sub>0</sub>.

The weighting factor,  $\lambda$  determines the relative importance of the two penalty terms. One method of determining the best  $\lambda$  value is by the construction of an L-curve, an example of which is shown in Figure 2-13<sup>51</sup>. A series of reconstructions are performed using different  $\lambda$  values. For each reconstruction, the values of sparsity and consistency penalty terms are plotted against each other. The optimal solution is the one for which both these penalty terms are small - which occurs at the lower left corner of the curve. To demonstrate the effect of different  $\lambda$ , the

4x under-sampled (in 2D) image shown in Figure 3-2 is reconstructed with 3 different weights and shown in Figure 2-14.

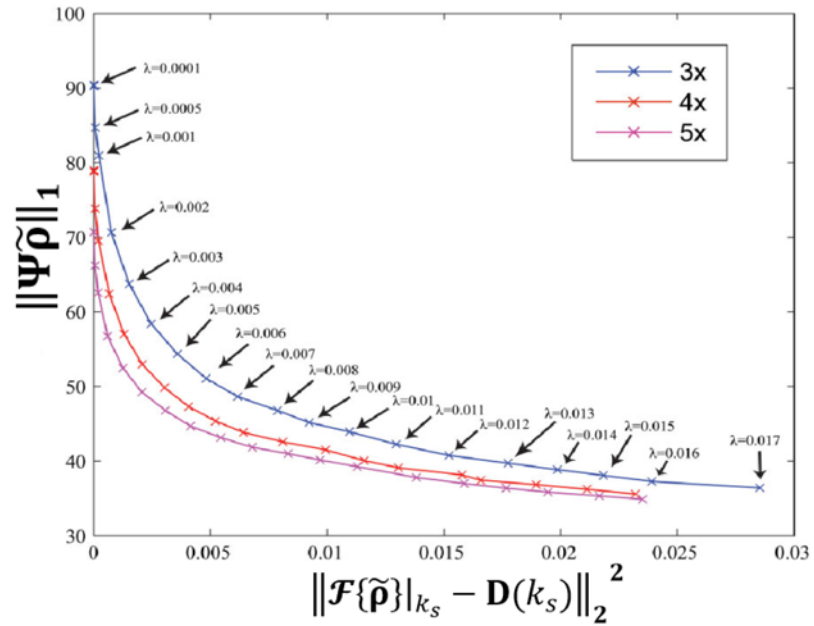


Figure 2-13 - A demonstration of the L-curve method, adapted from by Kim et al.<sup>51</sup>



Figure 2-14 - From left to right: CS reconstructed image from figure 3-1 using optimal CS weight (lower left corner of L-curve), very low weight (upper left corner of L curve) and very high weight (lower right corner of L-curve).

Regularization is the introduction of *a priori* knowledge (i.e. the image has a known sparse representation  $\Psi$ ) to solve the under-determined problem  $\mathit{arg\,min}_{\tilde{\mathbf{p}}} \left( \|\mathcal{F}\{\tilde{\mathbf{p}}\}|_{k_s} - \mathbf{D}(k_s)\|_2^2 \right)$ .

Other types of *a priori* knowledge can also be used. In some special cases, such as MR

angiography images, the image is already sparse in the image domain. One can solve equation 2.97 with the unity operator  $\Psi = \mathbf{1}$  and still yield a good solution. In other situations, if it is known that the image is mostly smooth, one can also apply the more time efficient, 2D finite difference operator as the sparsifying transform  $\Psi$ . Minimization of finite difference for improving image reconstruction has been used outside the context of compressed sensing, in a well-known method known as Total Variations (TV) de-noising.

### 2.8.3 Split Bregman Solver for Compressed Sensing

Unfortunately, the mix of  $L_1$  and  $L_2$  norms in equation 2.97 makes it a relatively difficult problem to solve. This section briefly introduces a very popular solver of the compress sensing optimization. As an example to demonstrate this technique, we attempt to solve equation 2.97, with anisotropic total variations as the regularizer, i.e.  $\arg \min_{\tilde{\rho}} \left( \mu \|\mathcal{F}\{\tilde{\rho}\}|_{k_s} - \mathbf{D}(k_s)\|_2^2 + \|\nabla \tilde{\rho}_x\|_1 + \|\nabla \tilde{\rho}_y\|_1 \right)$ , with the  $L_1$  and  $L_2$  norms coupled together. Using a method proposed by Goldstein *et al*<sup>52</sup>, we solve an reformulation of the same problem, replacing  $\nabla \tilde{\rho}_x, \nabla \tilde{\rho}_y$  with  $\mathbf{d}_x, \mathbf{d}_y$ , while constraining for  $\mathbf{d}_x \rightarrow \nabla_x \tilde{\rho}$  and  $\mathbf{d}_y \rightarrow \nabla_y \tilde{\rho}$ .

$$\begin{aligned} \arg \min_{\tilde{\rho}, \mathbf{d}_x, \mathbf{d}_y} & \left( \mu \|\mathcal{F}\{\tilde{\rho}\}|_{k_s} - \mathbf{D}(k_s)\|_2^2 + \|\mathbf{d}_x\|_1 + \|\mathbf{d}_y\|_1 \right. \\ & \left. + \lambda \|\mathbf{d}_x - \nabla_x \tilde{\rho}\|_2^2 + \lambda \|\mathbf{d}_y - \nabla_y \tilde{\rho}\|_2^2 \right) \end{aligned} \quad (2.98)$$

Goldstein *et al*, then proposed to apply the Split Bregman formulation<sup>52</sup> to solve the above problem. This method splits the problem into smaller iteratively steps which are much more easily solved individually. For the above problem, the 5 steps are as follows.

$$\mathbf{SB1}: \tilde{\rho}^{k+1} = \arg \min_{\tilde{\rho}} \left( \mu \|\mathcal{F}\{\tilde{\rho}\}|_{k_s} - \mathbf{D}(k_s)\|_2^2 + \lambda \|\mathbf{d}_x - \nabla_x \tilde{\rho} - \mathbf{b}_x^k\|_2^2 + \lambda \|\mathbf{d}_y - \nabla_y \tilde{\rho} - \mathbf{b}_y^k\|_2^2 \right)$$

$$\mathbf{SB2}: \mathbf{d}_x^{k+1} = \arg \min_{\mathbf{d}_x} \left( \|\mathbf{d}_x\|_1 - \lambda_1 \|\mathbf{d}_x - \nabla_x \tilde{\rho}^{k+1} - \mathbf{b}_x^k\|_2^2 \right)$$

$$\mathbf{SB3}: \mathbf{d}_y^{k+1} = \arg \min_{\mathbf{d}_y} \left( \|\mathbf{d}_y\|_1 - \lambda_1 \|\mathbf{d}_y - \nabla_y \tilde{\rho}^{k+1} - \mathbf{b}_y^k\|_2^2 \right)$$

$$\mathbf{SB4}: \mathbf{b}_x^{k+1} = \mathbf{b}_x^k + (\nabla_x \tilde{\boldsymbol{\rho}}^{k+1} - \mathbf{d}_x^{k+1})$$

$$\mathbf{SB5}: \mathbf{b}_y^{k+1} = \mathbf{b}_y^k + (\nabla_y \tilde{\boldsymbol{\rho}}^{k+1} - \mathbf{d}_y^{k+1})$$

It should be noted that **SB1** has all L<sub>2</sub> norms, it is therefore convex and can be solved by differentiation. On the other hand, **SB2** and **SB3**, while non-convex, are in a simpler form which can be solved, explicitly, using the Shrinkage method<sup>52</sup>. For SB2, that is

$$\mathbf{d}_x^{k+1} = \max\left(s^k - \frac{\mathbf{1}}{\lambda_1}, \mathbf{0}\right) \frac{\nabla_x \tilde{\boldsymbol{\rho}}^k - \mathbf{b}_x^k}{s^k} \quad (2.99)$$

and for SB3, that is

$$\mathbf{d}_y^{k+1} = \max\left(s^k - \frac{\mathbf{1}}{\lambda_1}, \mathbf{0}\right) \frac{\nabla_y \tilde{\boldsymbol{\rho}}^k - \mathbf{b}_y^k}{s^k} \quad (2.100)$$

where

$$s^k = \sqrt{|\nabla_x \tilde{\boldsymbol{\rho}}^k + \mathbf{b}_x^k|^2 + |\nabla_y \tilde{\boldsymbol{\rho}}^k + \mathbf{b}_y^k|^2} \quad (2.101)$$

Finally, **SB4** and **SB5** can also be explicitly evaluated. By running these 5 steps iteratively, Goldstein *et al* has found the solution converges much quickly compared to alternative methods, such as the standard gradient descent.

## 2.9 Dynamic MR Acceleration

Dynamic MRI is the acquisition of a series of images at the same spatial location at different time points. It has a wide range of applications for studying body function, including the quantification of contrast agent uptake, blood flow, cardiac and breathing functions, as well as organ motions, etc<sup>53</sup>. It is also a valuable tool for various types of interventional MRI, providing

real time guidance for various types of medical treatments ranging from image guided surgery to radiation therapy.

Several methods described in the previous chapter are similar in that they exploit the spatial redundancy of  $k$ -space. Dynamic MRI additionally exploits the redundancy in the temporal domain. Acceleration methods for dynamic MRI can broadly be separated into 3 categories: methods that exploit temporal redundancy only, methods that exploit temporal and spatial redundancy serially, and finally the newest methods that exploit temporal and spatial redundancy jointly.

### **2.9.1 Exploiting Temporal Redundancy: Viewsharing**

The techniques that belong to this category are mostly developed prior to the spatial-redundancy exploiting methods mentioned in the previous sections. They are mostly based on the idea of  $k$ -space sharing (Viewsharing), that is, only a part of  $k$ -space is acquired at each dynamic point, whereas the missing  $k$ -space lines are filled by  $k$ -space points that are acquired previously. The first of such techniques is known as MR fluoroscopy where in each dynamic only a single  $k$ -space line is acquired in a pattern described by Figure 2-15. The apparent frame rate of this type of technique is comparable to fluoroscopy<sup>54</sup>. The most of energy in the image is contained in the central areas of  $k$ -space. Thus, although this technique generates images at a high frame rate, the important part of image is only updated when the central  $k$ -space lines are acquired.

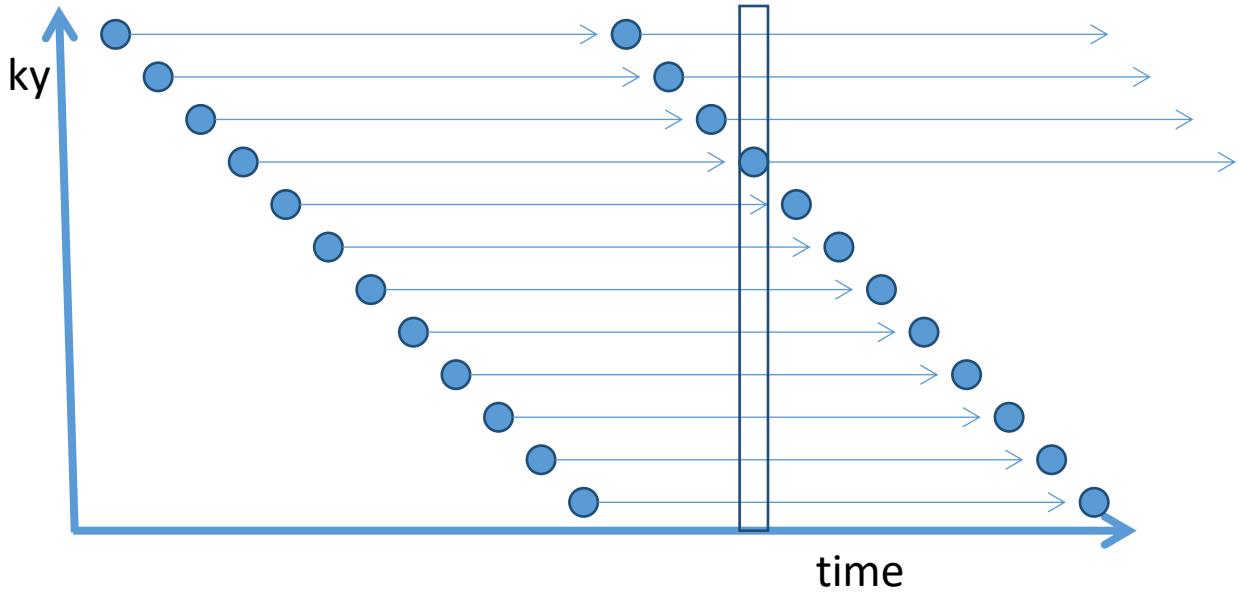


Figure 2-15 –  $k$ -space acquisition scheme of MR fluoroscopy.

Because of the importance of the central area of  $k$ -space, a different method, known as KEYHOLE<sup>55</sup> is developed, which starts with a fully sampled scan followed by under-sampled dynamics, as shown in Figure 2-16.

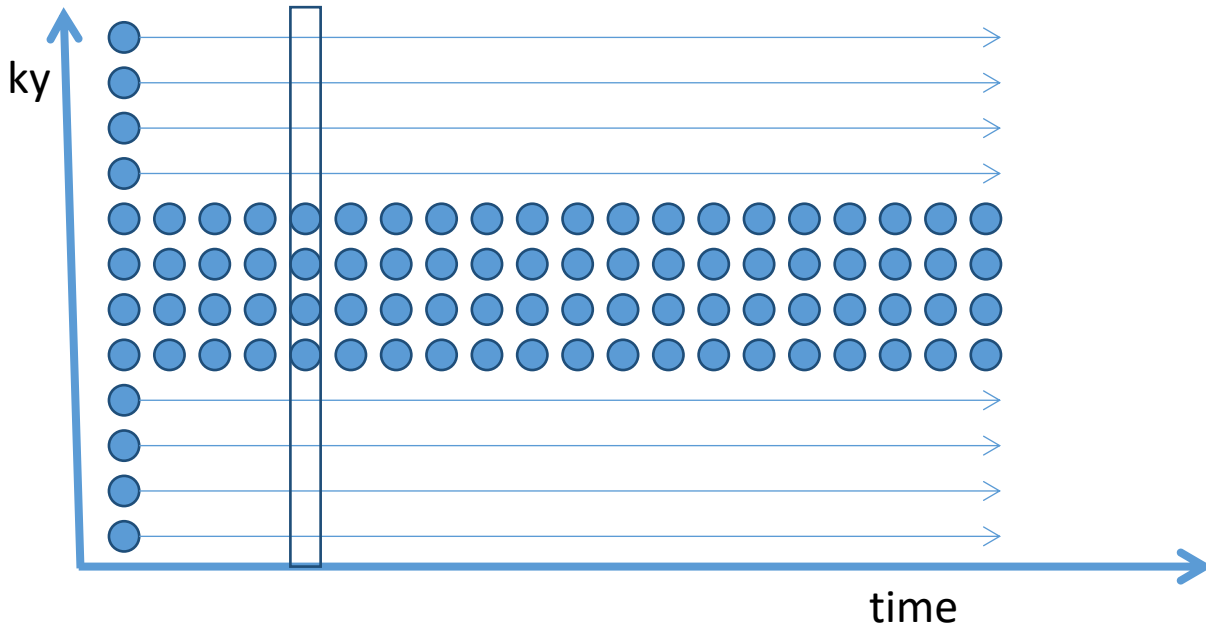


Figure 2-16 -  $k$ -space acquisition scheme of MR fluoroscopy.

KEYHOLE is an effective method in studying dynamic systems where most of the changes between dynamics are contrast changes rather than the positional variation (i.e. the study of contrast uptake). Figure 2.17 shows an example of an artifact that is created when there are motional changes, where the edge of the structure (high resolution) is outdated compared to the location of the contrast (low resolution).

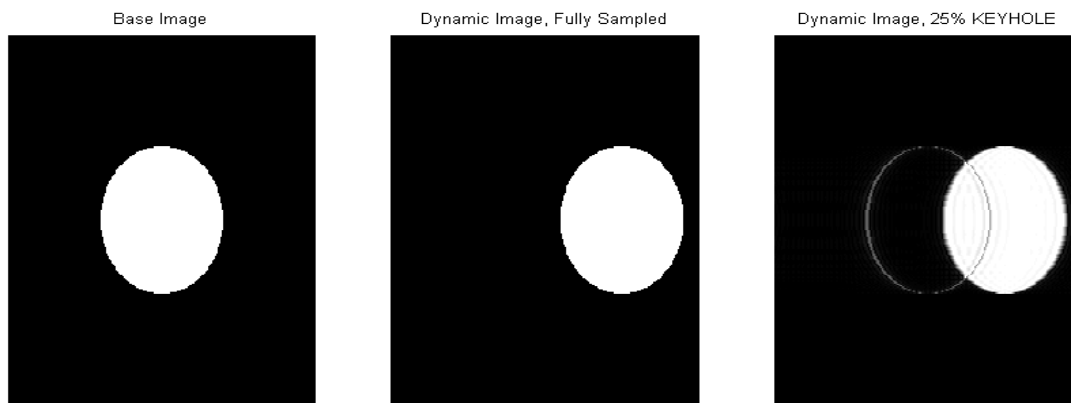


Figure 2-17 – Demonstration of a potential pitfall of KEYHOLE imaging. The left image represents the base image, whereas the middle image represents the fully sampled dynamic image. The right image represents a keyhole dynamic in which the central 25% of  $k$ -space acquired but the remainder of  $k$ -space is shared from the base image. The high frequency component from the base image manifests itself as artifacts.

TRICKS<sup>56</sup> is another approach that allows for less frequent updating of periphery of  $k$ -space. It is based on variable density under-sampling. Note that in this example the central  $k$ -space is updated twice as frequently as the periphery.

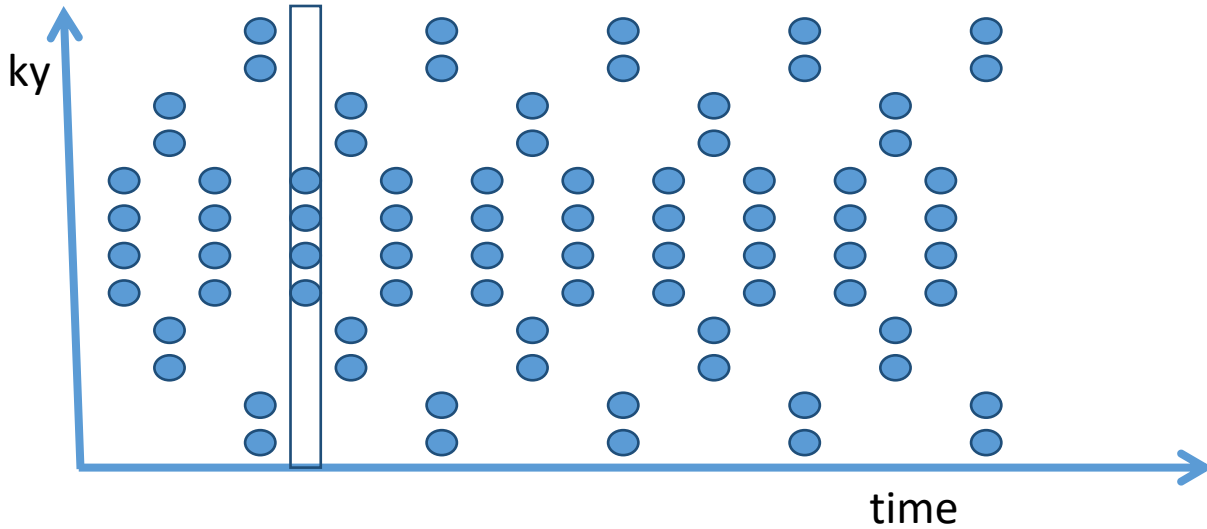


Figure 2-18  $k$ -space acquisition scheme of TRICKS

### 2.9.2 Exploiting Temporal and Spatial Domain Serially

Two examples that exploit temporal and spatial redundancy serially are T-SENSE<sup>57</sup> and T-GRAPPA<sup>58</sup>. In these methods, under-sampling of  $k$ -space is performed in an interleaved manner. A sliding window is used to average these interleaved data into a high spatial resolution but temporally blurred data. This blurred data is used to improve the estimate of coil sensitivity in the case of SENSE, and to improve the accuracy of coil weights in GRAPPA. After this step is performed, standard SENSE and GRAPPA reconstruction is performed on each dynamic image. Figure 2-19 shows an example comparing GRAPPA with T-GRAPPA with an acceleration factor of 3. In the GRAPPA example, the minimum required amounts of ACS are acquired. In T-GRAPPA, the complete set of ACS can be generated acquired using the 2 set of interleaved data prior to it. Note that these ACS points are NOT used during GRAPPA reconstruction, but only for the accurate determination of coil weights.

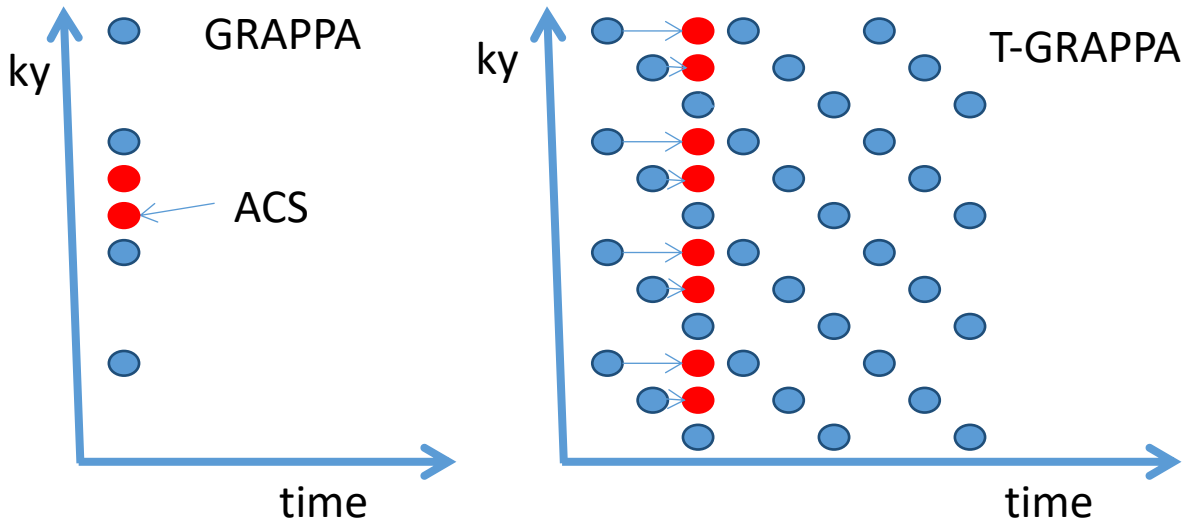


Figure 2-19 – GRAPPA compared to T-GRAPPA. In T-GRAPPA,  $k$ -space points from previous dynamic serves as ACS used to determine coil weight for GRAPPA reconstruction.

### 2.9.3 Exploiting Temporal and Spatial Redundancy Jointly

#### 2.9.3.1 Regular Sampling: UNFOLD, $kT$ -BLAST

This section describes a subset of powerful methods that exploit spatial and temporal redundancy jointly. These methods tend to have the highest ability to under-sample dynamic images.

However, these methods tend not to be suitable for on-the-fly imaging needed for real time tumour tracking, as it typically requires the entire dataset to be acquired prior to reconstruction, and relatively long reconstruction times.

In section 2.8.1, it was discussed that the under-sampled  $k$ -space generates predictable artifacts in image space related through the 2D Fourier transform. However, in the context of dynamic under-sampling, the under-sampling occurs in  $k$ - $t$  space, the analogues 2D Fourier of  $k$ - $t$  space is commonly called the  $x$ - $f$  space. A set of dynamic images has three coordinates  $(x_1, x_2, t)$  with the corresponding  $k$ -space coordinates  $(k_{x1}, k_{x2}, t)$ . In order to generate a series of  $xf$ -planes, we first perform a 1D Fourier transform along the frequency encoding direction  $x_1$ , resulting in  $(x_1, k_{x2}, t)$ . In this representation, there is a  $k$ - $t$  plane along every point in  $x_1$ .

The appearance of an  $x_2$ - $f$  plane is a “cross” shape as shown in Figure 2-20. The central region along the  $x_2$  dimension tends to contain more signals since the FOV is located such that the organs of interest are located in the center of the FOV. However, along the  $f$ -axis, the signal

concentrated near the origin represents the static or slow time varying signals – which in most cases represent the majority of energy in the image.

Now let’s consider an interleaved, alternating regular under-sampling. Recall from the Figure 1-3 that regular under-sampling in k-space leads to foldover artifacts in the image domain. The analogous effect occurs here, except that the under-sampling occurs in a 45 degree rotated axis, which leads to rotated foldover artifacts in the x-f domain (Figure 2-20, left), because the “corners” of x-f space contains relatively little signal, the foldover artifact tend not to contaminate the central region. In the UNFOLD<sup>59</sup> method, the operator defined “cross” shape region (white dotted region in Figure 2-20, left), in which all the signal outside the region is simply removed. This has the effect of filling in the missing k-space points. Note that method does not fully preserve all the missing information, as the regions outside the cross in x-f space, namely the fast changing information in the periphery of the image is sacrificed. Increasing the under-sampling means the aliasing in x-f space is closer to the central region, which means the “cross” region must be reduced, sacrificing more dynamic information.

k-T BLAST<sup>60</sup> eliminates the need for an operator to define the appropriate “cross” region by acquiring low resolution training data (Figure 2-20, right). This low resolution training data is used to generate a “blurred” x-f image which is then used to guide image reconstruction.

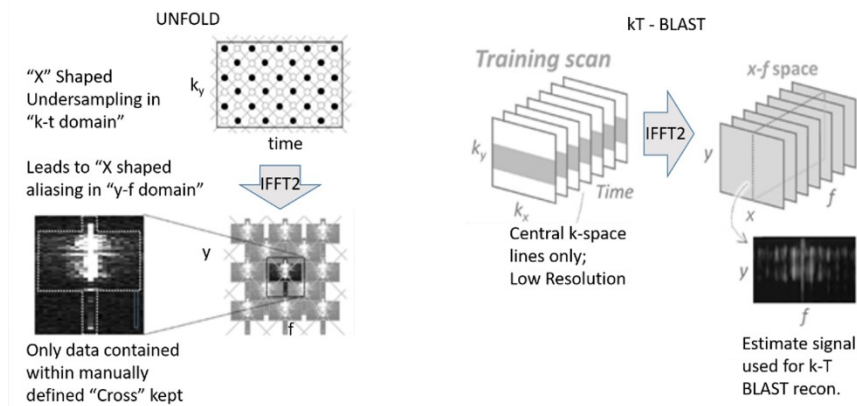


Figure 2-20 – Left the UNFOLD technique, Right: k-T BLAST technique, adapted from Tsao<sup>53</sup>.

### 2.9.3.2 Irregular Undersampling: kT-SPARSE, kT-SLR

The principle of CS MRI can also be applied in dynamic imaging, in the form of k-T SPARSE<sup>61</sup>. From the UNFOLD example, a regular under-sampling of k-T space leads to foldover artifacts in

x-f space. Recall the first condition required for Compressed Sensing is that sampling must be done in a random manner that leads to incoherent artifacts, and the second condition required for CS MRI is to find a sparse representation of the image data. In the x-f space, the data is sparse along the f-dimension but not sparse in the spatial (x) dimension. The solution is therefore to perform a Wavelet transform along the spatial dimensions, resulting in the sparse w-f space. After which, the familiar convex optimization can be used to perform reconstruction

$$\mathit{arg\ min}_{\tilde{\mathbf{p}}} \left( \left\| \mathcal{F}_{x,y}\{\tilde{\mathbf{p}}(x, y, t)\}|_{k_s} - \mathbf{D}(k_s) \right\|_2^2 + \lambda \left\| \Psi_{x,y} \mathcal{F}_t\{\tilde{\mathbf{p}}(x, y, t)\} \right\|_1 \right)$$

It is important to accurately keep track of the domain in which these variables operate. We desire our solution  $\tilde{\mathbf{p}}$  please change, to be a set of dynamic MRI images, therefore  $\tilde{\mathbf{p}}$  is in the x-t domain. However, our acquired data,  $\mathbf{D}$ , is in the k-t domain. Therefore the Fourier transform term  $F_u$  only operates on the spatial domain. In the  $L_1$  term, the sparsifying transform  $\Psi$  is a 1D wavelet that only operates in the spatial domain of  $\tilde{\mathbf{p}}$ . While the k-T SPARSE method is conceptually the easiest to understand, other more advanced k-T CS methods have been developed. One example is k-T FOCUS<sup>62</sup>, which decomposes the total signal into predicted and residual components. The prediction component can be obtained from viewshare images of the dynamic data. The reconstruction then exploits the sparse representation of the remaining residual signal. . Another example of an advanced spatial temporal CS method is the k-T SLR method<sup>63</sup>. In k-T SLR the Karhunen Louve transform is used, which decomposes the k-t data to a series of orthogonal basis functions. In this approach, rather than enforcing sparsity in a particular domain, the method applies a spectral penalty to estimate temporal basis function and its weights, fully exploiting the correlations within a temporal data set. XD-GRASP<sup>64</sup> is a radial based spatial temporal strategy which is particularly effective if there are multiple sources of motion present at different temporal frequencies (i.e. respiratory and cardiac). These different motions types are separated into their individual motion state dimensions and sparsity is exploited in these dimensions. Generally, these methods are retrospective in nature, requiring the complete dataset, in temporal sense, to be acquired before the image construction can start. They also tend to be much more computationally intensive than the standard compressed sensing, as the optimization solver must be applied to a larger matrix (i.e. 3D for dynamic 2D images, 4-D for dynamic 3D images).

## 2.10 Summary

To summarize, there are many strategies which one can use to accelerate MR acquisition. However, they are not all suitable for the purpose of real time imaging. The non-dynamic strategies that rely on spatial redundancy only (Compressed Sensing, Parallel Imaging) can potentially be used in real time, with CS having the advantage of not being reliant on specialized phase-array coils not available in some situations. For dynamic imaging, view sharing strategies that rely on temporal redundancies only (i.e. Keyhole, TRICKS) are suitable for real time use, whereas the more powerful spatial-temporal strategies tend to be more suitable for retrospective reconstruction due to the requirement of significantly longer reconstruction times. In chapters 4 and 5, a novel strategy that is presented, improving upon the CS strategy by incorporating prior data (i.e. taking advantage of temporal redundancy in addition to CS), while maintaining near real time image reconstruction times.

## **Chapter 3 Validation of a tumour autocontouring algorithm**

*Parts of this chapter have been adapted from a published article: Yun J, Yip E, Gabos Z, Wachowicz K, Rathee S, Fallone BG. Neural-network based autocontouring algorithm for intrafractional lung-tumor tracking using linac-MR. Medical Physics. 2015;42(5):2296-2310.*

### **3.1 Introduction**

One of the most exciting applications of hybrid Linac-MR system<sup>20</sup> is real time tumour tracking (RTTT), which takes advantage of the simultaneous MR imaging and radiation delivery. In the RTTT scheme currently being developed at the Cross Cancer Institute, the moving tumour is imaged with the dynamic MRI in real time, and the tumour is segmented in real time using an in-house autocontouring algorithm<sup>65</sup>. This chapter describes this in-house method and its latest developments, as well as the experiments designed to validate our auto-contouring algorithm using both phantom images, where the tumour shape and location is known *a priori*, as well as in patients, in which the auto-contouring algorithm is compared against the manual contours by a radiation oncologist – the current gold standard for contouring tumours in MR images. Once validated, the tumour autocontouring algorithm is a valuable tool in evaluating MR acceleration strategies, as all MR acceleration strategies inevitably result in some reconstruction errors compared to a fully sampled, albeit slow, image. By applying a validated autocontouring algorithm to the undersampled images and analyzing the changes in contours, allows us to compute a series of metrics which can be used to assess image reconstruction quality. This chapter describes a study designed to validate the current tumour auto-contouring software at the CCI.

#### **3.1.1 Artificial Neural Network Based Tumour Tracking Algorithm**

As the emphasis of this chapter is on the validation, rather than the development of the algorithm, and details of the algorithm will only be summarized here. For the detailed description of the inner workings of the algorithm, please refer to the appendix of the manuscript<sup>30</sup>. Compared to the previous version<sup>65</sup>, the latest autocontouring software uses artificial neural networks, which is briefly discussed here. Artificial neural network is a mathematical model to emulate the electrochemical mechanism of a cat's visual cortex. In this model, a nerve comprises of a matrix of individual neurons. Each individual neuron receives continuous signals as inputs, but it can only have a binary output (firing / not firing). These

neurons are also interlinked with each other such that a neuron's output is dependent not only on its own input, but on the inputs of neurons in close proximity, thus, neurons tend to fire together as a cluster. In our MR images, a tumour consists of heterogeneous cluster of hyper-intense pixels in comparison to surrounding healthy tissue(s). Each pixel in the image can emulate as a neuron; the actual pixel's value being the input of neuron. The neural network model hence serves as a way to group together heterogeneous tumour pixels to give a uniform output value based on a uniform criteria for firing. Applying this algorithm iteratively enhances the contrast of the tumour compared to the surrounding healthy tissue(s)

The current clinical standard for segmenting tumour in an image is the manually drawn contour by the radiation oncologist. The algorithm is designed to mimic the performance of a human clinician, and described in the following steps.

### 3.1.2 Preparatory Steps and User Input.

As a preparatory step, the user acquires a set (approximately 30) of fully sampled dynamic images prior to the real time dynamic series. The user (a clinician) then contours the tumour in all 30 images, which will be referred to as  $ROI_{STD}$  (Fig 3.1, a); the shape of these  $ROI_{STD}$  is used for training the algorithm. From these 30  $ROI_{STD}$ , a single representative region, least impacted by the breathing motion at the end of the exhale phase, is chosen as a representative tumour,  $ROI_{REP}$ . Next, from observing tumour trajectory of motion in 30 images, the user determines a larger "background region" (Fig 3.1, c) that encompasses the motion trajectory of the tumour.

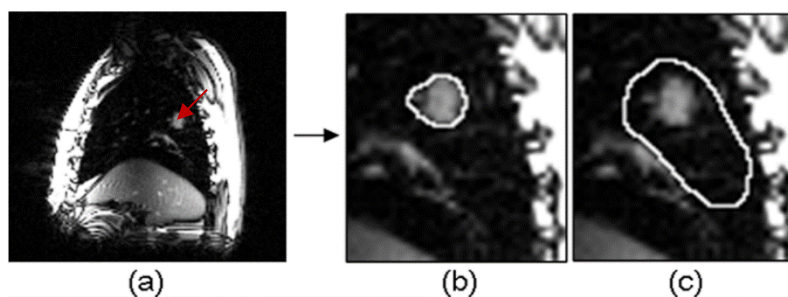


Figure 3-1 – (a) A dynamic MR image containing the tumour (red arrow), which is zoomed in, and displayed with the manually defined (b)  $ROI_{STD}$  (c) background.

### 3.1.3 Parameter Optimization

The manually defined contours are used to optimize neural network parameters that governs the iterative process (i.e. degree of contribution from neighboring pixels, firing thresholds, etc.)

which is used to enhance tumour contrast (Figure 3-2, b) as well as 2 morphological parameters (dilation/erosion) that is applied after thresholding (Figure 3-2, e-f).

These contours are also used to train the neural network algorithm by optimizing the similarity between the manual standard and automatically determined contours. To find the optimal parameters, the main algorithm, described in the next section is performed, and the results  $ROI_{auto}$  compared to the 30  $ROI_{STD}$ . The optimal set of parameters yield the contours that are best matched to the standard manual contours in terms Dice Coefficient (DC), define as:

$$DC = 2 \frac{Area(ROI_{STD} \cap ROI_{Auto})}{Area(ROI_{STD}) + Area(ROI_{Auto})} \quad (3.1)$$

### 3.1.4 Main Processes

Once all the parameters have been determined, the image segment of each newly acquired dynamic image contained within the background region is extracted using a masking procedure. The main processes of the neural network consists of the following steps: 1.) Normalized cross correlation is performed between the extracted background region of the new image against  $ROI_{REP}$  2) From the region centered at this new location, a smaller region, defined by a dilated version of  $ROI_{REP}$  is further extracted, yielding the image in Fig 3-2(a); 3) A neural network algorithm is then applied iteratively, with the optimized parameters to enhance the tumour contrast, yielding the image in Fig. 3-2(b); 4) This image is then thresholded via the Otsu's Method<sup>66</sup> to give the image in Fig. 3-2(c); 5) Small islands in this image are then removed to give the image in Fig. 3-2(d); 6) The tumour shape is then smoothed, yielding the image in Fig.3-2(e); and 7). Dilation and erosion steps are finally applied to provide the final contour as shown in Fig. 3-2(f).

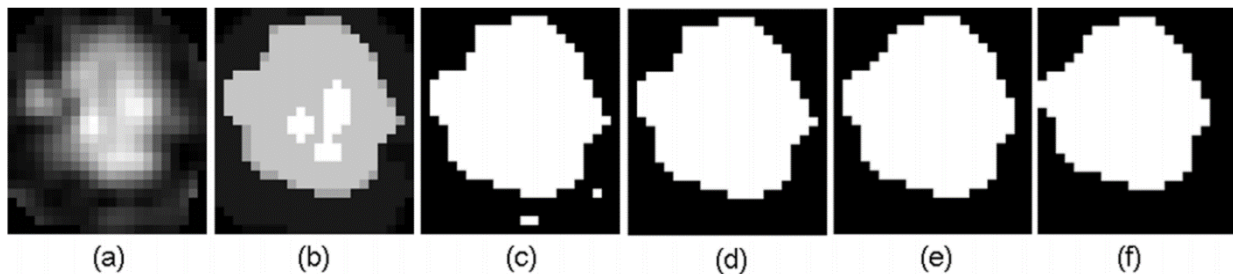


Figure 3-2: The multi-step process in which the tumour shape is determined from the image: (a) The expanded  $ROI_{STD}$  from which the algorithm determines the tumour region. (b) The neural network contrast enhancement. (c) Thresholding by Otsu's method. (d) Removal of small discontinuous islands, e) smoothing and f) Dilation/Erosion.

## **3.2 Validation Study – Methods**

The goal of this study is to validate the neural network based autocontouring algorithm that automatically segments lung tumours in the dynamic images of both the phantom and patients. During the course of this dissertation, only the 3T clinical Philips Acheiva MRI system (Philips Medical Systems, The Netherlands) was capable of performing the real time (i.e. dynamic images at 4 frames per sec e.g.) imaging. Furthermore, the ethical approval from the hospital's ethical board was only feasible and obtained for the patients that were imaged using this system. On the other hand, the Linac-MR system operates at a lower field strength of 0.5T, with the real time imaging (and potentially tumour tracking) capability to be available in the very near future. Thus, we designed a series of phantom and patient studies on the available clinical 3T system. In the post-processing step of the images obtained using this 3T system, we generated pseudo 0.5 T noise-equivalent dynamic images of both the patients and the phantom to validate the auto-contouring software's ability to accurately contour the tumour in images equivalent to those obtained with our the Linac-MR system.

### **3.2.1 Phantom Experiment Setup**

Our phantom and its experimental setup are shown in Figure 3-3. The phantom is placed inside the MRI's field of view, and it contains a moving "lung compartment" that can freely slide within the "thorax" region. The thorax region contains the standard phantom solution<sup>67</sup> of sodium chloride (3.6 g/L) and copper sulfate (1.25 g/L) to mimic a realistic electric load to the coil. In the lung compartment, the lung "tumour model" (red circle in Fig. 3-3) is located approximately at the center of the lung compartment, and the tumour model is surrounded by simulated lung tissue (green rectangle).

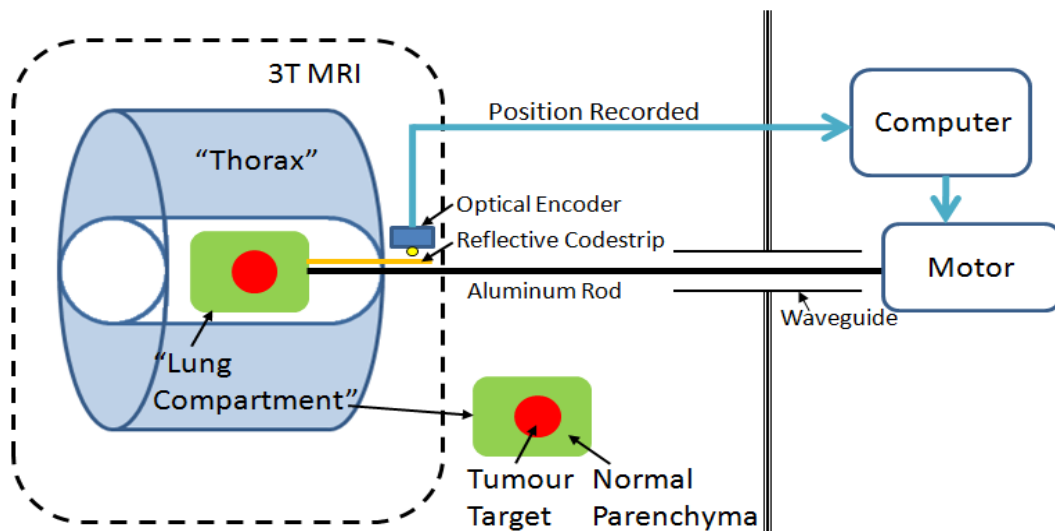


Figure 3-3: A schematic diagram describing the motion phantom.

The lung phantom was designed<sup>65</sup> to mimic the lung tumour and the normal lung parenchyma contrast characteristics in the 0.5T Linac-MR system in the 3T clinical system available (see Table 3-1). The lung tumour model consists of a spherical shaped container filled with an aqueous solution of Manganese (II) Chloride ( $\text{MnCl}_2$ , Signa Aldrich), with concentrations by volume of 0.020 g/L, whereas the simulated normal parenchyma is made of mixture of 2mm plastic beads (no MR signal) mixed with porcine gel in a 70:30 volume ratio. The porcine gel contains 0.0125 g/L  $\text{MnCl}_2$ . Finally, 3.6 g/l NaCl is added to all solutions to simulate the electric conductivity of tissues. On the 3T system, the measured  $T_1$ ,  $T_2$  and relative PD values of the simulated lung are shown to be comparable to the literature values of the actual lung at 0.5 T, as shown in Table 3.1.

Table 3-1 – Lung Tumour and Normal Lung Parenchyma Contrast Parameters measured on the 3T scanner compared to literature values at 0.5T as used in the phantom designed to mimic 0.5T MR contrast in a 3T scanner.

	Lung Tumour		Normal Lung Parenchyma	
	Literature	Measured (3T)	Literature	Measured (3T)
	(0.5T)		(0.5T)	
$T_1$ Mean±SD	<hr/>			
(ms)	532±271 <sup>37</sup>	519±2.4	599±114 <sup>37</sup>	604±4.9
$T_2$ Mean±SD				
(ms)	69±45 <sup>37</sup>	61±1.9	79±29 <sup>37</sup>	97±5.9
Relative PD to tumour	N/A	N/A	0.20 - 0.34 <sup>68,69</sup>	0.30

The lung compartment is attached to a programmable motor via a rigid aluminum rod, creating 1-D motion parallel to the aluminum rod and to the longitudinal axis of magnet bore. This motion is in the same direction as the patient’s superior-inferior (SI) direction that is known to be the largest motion of the lung tumour caused by free-breathing. The aluminum rod is grounded to the wave guide using a small amount of copper tape to eliminate any RF noise coupled by the metal rod. To provide an independent, reference measurement of the lung tumour position, an optical encoder (model #: AEDR-8300-1Q2, Avago technologies, San Jose, CA) was attached to the thoracic cage as shown in Figure 4-1. Paired with the encoder, a reflective code strip (resolution: 180 lines per inch) which is attached to the moving compartment that contains the tumour model. Because all other parts of the phantom are stationary, and the tumour model is fixed in the lung compartment, any change in the tumour position in SI direction is measured by the encoder as a change in counts (1 count  $\approx$ 0.035mm). In our experiments, the phantom is

programmed to undergo 4 breathing motion patterns: a basic sine pattern, and 3 realistic breathing patterns based on a Cyberknife™ study<sup>70</sup>, shown in Figure 3-4.

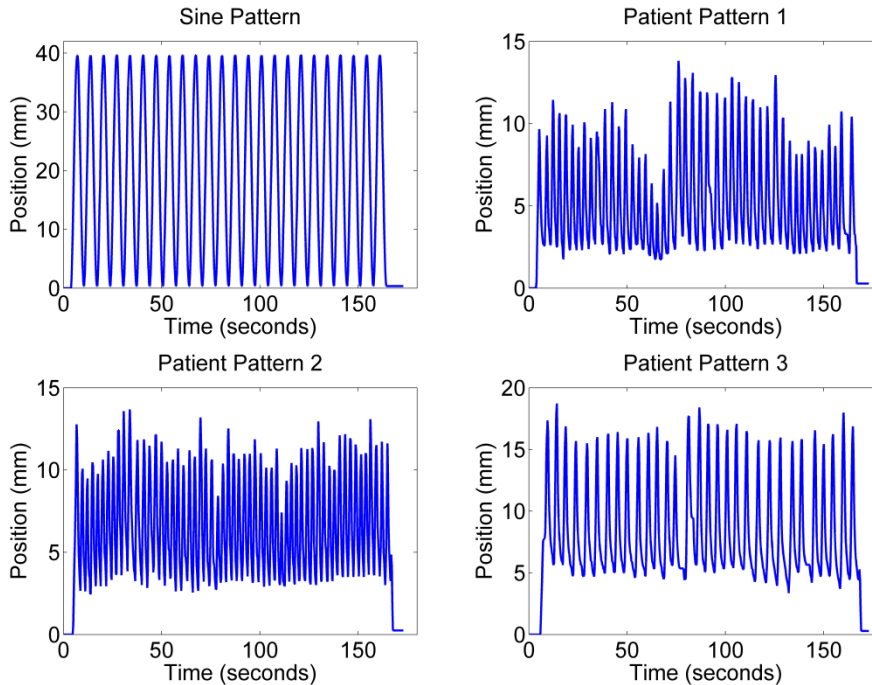


Figure 3-4 – S-I Motion Pattern applied to the phantom. A sine pattern and 3 patient patterns, based on a Cyberknife™ study<sup>70</sup> is used.

### 3.2.2 The MRI Protocol for Phantom Data Acquisition

For the phantom, two scans are performed. A high quality, high resolution TSE scan (MRI Parameters: FOV = 400 mm x 400 mm, voxel size = 0.4 mm x 0.4 mm x 4 mm, 5 slices, TE = 87 ms, TR = 1798 ms) is performed. These images accurately visualize the wall of the tumour to determine the “standard shape” of the tumour. For dynamic imaging, the 2D bSSFP sequence was used to acquire images at approximately 4 fps (Identical FOV to TSE scan: 400 mm x 400 mm, Acquired at 128x128, which translate to 3.1 mm x 3.1 mm x 20 mm, TE = 1.1 ms, TR = 2.2 ms, Dynamic Scan Time = 275 ms) in the horizontal plane through the middle of the tumour model, known as the coronal plane. A total of 600 dynamic images were acquired. Prior to each dynamic image acquisition, an external synchronization pulse at known time point is sent to the optical encoder. Using this pulse, the optical encoder records the position of the tumour at the mid-point time of each dynamic data acquisition when the signal acquisition is occurring at the center of k-space. The first few images in the dynamic scan series are acquired prior to the

commencement of motion, with the phantom in the same position as the reference TSE scan. These images are visually inspected to ensure alignment with the high-resolution TSE image.

All MR images were acquired with a 6 channel Philips torso coil. Noise is measured as the standard deviation for each individual image in a 10x10 pixel region at the corner of the image containing no MR signal. To ensure there is no positive bias to the measured noise, the noise is measured in the real and imaginary images and averaged, rather than being measured in the magnitude images.

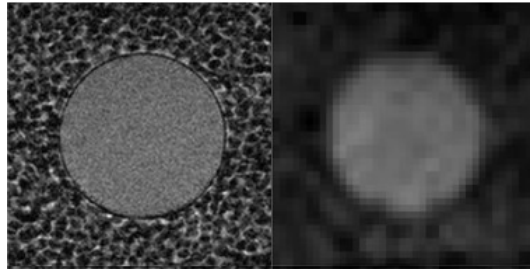


Figure 3-5 – Left : High Resolution (0.4 mm) reference scan allows for visualization of edge of tumour, Right, lower resolution (3.1mm) dynamic scans acquired at 4 fps.

### 3.2.3 Phantom Image Post Processing

Gaussian distributed random values are added, as additional noise, to the images that were acquired on the 3 T MRI system, in order to reflect the lower CNR at 0.5 T. Downscaling of CNR from 3 T images could be achieved by linear CNR scaling, amplifying the measured background noise by a factor of 6 to reduce CNR according to equation 2.69. One additional correction must be added, as the tumour model of aqueous solution (~100% water), whereas actual tissues contain approximately 75% water<sup>71</sup>. Therefore, image noise is further increased by another 33% to account for this difference in absolute proton density. Combining these two corrections, noise amplification factors of ( $N = 8$ ) were applied to simulate the 0.5 T images. Noise amplification is achieved by the addition of uncorrelated noise, in the form of zero mean Gaussian random numbers, to the images. Assuming statistical independence, the required standard deviation of the added noise is derived from the standard deviation of measured noise using the following equations

$$(N \cdot \sigma_{meas})^2 = \sigma_{meas}^2 + \sigma_{added}^2$$

$$\sigma_{added} = \sqrt{N^2 - 1} \cdot \sigma_{meas} \quad (3.2)$$

The adjusted 0.5T SNR/CNR for the tumour is measured and shown in table 3-2. It should be noted that despite accounting for contrast parameters (T1, T2) at lower fields, this simulation of 0.5 T image is still has the following limitations. While considering the SNR at 0.5 T, reduced specific absorption ratio (SAR) allows the larger flip angles, compensating somewhat for the lost SNR due to the lower B<sub>0</sub>-field. In terms of structured artifacts, imaging at 0.5 T is less sensitive to the off-resonance effects, reducing bSSFP banding artifacts present at the 3T images.

Table 3-2 – Measured SNR and CNR of the Phantom Tumour model in the pseudo 0.5 T images.

Motion Pattern	Tumour SNR (Mean ± SD)	CNR (Mean ± SD)
Sin	11.7±0.7	7.5±0.5
Pattern 1	11.7±0.8	7.6±0.5
Pattern 2	12.3±0.8	8.0±0.5
Pattern 3	12.6±0.8	8.2±0.5

### 3.2.4 Patient Study – Data Acquisition

With ethics approval from the Alberta Cancer Research Ethics Committee, we have recruited 6 non-small cell lung cancer patients who are candidates for lung radiotherapy/radiosurgery to undergo dynamic MRI in the clinical 3.0 T MR system, under free breathing for 3 minutes using the same dynamic balanced steady state free precession (bSSFP) sequence as described in the previous section. A total of 650 full sampled images are acquired at a rate of 270 ms/image. Examples of these images are shown in Figure 3-6.

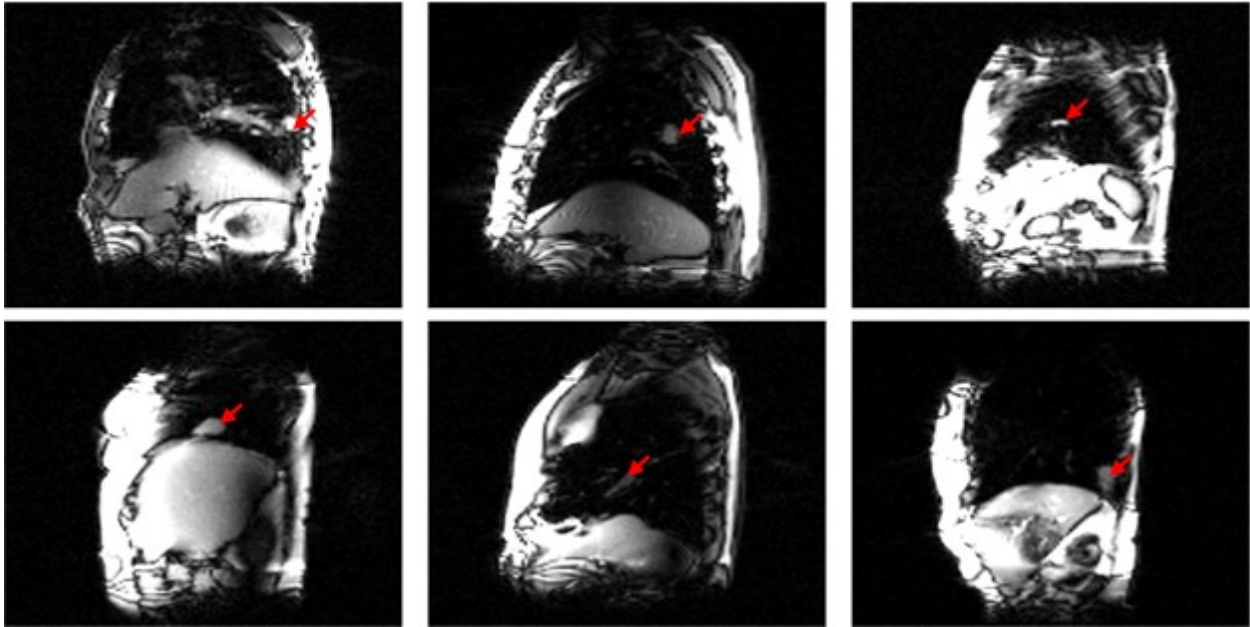


Figure 3-6: Fully sampled images of our 6 patients. Red arrows indicate the location of lung tumour.

### 3.2.5 Patient Data - Image Post Processing

Downscaling of the noise from 3T to 0.5T in the patients' images is performed by linear scaling SNR as described in equation 3.2. Noise is measured in the image, and amplified by a factor of  $N = 6$  according to equations 3.2, leading to the example images of Figure 3-7. After the noise is added, we were unable to detect any meaningful signal from the background parenchyma. (i.e. the detected signal is so low that we cannot make our measurements in the magnitude images, and found that regions have  $\sim$  zero mean in their real and imaginary images), hence have background of SNR of zero. From equation 2.69,  $CNR = SNR$  in this case. The results are given in Table 3-3. Please note that only the pseudo 0.5 T equivalent images are used in this validation study. For the compressed sensing studies presented in chapters 4 and 5, we use both 3T and pseudo 0.5 images.

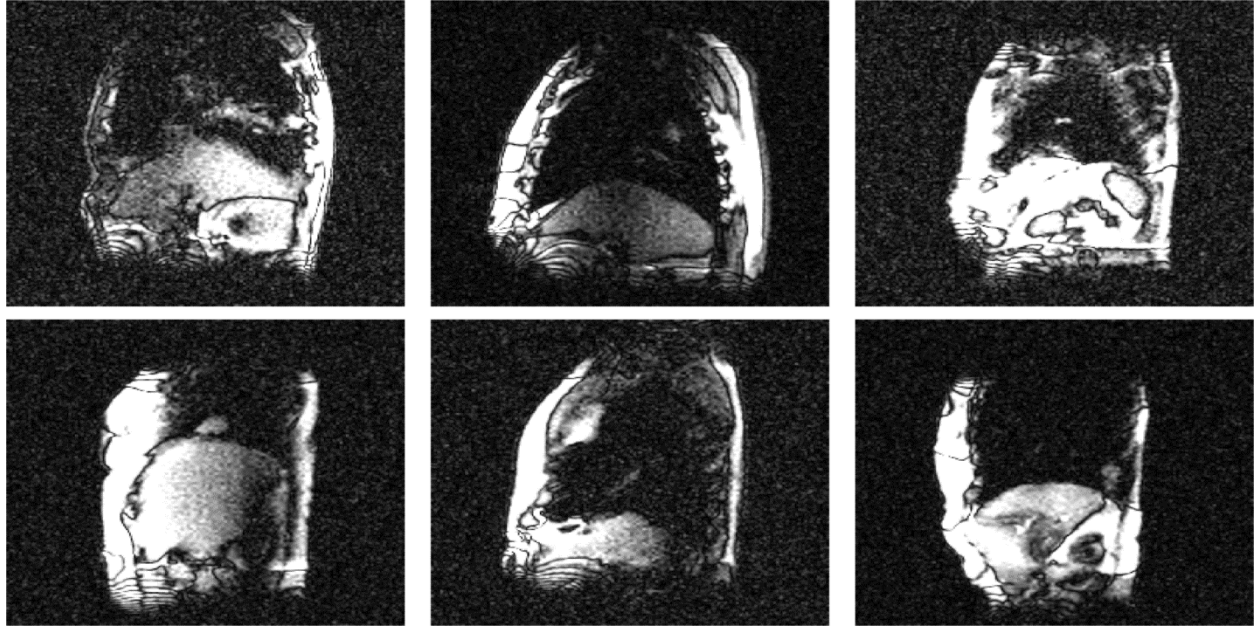


Figure 3-7 – Noise added, pseudo 0.5 T equivalent images of our 6 patients.

Table 3-3 – Measured Tumour SNR, Area, and Maximum extent of motion for the 4 patients.

Patient #	Original 3T SNR/CNR	Pseudo 0.5 T SNR/CNR	Area (cm <sup>2</sup> )	Max. Extent SI Motion (mm)	Max. Extent AP Motion (mm)
	Mean (SD)	Mean (SD)	Mean (SD)		
1	39.7 (1.9)	6.7 (0.5)	4.76 (0.19)	25.7	5.4
2	18.0 (1.0)	3.1 (0.5)	6.81 (0.37)	34.9	9.9
3	24.2 (1.8)	4.2 (0.4)	2.35 (0.31)	20.9	8.7
4	31.5 (1.5)	5.4 (0.4)	6.41 (0.68)	11.0	5.7
5	24.6 (1.0)	4.3 (0.5)	3.10 (0.35)	13.4	9.4
6	26.5 (1.2)	4.6 (0.3)	7.97 (0.29)	12.6	1.9

### 3.2.6 Contour Comparisons

The auto-contouring algorithm generates a contour for every dynamic image acquired and fed into the software. We assessed the accuracy of automatically delineated contours by comparing

to the reference, “gold standard” contours. For the phantom, the standard shape is determined from the high resolution (1024x1024) TSE image which allows the shape to be easily delineated manually in MATLAB as the line between “tumour” and “healthy” (Figure 3-5, left) regions. This “standard shape”, which is a 1024x1024 mask, is translated in the superior and inferior direction at positions determined using the optical encoder readings. This provides a series of high resolution standard contours whose position is determined independently using the optical encoder. The automatic contours, generated at 256x256 resolution, is upscaled to 1024x1024, and compared to this high resolution standard.

For the patient datasets, separate high resolution scans cannot be acquired, therefore, the standard contours around the GTV are delineated on every 3T image manually by a senior radiation oncologist. A subset of 100 out of 650 images is first uploaded into the CERR (Computational Environment for Radiotherapy Research) environment. A standard “MRI” window and level is used, and the radiation oncologist is asked to manually contour the GTV in these 100 images. In this case, both the standard and the auto-contours are at 256x256 resolution. To compare the standard and auto contours, two metrics are used. The first metric is to measure the displacement error  $\Delta d$  between the centroid of the two contours, given as:

$$\Delta d = \sqrt{\Delta x^2 + \Delta y^2} \quad (3.3)$$

The second metric of contour comparison is the Dice’s coefficient, which is the same metric as used for parameter optimization of the algorithm given in Eq. (3.1).

### 3.2.7 Intra-observer and Inter-observer variability experiment

The validation of our auto-contouring algorithm is by comparison to the radiation oncologist’s manual contours as our standard ( $ROI_{STD}$ ), it is important to assess the inherent variability in these contours. We therefore designed a study of intra-observer variability, which is defined as the variation in contours obtained in the same images, by the same radiation oncologist at different times

For our patient datasets, the senior radiation oncologists was asked to re-contour the 100 3T images of every patient on a different day, several months after the initial contouring. The images are re-contoured in CERR using the identical window and leveling (“MR”) setting. These new contours ( $ROI_{INTRA}$ ) are now compared to the original standard contours, ( $ROI_{STD}$ )

which allows us to determine both the intra-observer Dice's coefficient, as well as intra-observer centroid error.

To evaluate the uncertainty of contouring between different oncologists, a second radiation oncologist, blind to the original contours, was asked to contouring the images using the same software with identical images, using the identical computer and window/leveling. These new contours ( $ROI_{INTER}$ ) is compared against the original standards ( $ROI_{STD}$ ), to determine inter-observer Dice coefficient and inter-observer centroid error.

### 3.3 Results

The extent of tumour motion for 6 patients, as determined by the auto-contouring algorithm is shown in Figure 3-8.

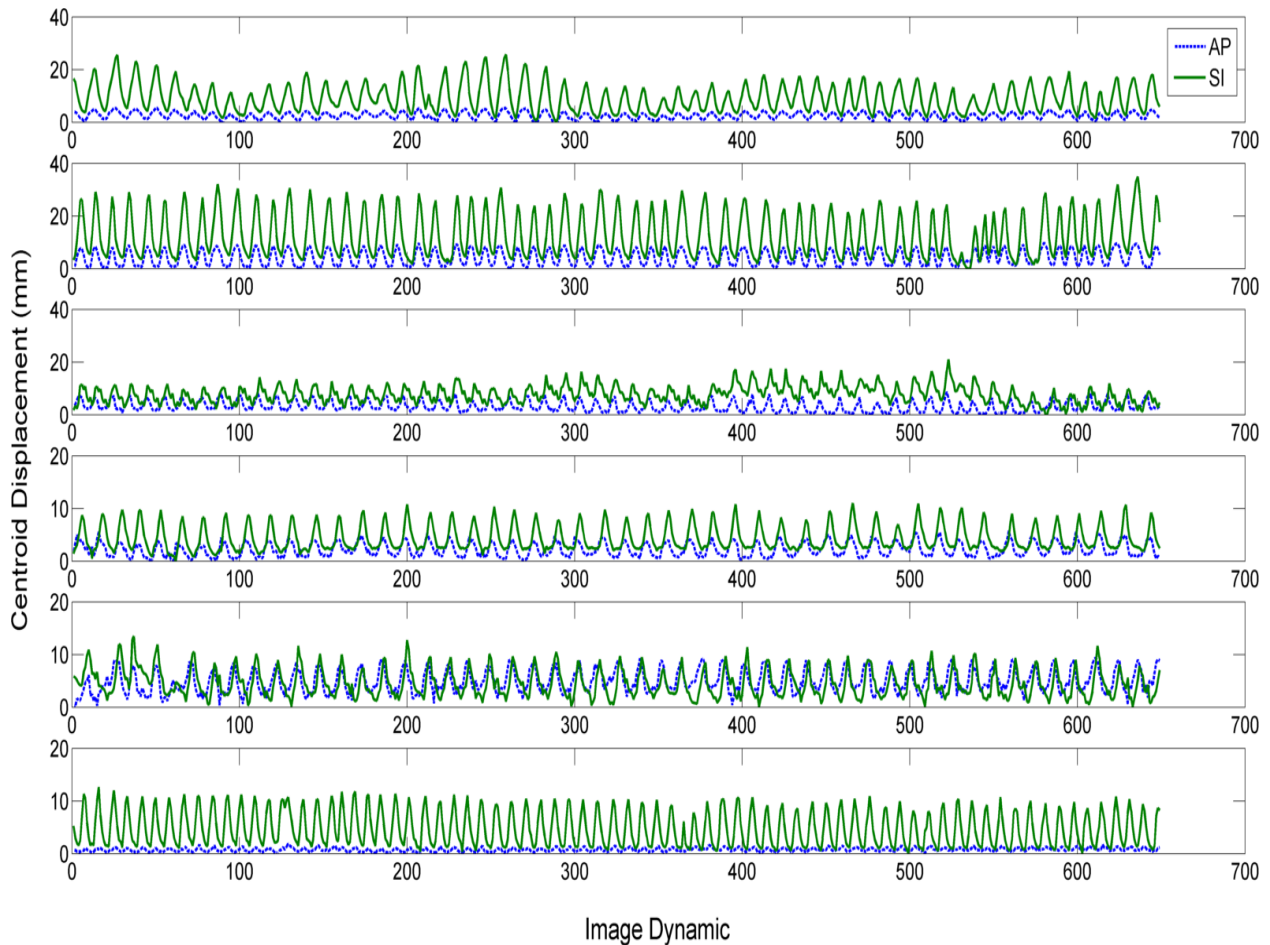


Figure 3-8: Degree of Superior Inferior (Green, Solid) and Anterior Posterior (Blue, Dashed) tumor motion of 6 patients.

### 3.3.1 Auto-Contouring Results

Results of comparing the automatically generated contours of the phantom and patients, to their respective standards are shown in table 3-4.

Table 3-4 – Dice’s Coefficient and Centroid Displacement Error of Autocontours compared against Standard.

		Dice’s Coefficient		Centroid Displacement Error (mm)	
		Mean (Std)	Max/Min	Mean (Std)	Max/Min.
<b>Phantom</b>	Sine Pattern	0.95 (0.01)	0.97/0.93	0.93 (0.29)	2.04/0.23
	Pattern 1	0.96 (0.01)	0.97/0.94	0.68 (0.24)	1.40/0.04
	Pattern 2	0.96 (0.01)	0.97/0.93	0.73 (0.24)	1.40/0.03
	Pattern 3	0.96 (0.01)	0.97/0.93	0.74 ( 0.24)	1.87/0.05
<b>Patient</b>	1	0.92 (0.03)	0.97/0.86	0.96 (0.52)	2.27/0.10
	2	0.90 (0.03)	0.95/0.82	1.22 (0.69)	3.77/0.12
	3	0.88 (0.05)	0.97/0.71	0.90 (0.55)	3.25/0.05
	4	0.89 (0.04)	0.89/0.77	1.31 (0.75)	3.10/0.07
	5	0.77 (0.07)	0.91/0.61	3.90 (1.65)	7.76/0.10
	6	0.89 (0.04)	0.95/0.72	1.55 (1.12)	5.86/0.09

From the results, one can see that that the auto-contouring method generates very accurate matches to the phantom standards; yielding the DC of 0.95-0.96 and the centroid error of 0.68-0.93 mm. For 5 of 6 patients, the match between the automatic contours and the gold standard contours is still high, yielding the DC of 0.88-0.92 and the centroid displacement of 0.96 – 1.55mm. Patient 5’s agreement is noticeably poorer compared to other 5, with a DC of 0.77 and a centroid displacement of 3.90 mm.

### 3.3.2 Intra-observer/Inter-observer Reliability

The evaluation of intra-observer variability ( $ROI_{STD}$  vs  $ROI_{INTRA}$ ) is shown in Table 3-5, and the inter-observer variability ( $ROI_{STD}$  vs.  $ROI_{INTER}$ ) is shown in Table 3-6.

Table 3-5 – Intra-observer variability

		Dice's Coefficient		Centroid Displacement Error (mm)	
		Mean (Std)	Max/Min	Mean (Std)	Max/Min.
<b>Patient</b>	1	0.90 (0.03)	0.95/0.81	1.12 (0.62)	2.73/0.02
	2	0.92 (0.02)	0.96/0.86	1.10 (0.59)	2.69/0.04
	3	0.89 (0.04)	0.97/0.77	0.96 (0.47)	2.96/0.05
	4	0.93 (0.02)	0.98/0.89	0.94 (0.49)	2.10/0.94
	5	0.74 (0.08)	0.90/0.48	5.07 (1.43)	8.48/1.69
	6	0.89 (0.03)	0.95/0.79	1.64 (0.87)	4.10/0.22

The auto-contouring accuracy against standard ( $ROI_{AUTO}$  vs  $ROI_{STD}$ ) in terms of Dice's Coefficient ( $DC_{AUTO}$ ) for each of the 6 patients is shown next to the intra-observer variation ( $ROI_{STD}$  vs  $ROI_{INTRA}$ ) and inter-observer variation ( $ROI_{STD}$  vs  $ROI_{INTER}$ ) in terms of the Dice's coefficient ( $DC_{INTRA}$ ,  $DC_{INTER}$ ) in Figure 3-9.  $DC_{AUTO}$  is significantly higher than  $DC_{INTRA}$  in patients 1, 5, while being significantly lower than  $DC_{INTRA}$  in patient 2 and 4, as indicated by the non-overlapping 95% confidence intervals in Figure 3-9. On the other hand,  $DC_{AUTO}$  is higher significantly higher compared to  $DC_{INTER}$  for patients 1, 2, 6, and significantly lower in patient 4 and 5.

Table 3-6 – Inter observer variability

		Dice's Coefficient		Centroid Displacement Error (mm)	
		Mean (Std)	Max/Min	Mean (Std)	Max/Min.
<b>Patient</b>	1	0.89 (0.04)	0.95/0.79	1.28 (0.71)	4.32/0.08
	2	0.83 (0.05)	0.92/0.69	1.62 (0.78)	3.53/0.26
	3	0.89 (0.04)	0.97/0.78	0.90 (0.46)	2.19/0.09
	4	0.93 (0.03)	0.98/0.88	0.96 (0.51)	2.42/0.12
	5	0.84 (0.04)	0.94/0.66	2.77 (1.54)	7.52/0.14
	6	0.85 (0.04)	0.92/0.75	1.72 (0.94)	4.82/0.17

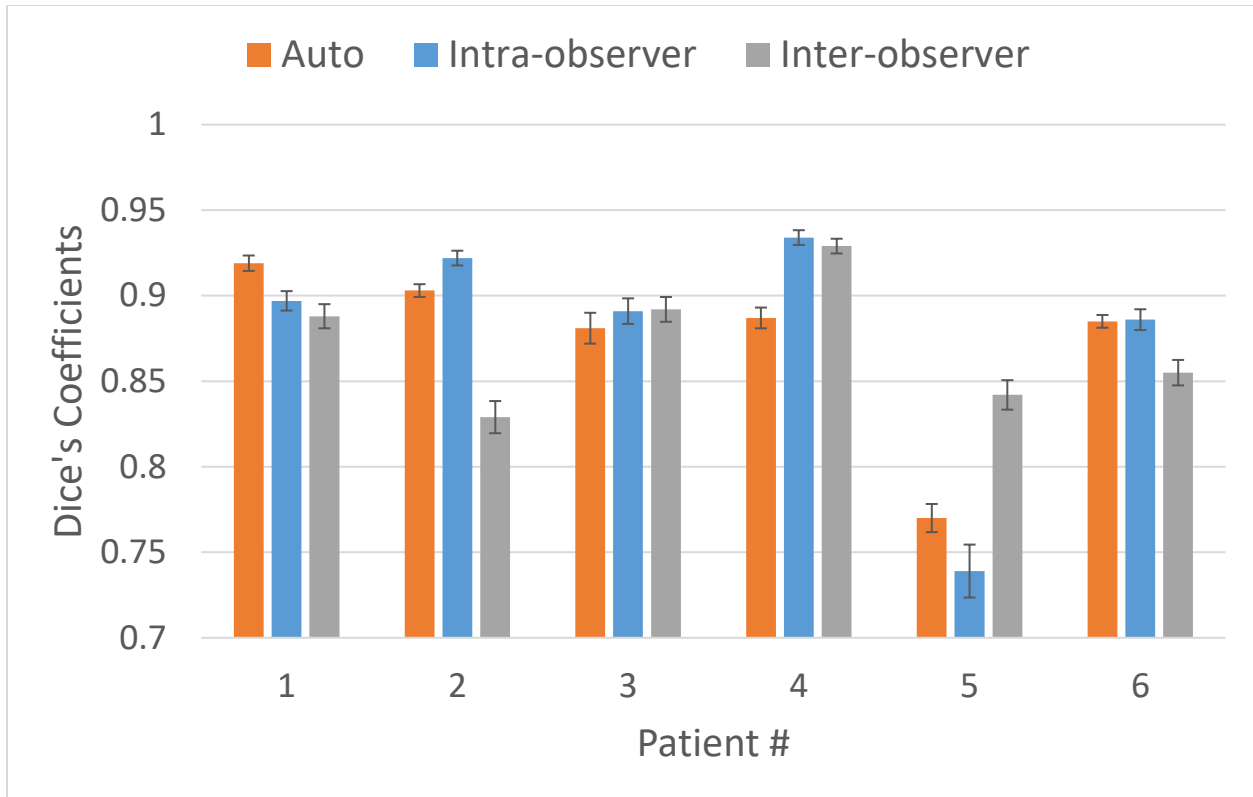


Figure 3-9 Intra-observer variations, ( $DC_{INTRA}$ , blue) and Inter-observer variations ( $DC_{INTER}$ , gray) for all 6 patients is plotted next to autocontouring accuracy in terms of Dice's coefficient, ( $DC_{AUTO}$ , orange). Error bars represents 95% confidence interval.  $DC_{AUTO}$  is significantly larger than  $DC_{INTRA}$  in patients 1 and 5, while significantly lower in patients 2 and 4.  $DC_{AUTO}$  is significantly larger than  $DC_{INTER}$  in patients 1, 2 and 6 and significantly lower in patients 4 and 5.

### 3.4 Discussion

It should be noted that there are some inherent differences in performing imaging at the 0.5 T field of the Linac-MR vs 3 T of the present clinical system which cannot be easily accounted modeled in degrading the 3T images into equivalent 0.5T images. Firstly, at 0.5 T, substantially less SAR is deposited to the patient. Therefore, the larger flip angles at high speeds can be used at 0.5 T as opposed to 3T systems limited by the clinical SAR. The larger flip angle in bSSFP generates images with a higher SNR. Secondly, the balanced SSFP sequences tend to be less affected by banding artifacts at 0.5 T compared to 3T, even though, after the application of local shimming around the tumour, there are no bands are observed near the tumour regions in our experiments.

The CNR results from Table 3-2 indicate some differences between phantom and patients. There are several reasons as to why matching phantom and patient CNR in the lung can be quite

difficult. Firstly, as one can observe from Fig. 3-6, the phantom tumour has considerably higher signal amplitude compared to that of the patients' tumours. The patient tumour is heterogeneous (i.e. contains a mixture of tissue, air, vessels, etc.), with some pixels of considerably lower signal compared to others; this may lead to an average PD in the tumor region to be lower compared to PD of muscles. The muscle tissue was used as the basis of the homogeneous tumour model in the phantom. Secondly, the surrounding solution contained in the "phantom thorax" may not fully simulate the coil load generated by the patient's body and the resulting body noise is highly dependent on accurate geometry. Finally, as shown in Eq. 2.74, the  $T_1$  tends to increase with magnetic field strength, and hence the  $T_1$  of patient tumour is likely higher compared to the phantom tumour model which has its  $T_1$  deliberately lowered to mimic 0.5 T contrast. According to Eq. 2.65, bSSFP signal decreases with higher  $T_1$ . All these factors may contribute to the higher signal in the phantom's lung tumour image. The phantoms' lung parenchyma also has significantly higher SNR compared to the ones in the patients, in which there is almost no detected signal. One possible reason is that the lung parenchyma in the sagittal slice has a lower PD (as the range of PD from references is 0.20-0.31) than the phantom (0.30). The other two factors, i.e. underestimation of the noise in the phantom's image and shortening of the  $T_1$  in the phantom, increase SNR, contributing to a higher SNR in the phantom's images.

Despite of all these limitations of the pseudo 0.5 T images, these images have a range of CNR's that are reasonably similar; 3.1 – 6.7 for patients, 7.5 – 8.2 for phantom. Particularly, the patients' CNR's values are likely an underestimate of the real CNR values attainable at 0.5 T. If the tumour tracking performs effectively via tumour segmentation in these images, it can be assumed to be as effective in the actual 0.5T images of the Linac-MR system, or for similar images with higher CNR.

One can observe from Table 3-4 that the auto-contouring algorithm yields a closer match in the phantom data compared to patients' images. There are inherent differences between the two sets of experiments. In the phantom study, the tumour contours in the standard images are obtained only once, in high quality, high resolution images containing homogeneous tumour. Due to these favorable conditions, the variability within the "gold standard" set of contours is expected to be very small. On the other hand, in the patient images, the  $ROI_{STD}$  are generated by the radiation oncologist on every image, at a lower resolution, containing a more heterogeneous

tumour. The variability in the oncologist’s test standard contours will have a negative impact on the tumour tracking metrics in terms of agreement between the standard contours and the auto-contours, even though this source of error has nothing to do with the auto-contouring algorithm itself. This is supported by the results from our intra-observer/inter-observer variation study shown in Table 3-5. In terms of the Dice’s Coefficient, as shown in Figure 3-9,  $DC_{AUTO}$  and  $DC_{INTRA}/DC_{INTER}$  are generally comparable. This result is perhaps unsurprising, as a recent study<sup>72</sup> has shown that the intra-observer variation for primary lung tumour volumes for 4DCT has Dice’s coefficient values from 0.77 to 0.83. On the other hand, the patient 5 represents a particularly difficult case for the automatic algorithm due to the ambiguous group of pixels (red arrow in Figure 3-10) around the tumour. This region is missed by the auto-contouring algorithm ( $ROI_{STD}$ , bottom left) leading to a reduced  $DC_{AUTO}$ . However, an experienced radiation oncologist, on a different day, contoured an even smaller area ( $ROI_{STD2}$ , bottom right), leading to an even lower  $DC_{INTRA}$ . Clearly, ambiguous pixels with similar brightness to the tumour present a challenge for both an experienced human observer and the auto-contouring algorithm alike, and improving robustness of the algorithm in these situations will require further research and development.

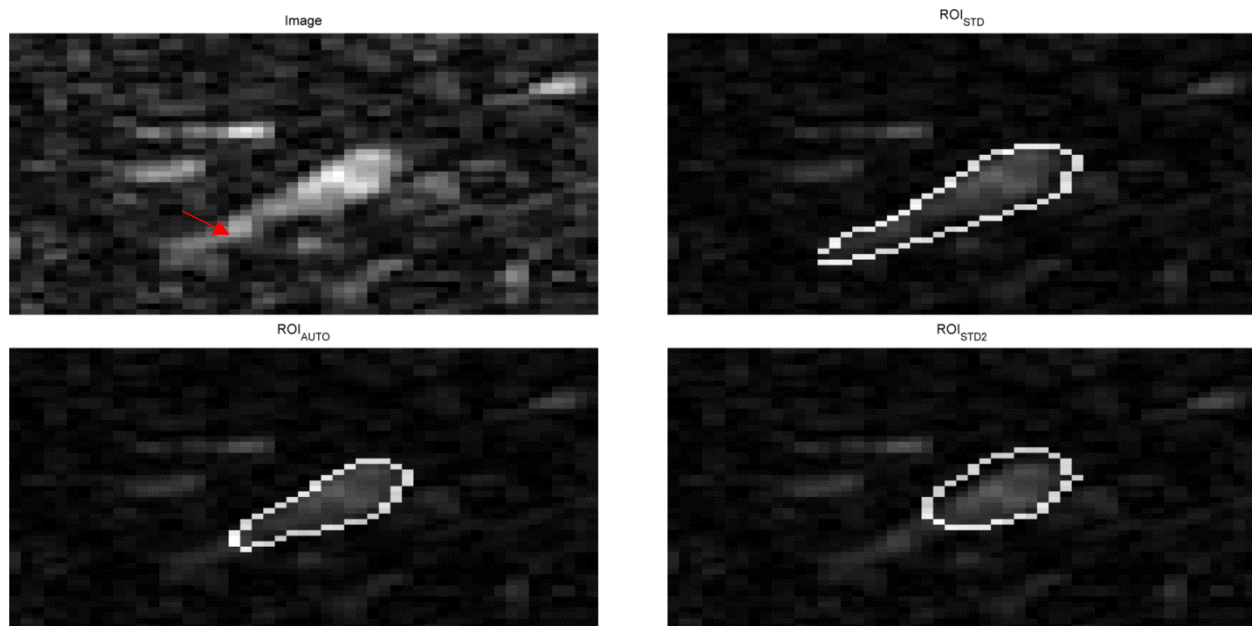


Figure 3-10: Example contours of the most difficult case encountered in our data (patient 5). Top Left – Image to be contoured, with ambiguous region shown by the red arrow. Top right,  $ROI_{STD}$  contoured by the radiation oncologist. Bottom left  $ROI_{AUTO}$  contoured by the automatic algorithm, missing part of the ambiguous region. Bottom left  $ROI_{STD2}$ , contours drawn by the same oncologist on the identical image/window/level on a different day.

### 3.5 Summary

In this chapter, we have described the phantom and patient experiments in which the neural network based algorithm for automatic tumour segmentation, developed at the CCI, is validated. In phantom experiments, the automatic contours show a very high agreement (DC 0.95-0.96) with a set of gold standard contours in high resolution imaging combined with optical encoders. In 5 of 6 patient experiments, the automatic contours show a high agreement (DC = 0.88-92) with a set of contours manually contoured by a radiation oncologist, these numbers are comparable to intra and inter-observer variations. For patient 5, the contouring algorithm fares poorly (DC = 0.79) due to some ambiguous structures (Figures 3-10), however this is still higher compared to intra-observer reliability (DC = 0.74). After validation, this automatic contouring algorithm itself is used as one of the tools to validate MR acceleration strategies described in the following chapters. Instead of contouring identical images and comparing human vs algorithm, the same algorithm will be used to contour images using different acceleration strategies. For identical images, the algorithm yields identical contours. Accelerated images, reconstructed with only partial k-space will necessarily suffer from some image reconstruction errors, studying how that affects the auto-contouring output yields insight about the quality of the image reconstruction strategy.

## Chapter 4 Prior Data Assisted Compressed Sensing

*Parts of this chapter have been adapted from a published article: Yip E, Yun J, Wachowicz K, Gabos Z, Heikal A, Rathee S, Fallone BG. Prior Data Assisted Compressed Sensing: A Novel MR imaging strategy for real time tracking of lung tumors. Medical Physics. 2014;41(8):082301 (12pp.)*

### 4.1 Introduction

In order for the real time image guidance of the Linac-MR system to be beneficial in tumour tracking, the system's delay time, i.e. the total time required for image acquisition, image reconstruction, tumor auto-contouring and MLC collimation, should be shorter than 0.5s, according to the AAPM's task group report on respiratory management, TG-76<sup>22</sup>. We have previously shown<sup>3</sup> that the fast MR sequences, such as balanced steady state free precession (bSSFP), can acquire a single 2D slice at 4 frames per second at a modest spatial resolution (~3mm). However, accelerated MR acquisition can benefit tumor tracking in several ways: 1) by increasing imaging frame rate, or 2) by increasing the spatial resolution, or 3) by imaging more planes while maintaining the necessary frame rate. The acquisition of images in 3D, or in multiple 2D orthogonal planes, captures the 3D motion of mobile tumors<sup>73</sup>.

Compressed Sensing<sup>47</sup> (CS) has recently been applied to increase data acquisition speed in MRI by reducing the amount of acquired k-space data. CS relies on the assumption that the reconstructed MR image has a known sparse representation. Under-sampling of the k-space is performed in a pseudo-random manner to ensure that the ensuing aliasing artifact appear as incoherent, noise like structure in the conventionally reconstructed image. The final image is reconstructed using an iterative method that removes these artifacts by promoting sparsity in a transformed domain while maintaining fidelity to the acquired k-space. CS can be applied to any MR sequence, including bSSFP, and unlike parallel MRI<sup>41,45</sup> methods, it does not require specialized hardware such as multiple array coils.

The original CS method proposed for MRI<sup>47</sup> is generally applied to non-dynamic MR image acquisitions. While this technique accelerates dynamic imaging, the maximum achievable under-sampling or acceleration potential is not reached if the temporal redundancy within the dynamic image series is not exploited. There have been several proposed methods, presented in

section 2.9.3, such as kT-Sparse<sup>61</sup> and kT SLR<sup>63</sup>, that exploit this spatial-temporal redundancy within the dynamic image series. However, these retrospective reconstruction methods are generally not suitable for real time image guidance, for two reasons. Firstly, these methods acquire the full dynamic dataset  $(x, y, t)$  before reconstruction commences, which makes them suitable for diagnostic purposes but not for real time image guidance. Secondly, even if these methods are modified to work on-the-fly, the data to be reconstructed is increased in dimension (i.e, from a single 2D image with domain  $(x, y)$  to a 2D temporal series with domain  $(x, y, t)$ ). This will significantly increase reconstruction time, making it unsuitable for real time uses. As an example, even with GPU implementation, the reported reconstruction time for k-T SLR reconstruction of an entire 2D time series of 70 images (128x128x70) is still too large at 8-10 minutes<sup>63</sup>.

In this chapter, we present a novel CS reconstruction method, Prior Data Assisted Compressed Sensing (PDACS), that is suitable for future use on-the-fly, while taking advantage of spatial-temporal redundancy. To assist in reconstruction, this method requires the acquisition of a series of prior data that spans at least one cycle of periodic breathing motion. Unlike the other spatial-temporal methods, this method has a similar reconstruction time to the original 2D CS technique. For validation, we retrospectively applied our technique to the dynamic data acquired for lung cancer patients, and evaluated the reconstruction technique by (1) assessing its image artifact power, and (2) applying our auto-contouring software to the reconstructed images.

## 4.2 Methods

### 4.2.1 Original CS Method

According to CS Theory described in Section 2.8.2, it is possible to accurately reconstruct an image from a small subset of k-space data if the following two conditions are met simultaneously:

1. The desired MR image has a sparse representation in a known domain;
2. Undersampling of the k-space is performed in an incoherent manner so that the resulting aliasing artifacts appear incoherent and noise-like.

Some common sparse representations of MR images include the wavelet and discrete cosine transforms<sup>8</sup>. Additionally, a finite difference operation as a sparse transform has also been shown to produce satisfactory results<sup>8</sup>. For incoherent sampling, Lustig *et al.*<sup>8</sup> reported that the best results are obtained by using a pseudo-random sampling pattern governed by a probability distribution function that samples the centre of k-space more densely than the periphery. Let  $\tilde{\rho}$  represent the 2D MR image to be reconstructed by the CS method. In the original CS method, the two CS conditions pose a constrained optimization problem, which is solved by minimization of the following unconstrained penalized objective function (eq. 2.97)

$$\mathit{arg\ min}_{\tilde{\rho}} \left( \left\| \mathcal{F}\{\tilde{\rho}\}|_{k_s} - \mathbf{D}(k_s) \right\|_2^2 + \lambda \|\Psi_{2D} \tilde{\rho}\|_1 \right) \quad (2.97)$$

Where  $\tilde{\rho}(x, y)$  is the solution matrix in image space,  $k_s$  are the pre-defined incoherent sampling k-space locations,  $\mathcal{F}\{\}$  is the 2D Fourier Transform operator,  $\mathbf{D}(k_s)$  represents acquired data in k space  $(k_x, k_y)$ . The minimization of L<sub>2</sub> norm enforces fidelity of the solution's k-space representation to the originally acquired k-space data. In the L<sub>1</sub> regularization term,  $\Psi_{2D}$  represents a sparsifying transform (e.g. wavelet, discrete cosine or finite difference). Some commonly used optimization techniques to solve this problem include the conjugate gradient method used by Lustig *et al.*<sup>8</sup>, and the Split Bregman method proposed by Goldstein *et al.*<sup>15</sup>.

#### 4.2.2 Spatial-Temporal CS

The conventional 2D-CS method treats each 2D image of the dynamic series as an independent image. However, this approach does not exploit the temporal redundancy of the data. To address this, a modification to the conventional CS method has been made to incorporate temporal information in the k-T SPARSE<sup>11</sup> method. In the k-T SPARSE method, the random sampling pattern is a function of the k-T domain i.e.  $(x, y, t)$ . The modified objective function is given as follows.

$$\mathit{arg\ min}_{\tilde{\rho}} \left( \left\| \mathcal{F}_{x,y}\{\tilde{\rho}(x, y, t)\}|_{k_s} - \mathbf{D}(k_s) \right\|_2^2 + \lambda \|\Psi_{3D}\{\tilde{\rho}(x, y, t)\}\|_1 \right) \quad (2.99)$$

In this formula  $\mathcal{F}_{x,y}$  represents 2D Fourier transform, applied only to the two spatial dimensions  $(x,y)$  of the 3D solution matrix  $\tilde{\rho}(x, y, t)$  in order to enforce consistency for all data acquired,  $k_s$  represents the selected sampling points in the 2D temporal series represented by  $(x, y, t)$

coordinates.  $\Psi_{3D}$  represents a 3D sparsifying transform, often including the standard wavelet/discrete cosine in the two spatial dimensions (x, y) as well as a Fourier transform in the temporal dimension. As shown in section 2.9.3, there are numerous approaches, discussed in the literature, that are even more sophisticated than the k-T SPARSE method. However, while these approaches have much greater acceleration potential due to the exploitation of spatial-temporal data, they can be computationally intensive in an iterative reconstruction process, and thus these are ill-suited for real time applications.

#### 4.2.3 Prior Data Assisted CS (PDACS)

We propose a novel approach, PDACS, to improve the image acquisition speed adequate for real time MR tumor tracking by the acquisition of training data prior to the real time dynamic data acquisition. In the real time radiotherapy scenario, these training data will add to the total treatment session time but not to the system delay during the dynamic acquisition. We modify the objective function by adding a second fidelity term to constrain the un-sampled locations of k-space,  $k_{us}$  of the solution to the mean prior data,  $\bar{\mathbf{D}}(k_{us})$  as the following.

$$\begin{aligned} \mathit{arg\ min}_{\tilde{\mathbf{p}}} & \left( \|\mathcal{F}_{2D}\{\tilde{\mathbf{p}}(x, y)\}|_{k_s} - \mathbf{D}(k_s)\|_2^2 + \lambda_1 \|\Psi_{2D}\tilde{\mathbf{p}}(x, y)\|_1 \right. \\ & \left. + \lambda_2 \|\mathcal{F}_{2D}\{\tilde{\mathbf{p}}(x, y)\}|_{k_{us}} - \bar{\mathbf{D}}(k_{us})\|_2^2 \right) \end{aligned} \quad (4.1)$$

In this approach, instead of performing multiple 2D Fourier Transforms and 3D sparsifying transform, only a single 2D Fourier Transform and 2D sparsifying transform are required in each iteration. To construct quality image with PDACS it is important for the prior data  $\bar{\mathbf{D}}(k_{us})$  to be as similar to current data  $\mathbf{D}(k_s)$  as possible. For tracking motion that are near periodic such as the lung motion, a simple solution is to acquire  $\bar{\mathbf{D}}(k_{us})$  over at least a single breathing cycle, generating composite prior data with contributions from different tumour locations along its motion trajectory. This compromise allows  $\bar{\mathbf{D}}(k_{us})$  to always be a “reasonable” match to the current data  $\mathbf{D}(k_s)$  as it tracks the tumour in real time. The reconstruction weight  $\lambda_2$  is chosen to be  $< 1$  to indicate that the prior data will be given less weight compared to the most current data acquired in the dynamic scan. The idea of anchoring CS reconstruction to a similar, previously acquired image has been shown to work well in CT, in a method called PICCS<sup>74</sup>.

It should be noted that the tumour motion must still be captured by the currently acquired data in the under-sampled k-space, and not by the prior data. Nevertheless, in very poorly defined problems, such as the case where there are large regions of k-space with very little fidelity information, the addition of prior data containing only an “approximate” solution can still improve the overall image quality significantly. The slightly mismatched k-space may result in some artifacts in the image, which the algorithm reduces with the  $L_1$ -regularization term. The positional integrity of the moving parts in the image is expected to be preserved as the “current” data in the relatively central areas of the k-space contains most of the energy in the image, and is given a higher weight by the PDACS algorithm. In this work, CS and PDACS reconstruction is performed with MATLAB implemented Split Bregman method<sup>15</sup>, introduced in Section 2.8.3 using the finite difference operator as  $\Psi_{2D}$ .

#### **4.2.4 Retrospective Study Based on *in-vivo* Data**

To test our image reconstruction methods, we performed a series of retrospective studies based on fully acquired data from lung cancer patients. While the PDACS reconstruction method is designed to work on the fly, the retrospective study is a common method to test and evaluate image acceleration methods as the fully acquired data set serves as a gold standard for the evaluation of reconstructed images. Several under-sampling fractions of k-space are simulated by the application of varying k-space sampling patterns. Each sampling pattern is a binary image in which a particular k-space point is either sampled (i.e. ‘1’) or not sampled (i.e., ‘0’). The binary mask image is pixel by pixel multiplied with the fully acquired k-space to simulate under-sampling. The under-sampled k-space is reconstructed using the conventional 2D-CS and the PDACS, and the resulting images are compared against images obtained with the fully sampled data, as a simple way of comparing different reconstruction techniques.

#### **4.2.5 MR Data Acquisition/Manipulation**

This study is focuses on patient data, and uses 6 patients with non-small cell lung cancer were recruited which were recruited with with institutional ethics approval. The patients are imaged in a 3T MR Acheiva Scanner (Philips Medical Systems, The Netherlands) for three minutes under free breathing. Dynamic images were acquired using a 2D bSSFP sequence at  $\sim 4$  fps (FOV: 40 cm x 40 cm, 3.1 mm x 3.1mm x 20 mm, TE = 1.1ms, TR = 2.2 ms, Dynamic Scan Time = 275ms) in a sagittal plane containing the lung tumor. The images are acquired using a 6 channel

torso coil. The data from the individual coils are first combined and then treated as single coil data for further use in retrospective undersampling and reconstruction. In order to preserve fully sampled complex data for our retrospective study we turned off all the acceleration methods available on the scanner. Moreover, we chose a relatively large FOV as to ensure the applicability of our methods in most clinical scenarios (i.e. a smaller patient could allow for improved resolution). With these restraints, the achieved spatial resolution at 4 frames per second is relatively modest. However, we expect that in actual clinical scenarios, with acceleration and smaller FOV that is chosen specifically for particular patient anatomy, the resolution can be improved significantly.

To explore the potential impact of SNR on CS reconstruction, the CS experiments are performed on both the original 3T images, and the noise added, pseudo 0.5 T images, for the measured SNR/CNR of these images, please refer to Table 3-3 in section 3.3.4.

#### **4.2.6 Generation of Sampling Patterns**

Coherent undersampling of k-space violates the Nyquist criterion, leading to coherent aliasing artifact (i.e. copies of the imaged object) that is difficult to eliminate. However, Lustig et al., have shown<sup>47</sup> that incoherent sampling pattern leads to aliasing artifacts which appear as incoherent, noise like structures with much lower signal amplitude compared to imaged object, which can then be removed by the iterative reconstruction algorithm.

Random sampling patterns are generated using the Monte Carlo process described by Lustig et al.<sup>47</sup> For our study, we restricted the k-space undersampling so that only the phase encode direction is randomized as it is only practical to undersample along the phase encode direction in a Cartesian 2D MR bSSFP imaging sequence.

A probability density function (PDF) is defined, with the total area under the PDF scaled proportional to the degree of undersampling (total probability of  $0.4 \times 128$  for 40% undersampling). The PDF is separated into two zones: a central region where it is sampled with 100% probability and a peripheral region governed by a decreasing function defined as  $p(k) = (1 - k/k_{\max})^2$  where  $k/k_{\max}$  is the normalized distance from the k-space center. Once  $p(k)$  is defined, sampling patterns are generated in the manner described by Lustig et al.<sup>47</sup>: A uniformly distributed random number ( $0 < n(k) < 1$ ) is generated for each k space line location, and the line

locations where  $n(k) < p(k)$  are sampled. If  $n(k)$  results in a sampling pattern that violates the degree of undersampling, the pattern is rejected and a new pattern is created by generating new random numbers. Using this scheme, the algorithm then generates 1000 patterns with the correct number of sampling lines, and selects the pattern using a criterion suggested by Lustig et al<sup>47</sup>, as follows: an image consisting of a single signal peak is Fourier transformed into k-space, undersampled with every test pattern, and transformed back to the image domain. This resulting image is the point spread function (PSF) of an undersampling pattern; containing the original signal peak with many additional smaller side peaks due to incoherent aliasing. The sampling pattern whose PSF contains the lowest secondary side lobe is chosen as the pattern<sup>47</sup>. This single pattern was used for the entire dynamic sequence. It should be noted that the 2D Cartesian sampling is not the most effective way of generating an incoherent sampling pattern with variable density. Golden angle radial patterns<sup>75</sup> or variable density spiral trajectories<sup>76</sup> could lead to even more incoherent pattern and better image quality. However, image reconstructions with these types of trajectories require extra computation time for gridding. As the clinical feasibility of the dynamic image reconstruction algorithm is highly favored by the shorter reconstruction times, the non-Cartesian signal acquisition methods are not considered in the study.

To explore the effect of increasing acceleration factors, we generated sampling patterns that represent 50%, 40%, 30%, 25%, 20% of total sampling representing acceleration factors of 2, 2.5, 3.3, 4, and 5, respectively. The resulting sampling pattern are shown here. The chosen patterns, used for both CS and PDACS are shown in Figure 4-1.

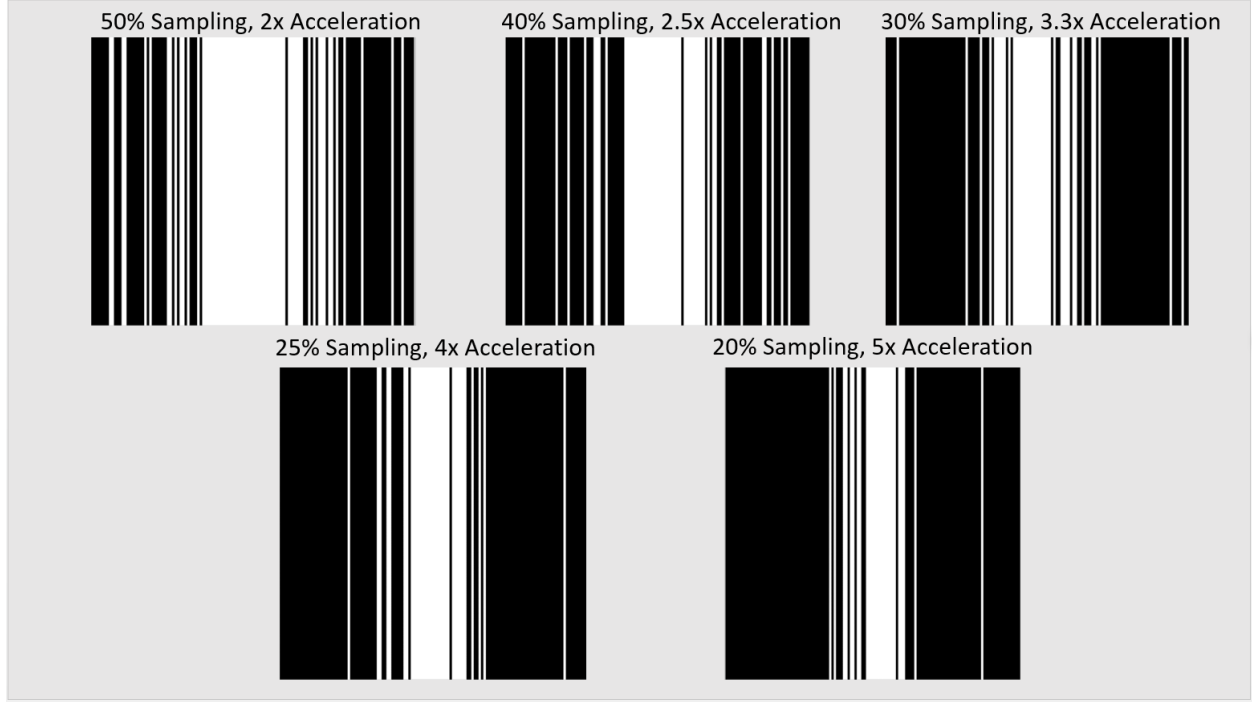


Figure 4-1 – Sampling Pattern in k-space used for 2D – CS and PDACS reconstruction

#### 4.2.7. Determination of Reconstruction Weights

The conventional 2D-CS method requires the estimation of parameter  $\lambda_1$  that represents the relative significance of the data consistency and the sparsity terms. In the proposed PDACS method however, the two parameters  $\lambda_1$  and  $\lambda_2$  must be determined which represent the relative importance of the complementary consistency and the sparsity terms. As the choice of appropriate weighting factors affects the quality of the reconstruction, it is important that the optimal weights are chosen. For this work, we optimize our weights in the following manner. A single fully sampled test image is chosen and the artifact power between the fully sampled image and various under-sampled test images is determined. The image artifact power is defined as

$$Artifact\ Power = \frac{\sum_i (\tilde{\rho}_{US} - \tilde{\rho}_{Full})^2}{\sum_i \tilde{\rho}_{Full}^2} \quad (4.2)$$

where  $\tilde{\rho}_{US}$  and  $\tilde{\rho}_{Full}$  are the images reconstructed from the under-sampled and fully sampled k-space respectively,  $i$  represents an index of individual pixels in the image. The algorithm then

determines optimal weights that minimize this error. In this study, we simply used the first image in the dynamic series as the test image for weight optimization. For time efficiency, optimization for  $\lambda_1$  in the 2D-CS method is performed in two steps: a “rough tuning” step in which  $\lambda_1$  varies in orders of magnitude followed by similar “fine tuning” step with a smaller change around the value determined in the first step. In the PDACS method,  $\lambda_1, \lambda_2$  are optimized jointly by varying both weights simultaneously using the same 2 step method. The ranges of tested values of  $\lambda_1$  and  $\lambda_2$  are from  $6 \times 10^{-6}$  to 0.4, and from 0.02 to 0.68 respectively. For the images acquired with our protocol, we have found that our reconstruction algorithm generates an acceptable solution using weights in the range of  $10^{-4} < \lambda_1 < 10^{-1}$  and  $0.02 < \lambda_2 < 0.1$ . While our optimization method doesn’t guarantee a global minimum, the region of weights searched (Figure 6) were generally adequate for a near optimal solution for images encountered in our MRI protocol, though this may require modification for images acquired with a different protocol. This optimization is practically feasible because a very few images are required (a single test image for CS in  $< 1$  second, 20 images of prior data for PDACS in  $< 6$  seconds) and the entire optimization takes less than 30 seconds. In the context of an actual treatment, the weight optimization may be performed immediately prior to the tracking scan. For this validation study, the optimization is performed for every pattern and patient combination.

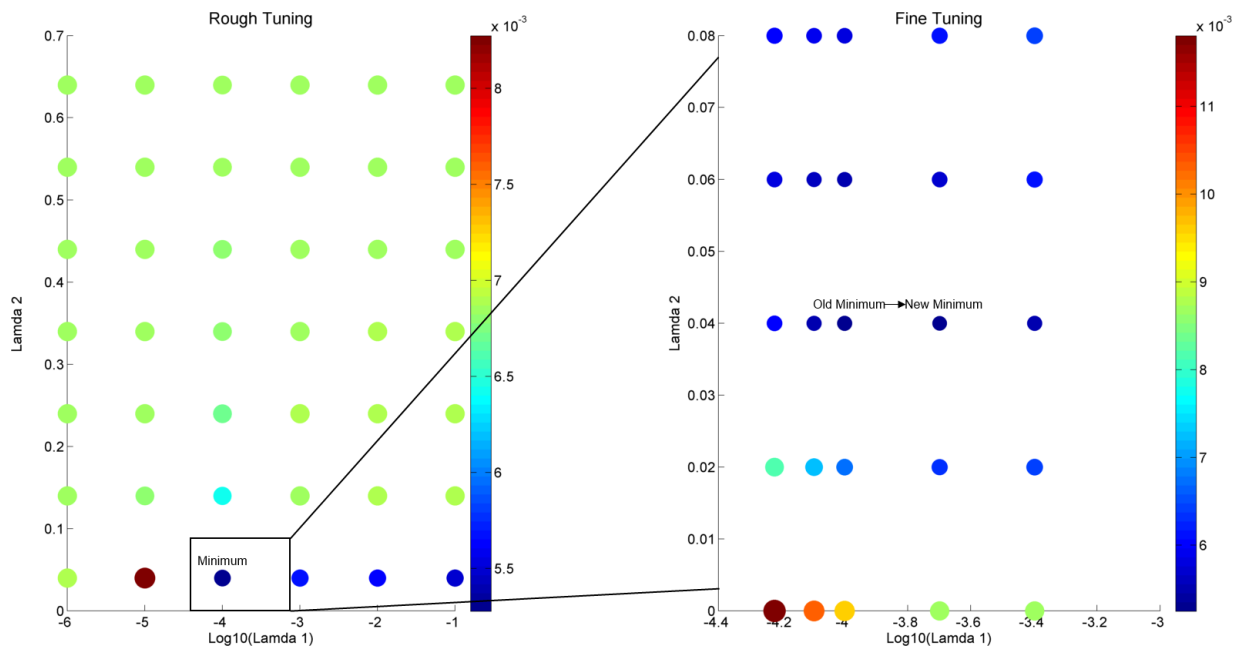


Figure 4-2 A plot describing the search for the optimal  $\lambda_1, \lambda_2$  values. Dots represent a tested pair of  $\lambda_1, \lambda_2$ , with the color and size of the dots representing the artifact power. Once the minimum is found in the rough search (left), a finer search (right) is performed in the neighbouring region.

One interesting aspect of the PDACS method is the solution that occurs when  $\lambda_1 = 0$ . In such a scenario, the solution would simply be a combination image between the under-sampled k-space in the current dynamic image and the complementary k-space data from the prior data, similar to many view-sharing methods<sup>20-23</sup>.

The optimized weights for 2D-CS are shown in Table 4-1.

Table 4-1 - Optimal weights  $\lambda_1$  for CS, determined by the 2-step algorithm for this study

Patient	Acceleration	3T	0.5T
		$\log_{10}(\lambda_1)$	$\log_{10}(\lambda_1)$
1	2	-3.22	-4.00
	2.5	-3.10	-3.92
	3.3	-3.22	-3.64
	4	-3.10	-3.76
	5	-2.92	-1.80
2	2	-3.00	-1.70
	2.5	-2.80	-3.67
	3.3	-2.92	-3.54
	4	-2.80	-3.54
	5	-2.00	-3.44
3	2	-3.00	-1.10
	2.5	-3.00	-1.40
	3.3	-1.49	-3.67
	4	-1.70	-1.70
	5	-1.49	-1.49
4	2	-1.10	-1.00
	2.5	-2.80	-1.40
	3.3	-1.10	-1.22
	4	-1.22	-1.32
	5	-1.32	-1.39
5	2	-3.00	-2.00
	2.5	-3.00	-2.00
	3.3	-2.80	-1.40
	4	-2.92	-1.70
	5	-1.49	-1.70
6	2	-2.80	-1.40
	2.5	-1.49	-1.70
	3.3	-1.40	-1.40
	4	-1.40	-1.49
	5	-1.40	-1.40

Table 4-2. Optimal weights  $\lambda_1, \lambda_2$  for PDACS, determined by the 2-step algorithm for this study.

Patient	Acceleration	3T		0.5T	
		$\log_{10}(\lambda_1)$	$\lambda_2$	$\log_{10}(\lambda_1)$	$\lambda_2$
1	2	-4.00	0.04	-4.70	0.10
	2.5	-4.00	0.04	-4.40	0.10
	3.3	-4.00	0.04	-4.40	0.10
	4	-4.00	0.04	-4.70	0.10
	5	-4.00	0.06	-4.70	0.10
2	2	-3.70	0.04	-4.22	0.10
	2.5	-4.00	0.06	-4.22	0.10
	3.3	-4.00	0.06	-4.22	0.10
	4	-4.00	0.06	-4.22	0.10
	5	-4.00	0.10	-4.22	0.10
3	2	-3.70	0.02	-0.40	0.04
	2.5	-3.70	0.02	-3.22	0.04
	3.3	-3.70	0.02	-4.40	0.04
	4	-3.70	0.02	-4.40	0.04
	5	-3.70	0.02	-4.22	0.04
4	2	-3.70	0.02	-4.10	0.04
	2.5	-3.40	0.02	-4.10	0.04
	3.3	-3.40	0.02	-4.22	0.04
	4	-3.70	0.02	-4.22	0.04
	5	-3.40	0.02	-4.22	0.04
5	2	-0.70	0.04	-4.40	0.12
	2.5	-1.00	0.04	-4.40	0.12
	3.3	-1.10	0.04	-4.40	0.12
	4	-2.10	0.04	-4.40	0.12
	5	-4.00	0.10	-4.40	0.12
6	2	-0.40	0.04	-4.22	0.20
	2.5	-3.70	0.04	-4.22	0.20
	3.3	-3.70	0.06	-4.22	0.20
	4	-3.70	0.10	-4.22	0.20
	5	-3.70	0.10	-4.22	0.30

To demonstrate the value of the more time consuming iterative  $L_1$  regularization step in PDACS, we also reconstructed view-sharing images by simply combining the same prior data with current k-space using the same random pattern to serve as a “control” dataset – that is PDACS without  $L_1$  regularization. As there are many viewsharing strategies in the MR literature, these images do not necessarily represent the most optimal viewsharing strategy, the determination of which is beyond the scope of this work.

#### **4.2.7. Image Reconstruction**

Using the weights shown in Tables 4-1 and 4-2, Split Bregman iterative reconstruction is performed to generate the 2DCS and PDACS images, using number of 10 inner iterative steps and 5 outer iterative steps as suggested by the author. The amount of time required is approximately 0.1s/ image, which makes this method potentially suitable for real time tumor tracking. In summary, we reconstructed each dynamic series using 3 methods: the conventional 2D-CS method without temporal acceleration which requires iterative reconstruction but no prior data; the view-sharing method which requires prior data but no iterative reconstruction; and finally, the PDACS method that requires both the prior data and iterative reconstruction. The reconstructed images are evaluated by looking at the overall artifact power and two different tumor tracking metrics.

#### **4.2.7 Evaluate of Overall Image Reconstruction Quality (Artifact Power)**

The overall quality of the reconstructed image is evaluated by calculating its artifact power, as defined at equation 4.2. In our evaluations, under-sampled images in simulations, performed at the 3.0T SNR, is compared to the fully sampled 3.0T images; while the simulations for 0.5T equivalent SNR is compared to the fully sampled 0.5T images. The superior reconstruction technique generates images with lower artifact power.

#### **4.2.8 Evaluation of Tumor Tracking Accuracy**

While the overall image quality of the image is important, for real time image guidance purpose, it is even more important that the under-sampled images accurately capture the dynamically changing location and shape of the tumor. Thus, we evaluated each reconstruction technique using our automatic tumor delineation algorithm for 6 patients validated in the chapter 3. For the analysis, the automatic algorithm was applied to the fully sampled images to generate a set of

“standard contours”. We then contoured the under-sampled images to obtain the set of test contours. The test contours are compared to the corresponding standard contours by using two separate metrics: centroid displacement (equation 3.3) and Dice’s coefficient (equation 3.1). Centroid displacement is simply the mean difference (in mm) of the tumor centroids of the standard and the test contours while the Dice’s coefficient measures the degree of overlap. . Artifact power, centroid position difference and Dice’s coefficient are evaluated using each of three reconstruction algorithms (2D-CS, PDACS, View-share). Please note that as this study is updated from the published study of patients 1-3, patient 5 was found to be an outlier due to poor reliability of auto-contouring on fully sampled images and thus it is excluded in the contouring analysis, but included in the artifact power analysis.

#### **4.2.9 Distinction between “Recent” vs. “Outdated” prior data**

As PDACS relies on the previously acquired prior data, the amount of time between the acquisitions of the prior vs current data may have an impact on PDACS images. The possible cause and quantitative analysis of this effect will be discussed in the next chapter. In this chapter, the first 20 images are treated as the prior data and the next 630 images are treated as dynamic test data and we limit our analysis for data acquired within 1 minute of prior data (Images 1 – 210 out of 630).

#### **4.2.10 3T vs Pseudo 0.5T Experiments**

The entire analysis is performed on both the original 3T images, as well as the noise added pseudo 0.5T images, as compressed sensing can be sensitive to SNR.

### **4.3 Results.**

#### **4.3.1 Image Evaluation – Global Image Quality (Artifact Power)**

A demonstration of image quality using different reconstruction methods is provided in Figure 4-3. At 2x acceleration, the organ contrasts in the image are qualitatively similar across the three methods, with a subtle difference in the view-sharing image that contains additional structured noise as pointed by the arrows. This difference is also evident in the quantitative artifact power comparison presented in Figure 4-4, where view-sharing method has slightly higher artifact power than PDACS method. At 5x acceleration, the resolution in the CS reconstructed image (Figure 4-3, second row, left) is poor compared to the other two techniques – this is again

supported by the artifact power analysis in Figure 4-4, where 2D-CS have very large artifact power at 5x acceleration. The overall trends in Figure 4-4 suggest that PDACS images generally have the lowest artifacts power as compared to the 2D-CS method and the view-share techniques. At the lower acceleration factors, 2D-CS performs well but the image quality deteriorates rapidly as the acceleration factor is increased. While the PDACS method generates the lowest artifact power overall, the advantage of PDACS relative to view-sharing method is reduced at high accelerations. At 0.5T SNR, artifact power is increased significantly in all three methods.

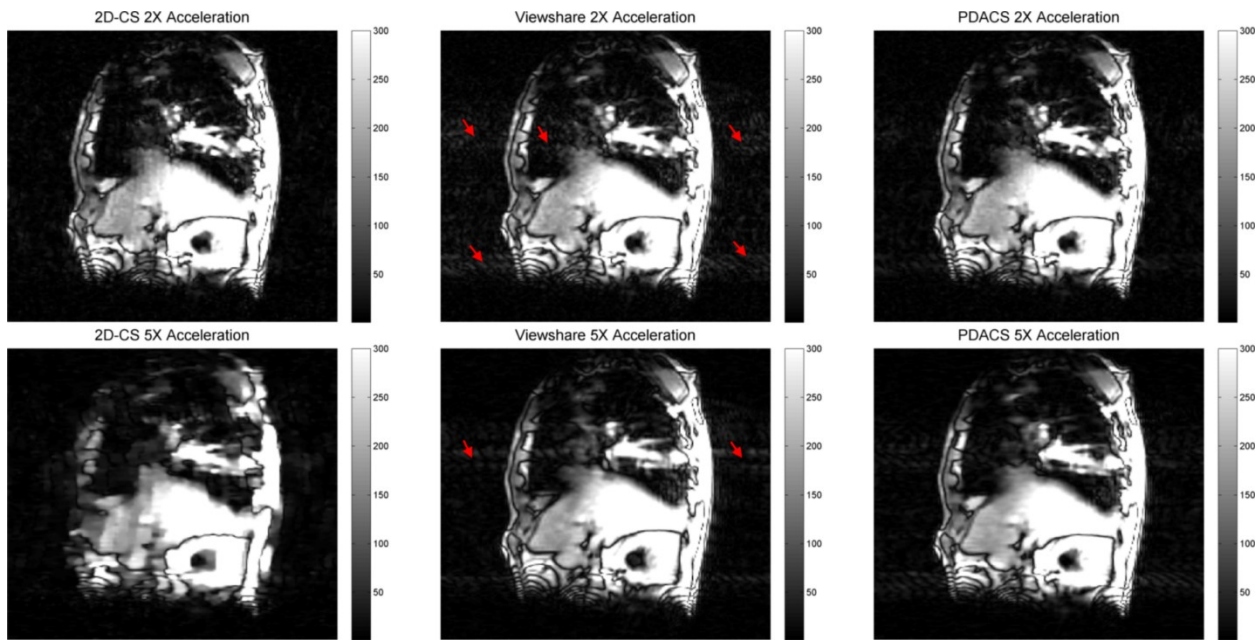


Figure 4-3 - Examples of reconstructed images based on the fully sampled image in Figure 2, top row, left. First Row: Reconstructed image at 2x acceleration (50% sampling), Left, 2D-CS; Centre, Viewshare; Right, PDACS; Second Row: reconstructed at 5x acceleration (20% sampling), Second Row: Left: 2D-CS, Centre, Viewshare; Right, PDACS. Red arrows indicate presences of noise like artifacts.

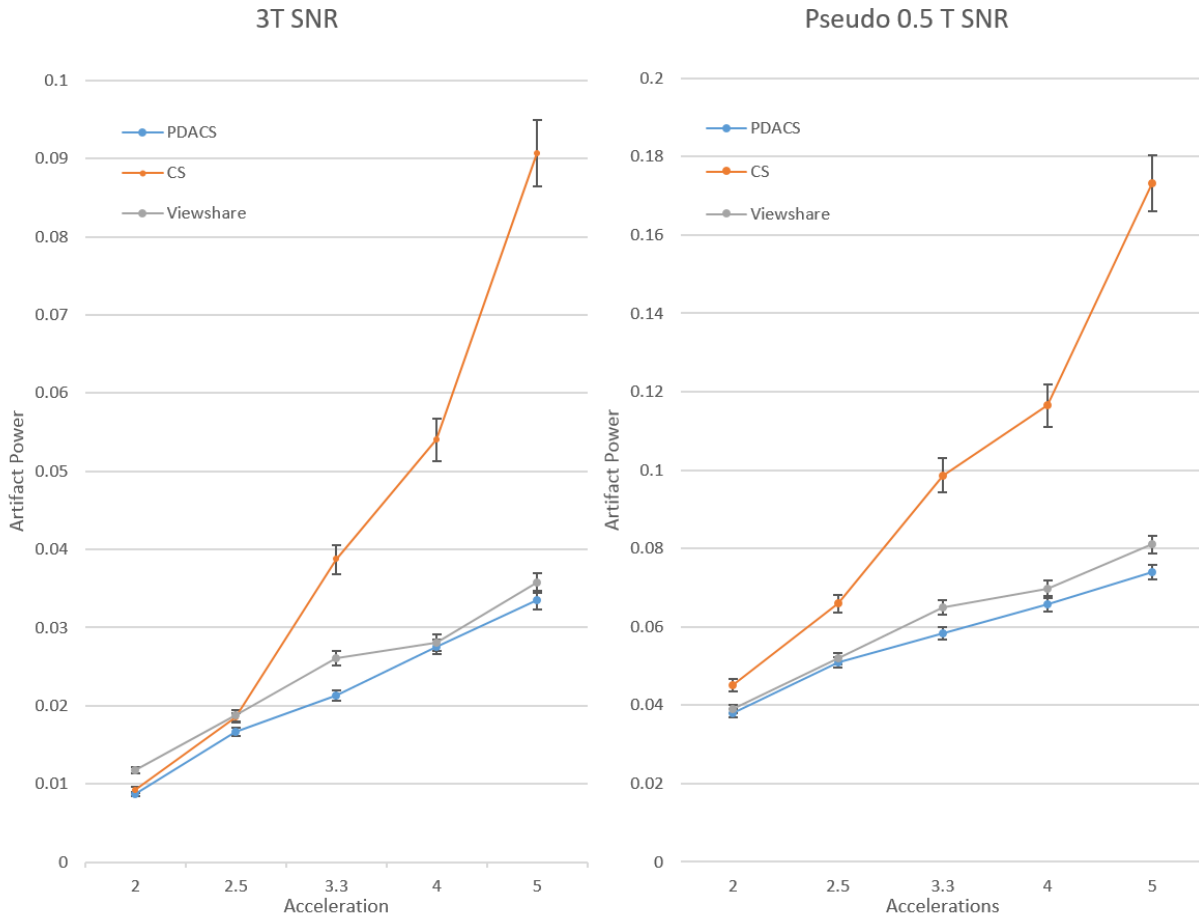


Figure 4-4 - Left: Aggregate artifact power for the three patients at the original 3T SNR images. Right: Aggregate artifact power in the pseudo 0.5 T SNR images. Please note the difference in y axis. Error bars indicate 95% confidence interval as determined from the standard error of the mean.

### 4.3.2 Tumour Tracking Accuracy.

The PDACS method essentially uses a motion averaged image as “prior data” which does not necessarily contain the accurate current tumour location to assist in reconstruction. Since the ultimate aim of the technique is to track moving lung tumours, it is therefore important to assess whether PDACS has any negative impact on the ability to accurately localize a tumour in the reconstructed images. Figure 4-5 contains a set of three zoomed in images of the tumour of the fully sampled image as well as 4x accelerated PDACS images at different phase of the breathing

cycle. While there are subtle differences between the two sets, the use of motion averaged supporting data does not significantly impact the ability to localize a tumour.

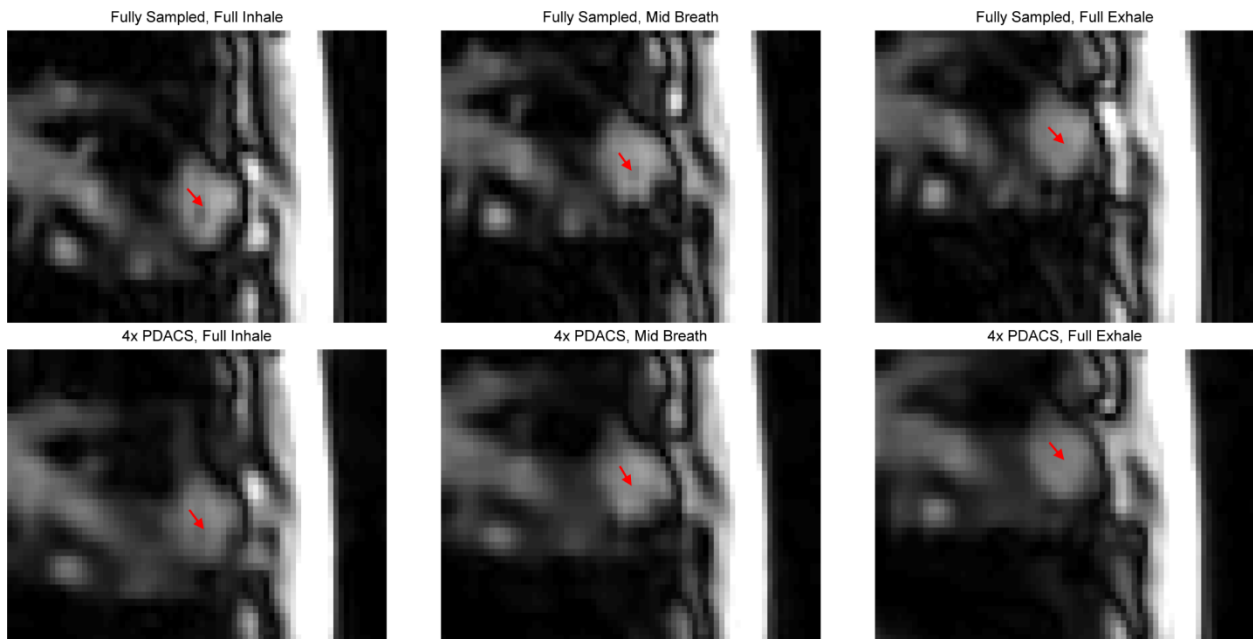


Figure 4-5 - Top Row: Zoomed in fully sampled images of the tumour as it undergoes breathing motion from inhale to exhale (Images 62, 65, 69). Bottom Row: Identical Images reconstructed with PDACS 4x acceleration. Tumour is indicated by red arrow.

For quantitative comparisons, Figures 4-6 and 4-7 show the results of Dice's Coefficient and the centroid displacement averaged over 5 patients and for both the original 3T and the equivalent 0.5T images. Using the Dice Coefficient metrics (Figure 4-6, left), CS gives the highest accuracy at 2x but its performance declines rapidly as the acceleration factor increases, with PDACS yielding the higher Dice's coefficient above 2x acceleration factor. At 0.5 SNR, CS performs relatively poorly, both PDACS and view-share methods provide substantial improvements over CS. (Figure 4-6, right).

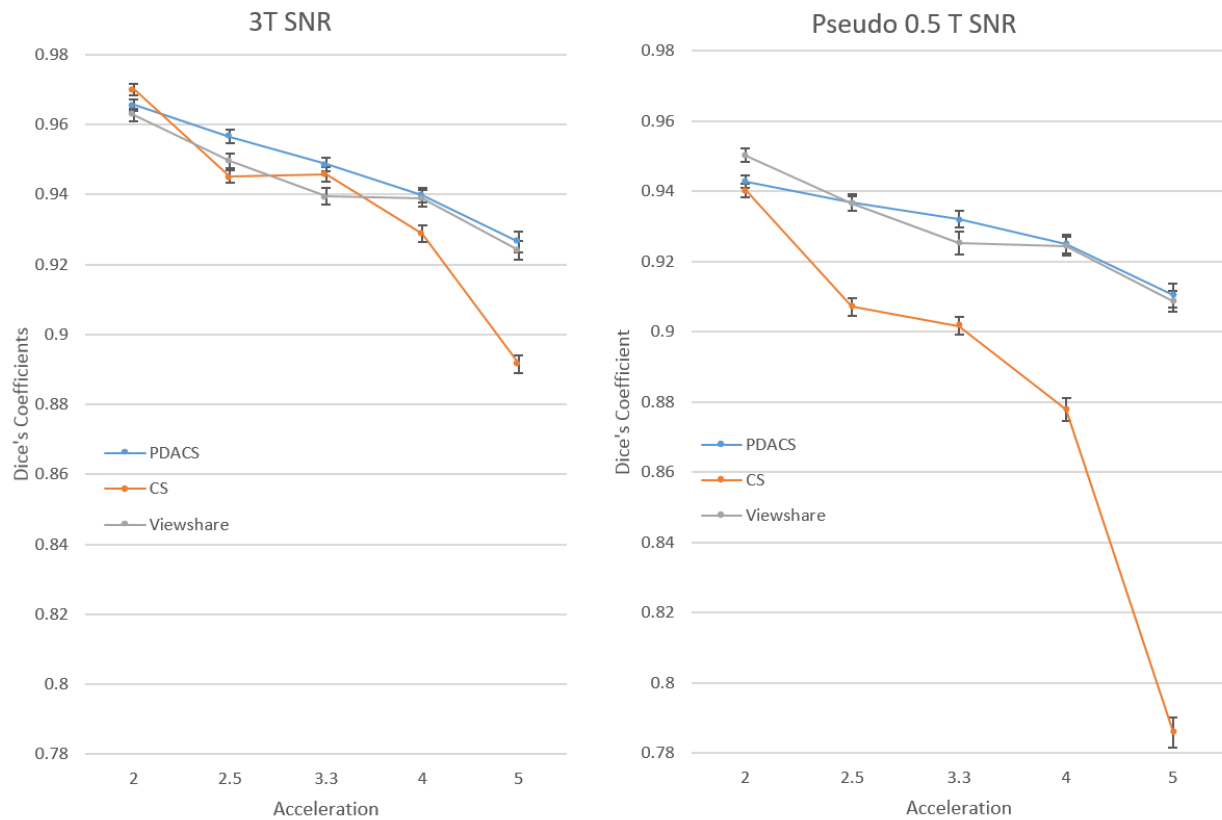


Figure 4-6 - Averaged Dice's coefficients, aggregated for 5 patients for all images reconstructed at the original 3T SNR (left) and the pseudo 0.5T SNR (right) with the increasing acceleration factor. Error bars indicate 95% confidence interval as determined from the standard error of the mean.

In the centroid error metrics at 3T (Figure 4-7, left), CS yields the lowest error at 2x acceleration while its performance decline at the higher acceleration, while PDACS is superior compared to CS above 2.5x acceleration factor. Between CS and view-sharing, it is unclear which method is generally superior, as this metric may not be sensitive enough to distinguish the techniques, except at 3.3x acceleration factor, where the PDACS method has statistically lower centroid error.

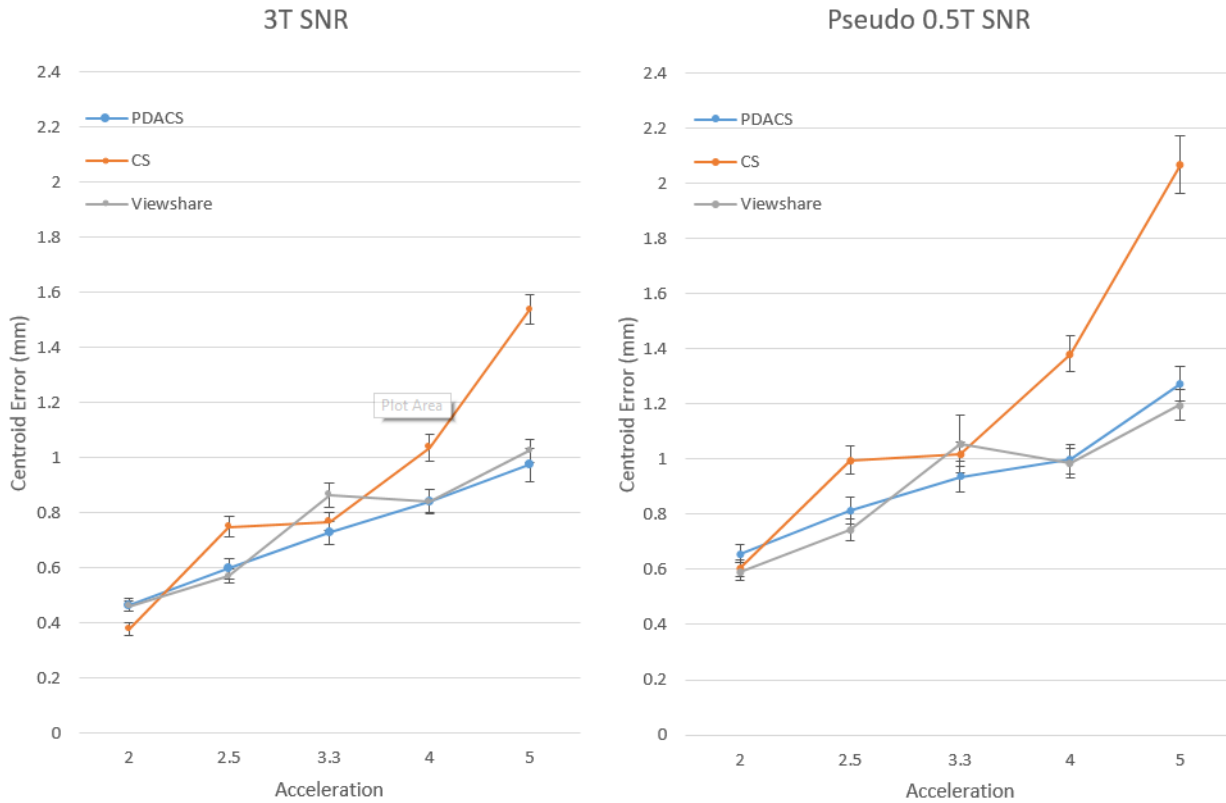


Figure 4-7 - Mean Centroid Displacement Error, averaged over 5 patients for all images reconstructed at the original 3T SNR (left) and the pseudo 0.5T SNR (right) with an increasing acceleration factor. Error bars indicate 95% confidence interval as determined from the standard error of the mean.

#### 4.4 Discussion

From the artifact power analysis (Figure 4-4) it is clear that the 2D-CS method is relatively sensitive to the degree of under-sampling in k-space. Heikal *et al.*<sup>25</sup> have shown that the under-sampling in compressed sensing causes quantifiable loss in spatial frequency response (as described by its Modulation Transfer Function) in reconstructed image. At lower acceleration factors, the sampling pattern still has a significant amount of sampled data points in the high frequency regions (Figure 4-1, top row). While the random under-sampling pattern would generate aliasing artifacts but these are subsequently removed by the iterative process. The small loss of response at high spatial frequencies makes very little qualitative difference in the image compared to the original image. However, with increasing acceleration factors, it becomes increasingly difficult to have sufficient sampling points at the high spatial frequencies of k-space (Figure 4-1, bottom row). With so few sampling points at the periphery, the CS algorithm is only able to generate an image with a significantly lower resolution (Figure 4-3, lower row, left column) as compared to the original image.

The premise of the PDACS and view-share methods is to provide the supporting data in the un-acquired regions of k-space to aid in reconstruction. Nevertheless, the quality of the PDACS and view-shared images is dependent on the similarity between the baseline k-space data and the up to date k-space information. With increasing acceleration factors, the final reconstruction contains less up to date information, thus reducing the quality of the reconstruction. In lung images, there is considerable temporal redundancy (since lung tumor motion contains periodicity). In our examples, the increase in artifacts at higher acceleration factors is shown to be considerably less compared to conventional CS. This leads to much more accurate tumour tracking for PDACS/Viewshare as compared to conventional CS.

To compare PDACS and view-sharing, one should consider an additional factor that limits the quality of these two techniques. A combination of k-space lines from data captured at different time points will result in discontinuous boundaries in k-space, generating noise like artifacts in the images domain. The PDACS algorithm has some success in reducing these artifacts at 3T as shown in Figure 4-3 and in Figure4-4. These artifacts appear to have some impact on tumour tracking algorithm, as indicated by higher Dice's coefficient for PDACS vs. view-share as shown in Figure 4-5, left. In other cases, the reduction in the artifact power does not translate to improved tracking metrics between PDACS and view-sharing.

In summary, the PDACS method combines advantages of the view-shared and CS methods. By solving the modified optimized problem as formulated in PDACS, with an additional constraint for prior data, the reconstruction takes advantage of the information in the un-sampled regions from the prior data, in a similar fashion to the view-shared method. In addition, iterative L1 minimization process in the CS/PDACS removes the aliasing artifacts in the CS images. This technique is also effective in removing artifacts that arise from the discontinuous k-space of the view-shared method. As a result PDACS gives better image quality than using 2D-CS and view-shared methods independently.

The quality of CS reconstruction also depends on the initial SNR of the image. Removal of aliasing artifacts generated from random under-sampling relies on the ability to, in the sparse domain, separate sparse but high intensity signal peaks from the lower intensity signals, which include both "noise like" artifacts that result from random under-sampling, as well as the inherent random noise present in a fully sampled image. Without prior data, this leads to the

generally poor result using the CS images. Our data suggests that the lower SNR images significantly benefit from the introduction of prior data as in the formulations of PDACS and view-share.

One should be cautious in interpreting the pseudo 0.5 T results, as our simulation is a simplistic approach that likely underestimates the quality of 0.5 T images, due to the following reasons. Firstly, at 0.5 T, reduced specific absorption ratio (SAR) allows for larger flip angles, partially compensating for lost SNR<sup>77</sup>. Secondly, imaging at 0.5 T is less sensitive to off resonance effects, reducing bSSFP banding artifacts<sup>77</sup>. Additionally, tissue contrast for bSSFP is determined by tissue relaxation properties (the ratio T2/T1) that are often improved at lower fields<sup>77</sup>. These effects are not accounted for in our pseudo 0.5 T simulations, which only serve as an indicator of how the algorithm performs in a “worst case scenario” for 0.5 T magnetic fields.

One important issue with applying CS to real time MR imaging is the reconstruction time. The 2D-CS and the PDACS methods require iterative optimization with similar reconstruction times; the reconstruction time per image is approximately 0.1s using a 3.4GHz CPU (Intel I7-4770). In a single plane tracking method, any potential gain in acquisition speed by the CS techniques will be reduced by this reconstruction time. However, in multiple slice imaging, the acquisition and reconstruction times are not equally important in the overall impact on the interventional MRI application. Consider an example of two different scenarios for a dynamic acquisition of 3 orthogonal slices (Figure 4-8). In the first scenario, no CS acceleration is performed, requiring 250ms of acquisition time but negligible reconstruction time. In the second scenario, acquisition speed is increased by a factor of 5x (50ms), at the cost of an additional 100ms of reconstruction time. While the sum of acquisition and reconstruction time for CS is 150ms (resulting in less than 2x acceleration compared to non-accelerated case), the reconstruction of individual slices are independent processes that could be performed in parallel using different CPU's. As a result, scenario 2 results in the orthogonal images that update every 150ms; a 5x improvement compared to scenario 1 in which the images are updated every 750ms.



Figure 4-8 - A schematic diagram demonstrating the benefit of speeding up acquisition time at the expense of increasing reconstruction time. As reconstruction of images from different slices are independent processes that can be performed in parallel, the accelerated scenario results in images that are updated at 150ms instead of 750ms in the first scenario

#### 4.5 Effect of Outdated Prior Data on PDACS and Viewshare

The work presented in this chapter demonstrates the benefits of prior data compared to CS. However, this analysis is limited to the first 210 images (~1 minute of data) after the prior data is acquired. For longer duration scans (>1 minute), it is observed in Figure 4-9 that the techniques which incorporate prior data (PDACS and view-share) suffer from an increase in artifact power as the scan progresses. On the other hand, the CS technique, which does not require prior data, has a constant artifact power. Consequently, this effect reduces the utility of PDACS for longer duration scans. A solution to mitigate this problem will be explored in the next chapter.

## Artifact Power, 5x Acceleration

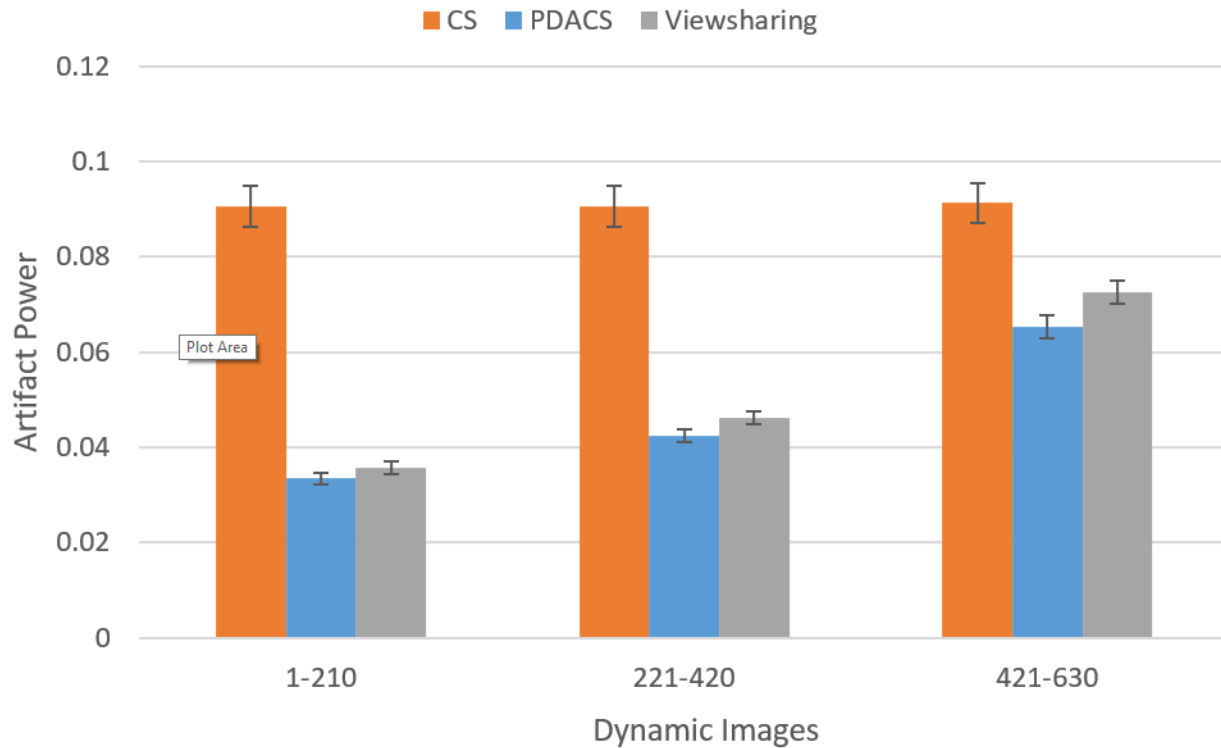


Figure 4-9 – Mean artifact power for all patients for 3T dynamic images 21-220, 221-430, 431-650. Progressive increase is artifact power observed for PDACS and viewsharing, where prior data is used, but not in CS where prior data is not used.

### 4.6 Summary

We have introduced a novel image reconstruction method, PDACS, which exploits the spatial-temporal redundancy in dynamic MR imaging. By combining the elements of compressed sensing with the view-sharing, we reconstruct images that are superior, in terms of artifact power, to both of these techniques when used separately. However, the utility for PDACS may be reduced for longer duration (>1 minute) dynamic scans.

## Chapter 5 Sliding Window PDACS

*Parts of this chapter have been adapted from an article in press: Yip E, Yun J, Wachowicz K, Gabos Z, Rathee S, Fallone BG. Sliding Window Prior Data Assisted Compressed Sensing for MRI tracking of lung tumours. Medical Physics. 2016; Accepted Author Manuscript. doi:10.1002/mp.12027*

### 5.1 Introduction

The original PDACS method, described in the previous chapter, pre-acquires a pool of preparatory data at the beginning of the dynamic sequence. This data is used as a motion averaged prior image. All subsequent acquisitions use a partial, randomly-sampled k-space pattern, and 2D images are reconstructed in sequence using a modified CS method that constrains the non-sampled k-space locations to an averaged prior data pool. In a sense, this original PDACS implementation represents some combination of compressed sensing and the KEYHOLE methods. While this approach is simple to implement and improves CS reconstruction for dynamic images<sup>78</sup>, there are large regions of un-sampled k-space in the dynamic images that may become progressively more mismatched to the prior data as the scan series progresses. Slow changes in the MR signal, possibly due to magnetic field instability arising from hardware heating<sup>79</sup>, or shifts in a patient's position during scans could lead to the prior data and the current data to be severely "mismatched" in longer duration scans, leading to image artifacts.

To illuminate the cause of the shift in baseline MR signal, a series of dynamic bSSFP images is acquired for the chest phantom described in Chapter 3, but without the motion in order to monitor the changes in the signal magnitude of the image. The pixel magnitude of image numbers 101, 201, 301, 401, 501, 601, and 701 is subtracted from pixel magnitude of image number 1. These images represent dynamic scans at 30 second intervals and the resulting difference images are shown in Figure 5-1. Initially, (i.e. #101, #201) only small changes are observed in the difference images, but in longer duration cases (bottom row) hot and cold spots can clearly be observed near bSSFP shifts, indicating a shift in bSSFP bands locations. Shifts in the bSSFP bands are caused by a change in phase, possibly due instability of  $B_0$  due to heating of some of the elements in the magnet. In addition to this effect, a gradual decline in signal can be

observed in the body of the phantom. Note that these effects begin to have an impact on images from image #201 onwards (>1 minute).

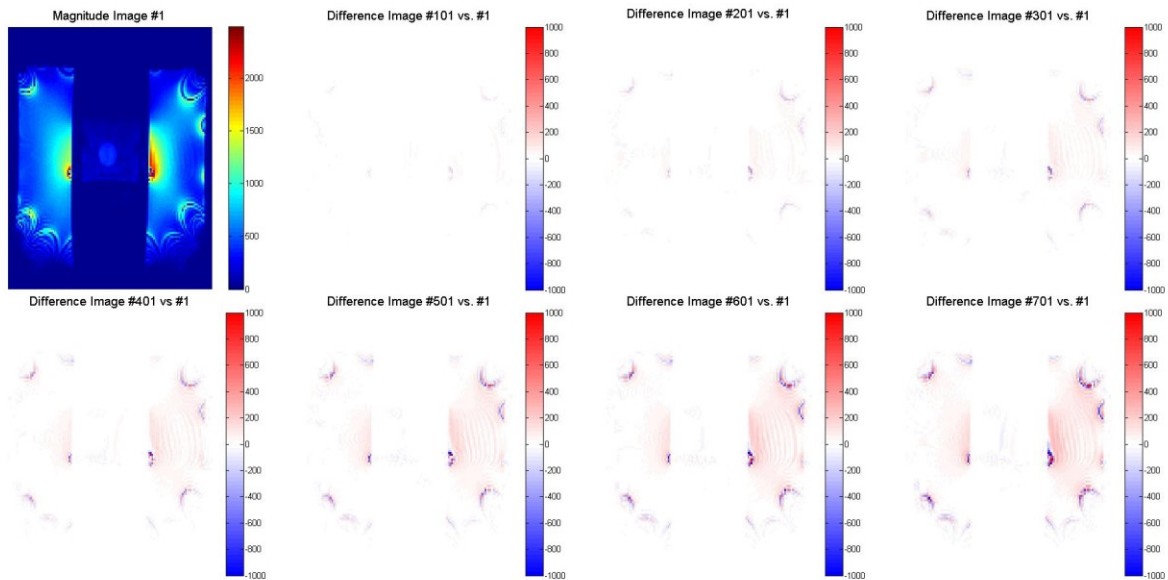


Figure 5-1 – Monitoring the change in bSSFP signal over time using the difference image. Top row, Column 1: initial magnitude image. Top row, Columns 2 – 4: difference image generated by subtracting images 101, 201, and 301 from the initial image. Bottom Row, Columns 1- 4: difference image generated by subtracting images 401, 501, 601, and 701 from the original image.

In the last chapter, PDACS is demonstrated to be superior to CS for dynamic images acquired within 1 minute prior data, but has reduced performance beyond that. While it is possible, in principle, to limit the dynamic scan acquisition to 1 minute, and then re-acquire the “prior data”, it will be inconvenient to perform this in the context of clinical workflow in practice. This is because the tumour tracking with the prediction algorithm<sup>80</sup> is best performed with images with a consistent frame rate. The re-acquiring of slower, fully sampled data may periodically stop the “tracking” dynamic and result in treatment interruptions. This chapter presents two specific aims: 1) Evaluate the negative impact on image quality of PDACS accelerated image reconstruction due to slow signal changes; and 2) Propose and test two sliding window strategies for PDACS reconstruction that continuously update the “prior data” as the dynamic scan progresses, without exclusive acquisition of the prior data.

## 5.2 Methods

### 5.2.1 Sliding Window Sampling Patterns

The crucial difference in the sliding window reconstruction is that, instead of repetitively using a single sampling pattern for all dynamic images (Figure 5-2, left), a series of different random patterns is used (Figure 5-3 right). These patterns cover different k-space sampling locations, such that whenever a k-space point is acquired, it will be used to “update” the pool of prior data, allowing it to be partially updated continuously. Unfortunately, the shape of the probability function often drops to near zero in the most peripheral regions, often results in a long time between updates of peripheral k-space points. In our new sampling strategy, k-space is separated into 3 regions. The very center of k-space (5 lines) is sampled with 100% probability. Next, the middle region is governed by the same polynomial function as suggested by Lustig et al. In the most peripheral region, arbitrarily defined as the region where  $p(k) < 0.25$ , we devised an iterative process to ensure that the limited sampling points here are temporally well spaced as shown in Figure 5-3. In the first iteration of this process, a uniform probability,  $p_{\text{peripheral}}$  is chosen such that,  $\sum p_{\text{central}} + \sum p_{\text{middle}} + \sum p_{\text{peripheral}}$  is equal to the constant total probability required for a particular degree of acceleration (i.e., for the fully sampled 128 k-lines, the total probability will ensure 64 and 32 k-space lines for 2x and 4x accelerations respectively). A sampling pattern is generated resulting in sampled locations,  $k_{s,1}$  and un-sampled location  $k_{us,1}$ . For the next pattern, in the peripheral region, the probability for the previously sampled location is reduced to zero to prevent those locations from being immediately resampled again, such that,  $p_2(k_{s,1}) = 0$ . However, this will result into decreased  $\sum p_{\text{peripheral}}$  by a certain amount. To maintain the constant total probability  $\sum p_{\text{peripheral}}$ , the probability of the un-sampled locations is increased uniformly, i.e.  $p_2(k_{us,1}) = p_1(k_{us,1}) + c_2$ , where  $c_2$  represents the lost probability equally redistributed to all un-sampled locations of the first iteration. Generally,  $p_{n+1}(k_{s,n}) = 0$ , and  $p_{n+1}(k_{us,n}) = p_1(k_{us,n}) + c_{n+1}$ . Note that any previously sampled location with lost probability will eventually become un-sampled and will have probability transferred back via the  $c_{n+1}$  term. This iterative sampling method eventually reaches a steady state that yields well distributed patterns (shown in Figure 5-3, right). PDACS and the sliding window PDACS (SWPDACS) patterns are generated for a

wide range of MR under-sampling/acceleration factors, 50%, 40%, 30%, 25%, 20% sampling which is equivalent to image acceleration of 2x, 2.5x, 3.3x, 4x, 5x.

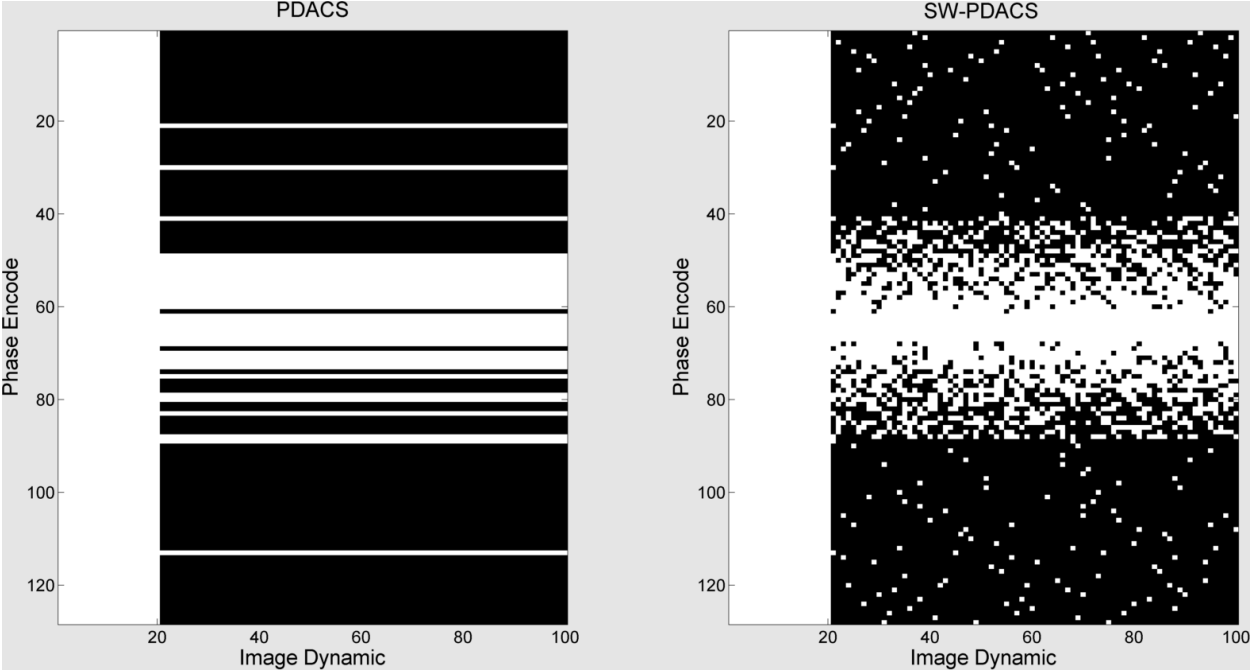


Figure 5-2 - Left: the original PDACS sampling pattern (25%) which uses identical sampling patterns for all image dynamic in which the non-sampled k-space locations are not updated, and the sliding window pattern in which all k-space locations are updated.

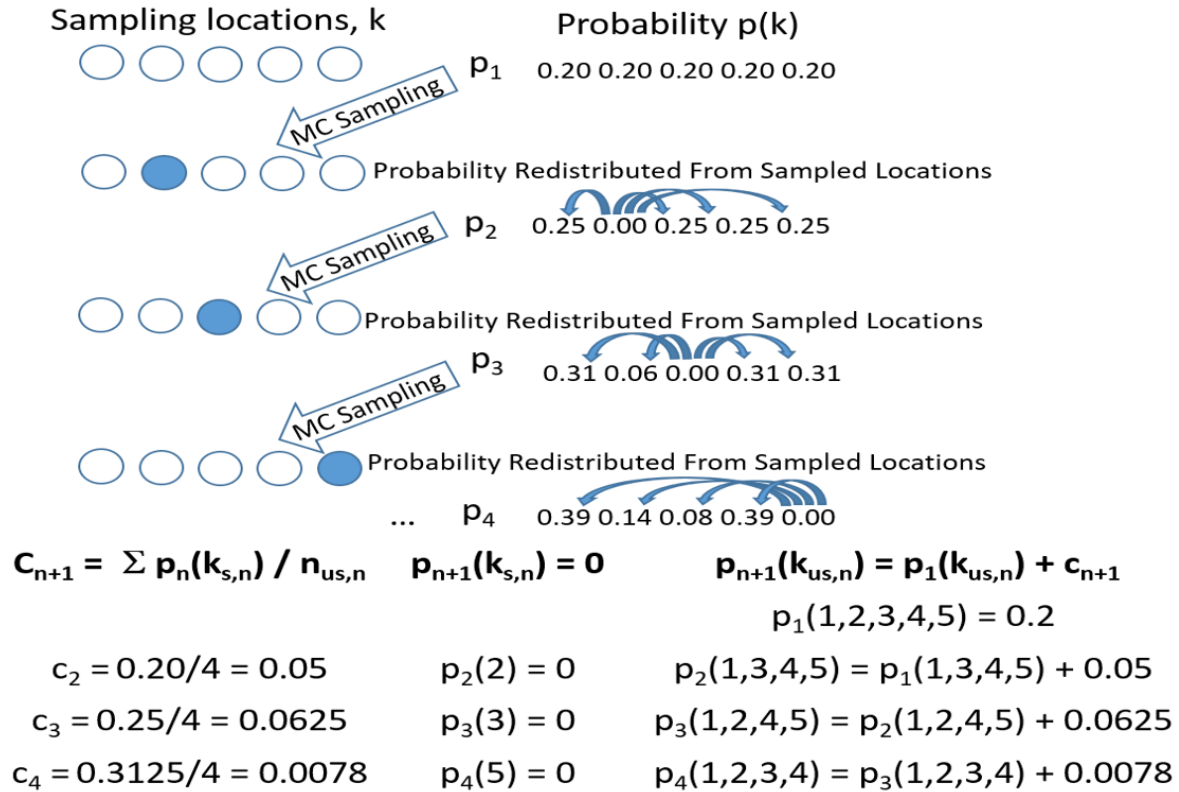


Figure 5-3 The probability redistribution process, applied in a simple case of 5 k-space locations, the algorithm starts with equal probability in all locations at  $p_1$  (0.2), the Monte Carlo process determines a sampling pattern from it, after which the probability from the sampled location is redistributed to the non-sampled location, resulting in probability distribution  $p_2$ . This process ensures good temporal spacing between sampling points while maintaining incoherent sampling required for Compressed Sensing.

### 5.2.2 Sliding Window Strategies 1 – Sliding Window Averaging

Two different schemes are proposed to select prior data  $\bar{D}$  from the window to improve reconstruction. The first method is a simple sliding average method where a sliding window of data is simply averaged as prior data (Figure 5-4, left). The window is first “pre filled” with the same 20 fully sampled images as it is in the PDACS method. As the scan progresses, additional data is added to the window until image #80, after that the window begins to slide, removing the oldest prior data from the window. From image #101 on, the window of 100 under-sampled images immediately prior to a particular dynamic is averaged as  $\bar{D}$  in equation 4.1. Note that with a sliding window implementation the “pre-filling” of the window with initial fully sampled prior data is not a necessity, as one can simply acquire 100 under-sampled frames to serve as prior data instead. Nevertheless, it is applied in this study to give the most straight forward comparison to the non-sliding method.

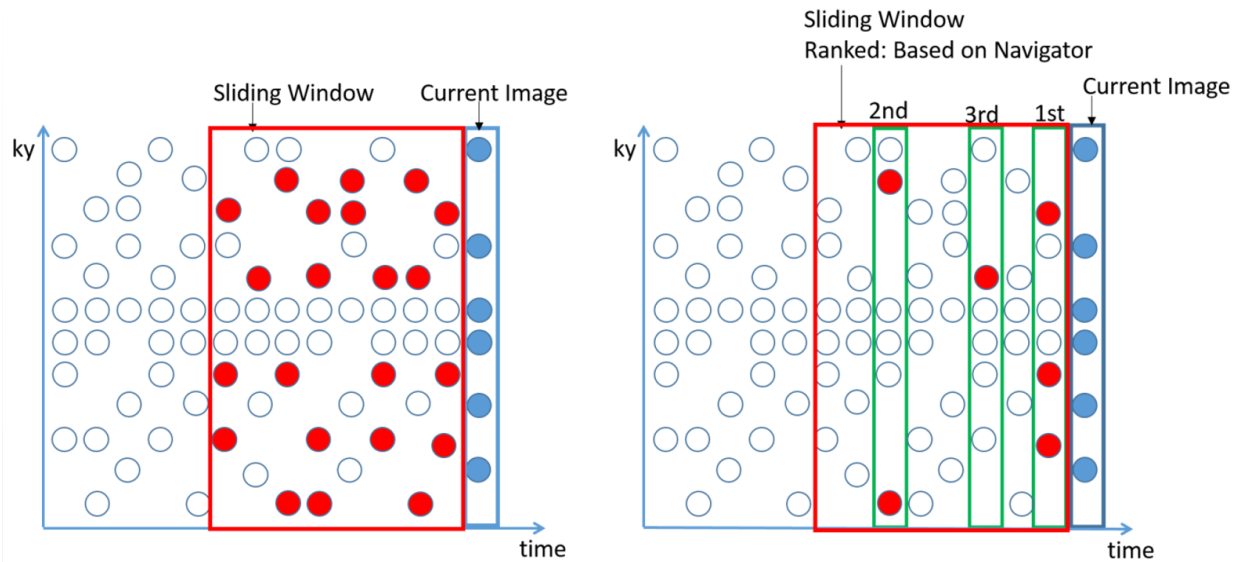


Figure 5-4 – Left – sliding window averaging method, each circle represents a k-space line. All data that corresponds to an unsampled location of current data (filled circle) is averaged and applied in reconstruction. Right – sliding window with navigator, the data within the sliding window is ranked based on navigator similarity – with the closest available match in each location used as prior data.

### 5.2.3 Sliding Window Strategies 2– Sliding Window with Navigator Guidance

The second proposed scheme is a navigator guided approach (Figure 5-4, right). It uses the same sliding window as described previously, but instead of averaging all the data in the window, it uses the data most closely matched to the current diaphragm position. The diaphragm position is quickly approximated by acquiring a navigator. In order to test this approach with the patient data that has been acquired previously, the central, superior-inferior k-space line is used as an intrinsic navigator. No additional navigator pulses are used. The 1D Fourier transform of the central k-space line is an anterior-posterior projection of the 2D sagittal image as shown in Figure 5-5.

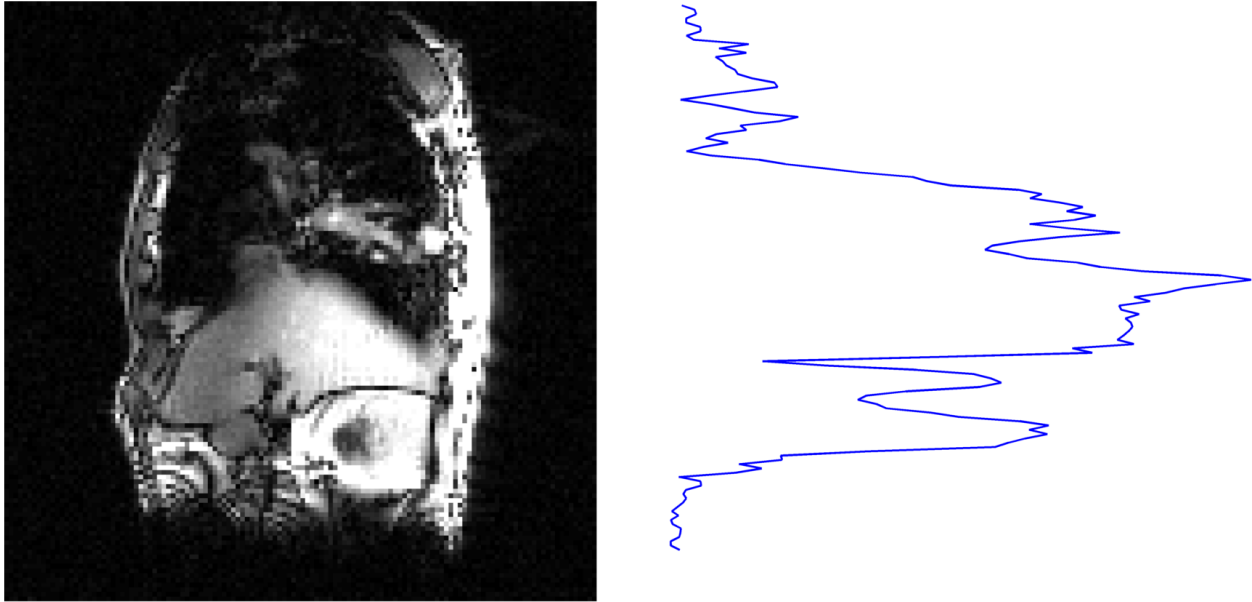


Figure 5-5 – Left, a 2D Fourier transform of the full k-space, Right, the equivalent profile resulted from a 1D FT of the central K-space line

As the diaphragm and other structures move throughout the breathing cycle, the navigator profile will shift accordingly; for every navigator profile after the first one, a 1D cross correlation operation is performed against first profile and the location of maximum correlation is determined. The location of maximum correlation will change during the breathing period. The maximum correlation location of the navigator profile is highly influenced by the diaphragm position in the breathing cycle, and is shown with the corresponding tumour position in Figure 5-6. The prior data,  $\bar{D}$ , is chosen from within the sliding window based on the closest available match to the current navigator position, such that reconstruction artifacts will be minimized. The additional computation of a 1D FFT for the navigator, a 1D cross correlation and data selection adds ~10ms of reconstruction time before 2D image reconstruction, but may reduce motion blurring<sup>81</sup> of the tumour associated with time averaged data in the prior image.

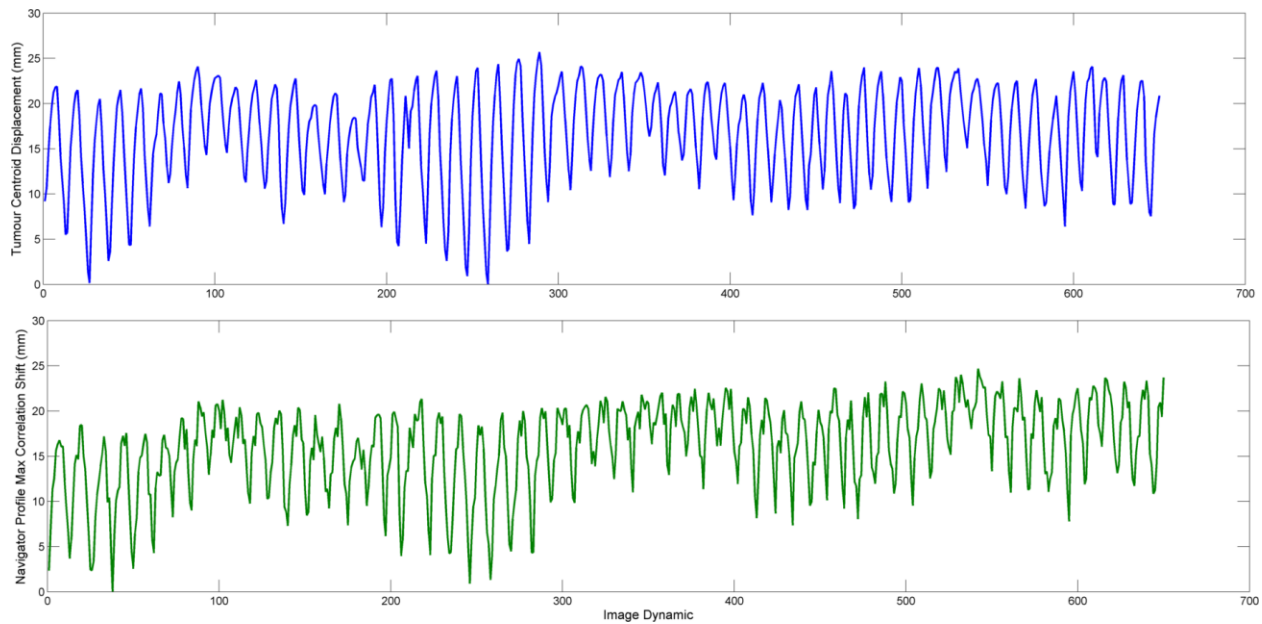


Figure 5-6- Actual tumour superior-inferior centroid position(top, blue) for a single patient as determined by contouring vs. approximate diaphragm position (bottom, green) as determined by the maximum correlation calculations of the navigator profiles.

### 5.2.4 Evaluating Decline in Image Quality due to the Outdated Prior Data

One of the main benefits of a sliding window reconstruction is that the prior data will be drawn from relatively recent acquisitions, which would reduce the impact of gradual changes in MR signal unrelated to breathing motion (i.e. due to MR signal drift or patient shifting position). For the PDACS reconstruction that uses the prior data acquired at the beginning of the scan series, the slow signal drift could lead to artifacts. In our analysis, the average of first 20 acquisitions is used as prior data, and the remaining 630 images are separated into 3 groups of 210 images (each representing  $\sim 1$  minute of breathing data). The 3 groups of data will be averaged separately for all the patients, in order to observe possible decline in image quality from the 1<sup>st</sup> to the 3<sup>rd</sup> group. Artifact power, Dice coefficient and centroid error for all patients are evaluated as described previously. Due to the less reliable tracking metrics for patient 5 shown in the validation study, it is excluded in the Dice's coefficient and centroid error analysis, but included in the artifact power analysis.

## 5.3 Results

### 5.3.1 Artifact Power – 3 T SNR

The average artifact power for the 3 image groups (images 1-210, 211 – 420 and 421-630) for 6 patients. MR acceleration factors from 2 – 5x, averaged across all patients, for 3 different image reconstruction methods is shown in the first row of Figure 5-7. For all methods, the image artifact power increases with the increasing acceleration factor. Please note that the ordinate scale is different for different acceleration factors in Figure 5-7. At each acceleration factor, without sliding window, the image artifact power shows a clear increasing trend as the dynamic scan progresses, as indicated by the increasing blue bar from image group 1 to 3 in the first row of Figure 5-7. This trend is not observed for both the average or navigator based sliding window methods, which have very similar performances between three image groups. The two sliding window techniques yield similar artifact power to each other. The non-sliding window performs similarly well to the sliding window methods in the first image group; however, in image groups 2 and 3, the two sliding window methods consistently yields lower artifact power compared to the non-sliding window technique. Image group 3 and 5x acceleration presents the most challenging scenario for the original non-sliding method, resulting in an artifact power of 0.065; however, the averaging and navigator sliding window approach reduce the artifact power to 0.030 and 0.031, respectively.

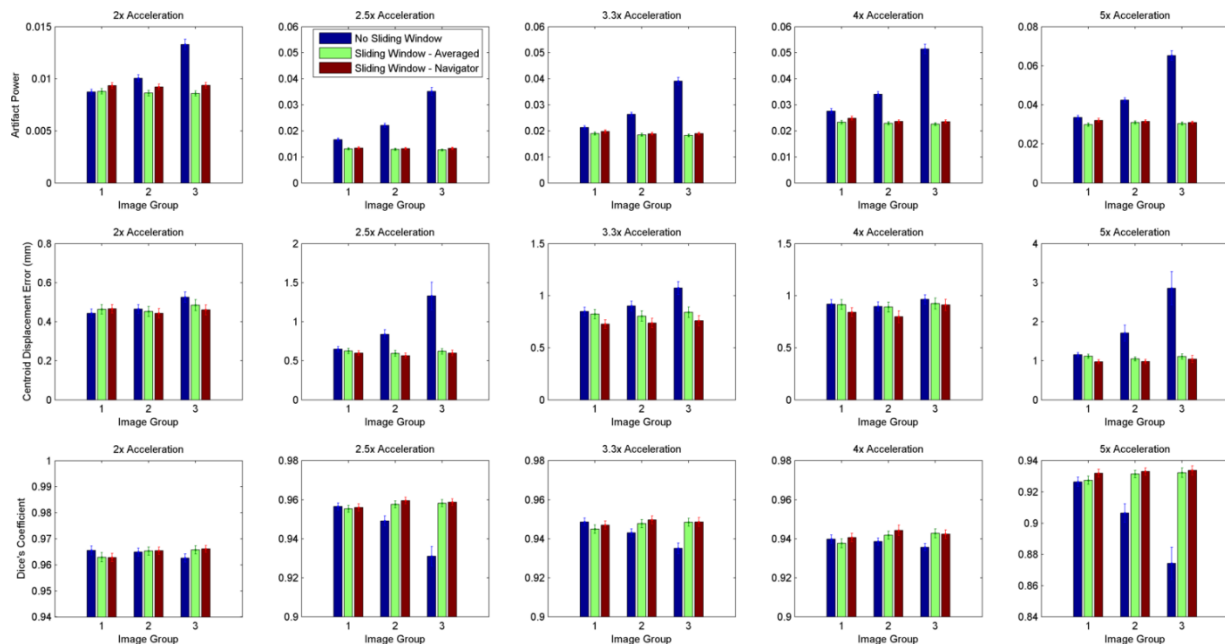


Figure 5-7 – Quantitative comparison of the 3 acceleration methods for 3 T images. First row, Artifact power for 2 – 5x acceleration are shown. Second Row: Centroid Displacement Error (in mm) is shown. Third row, Dice's Coefficients are shown. Image groups 1, 2, 3 represent a binned average of image 1-210, 211-420, 421 - 630. Error bars indicate 95% confidence intervals.

### 5.3.2 Tumour Tracking Error – 3 T SNR

The centroid displacement error and Dice coefficient are shown in rows 2 and 3 of Figure 5-7 respectively. For all acceleration factors except 4x, without using a sliding window, the centroid displacement error increases and Dice coefficient decreases from image groups 1 to 3, indicating a loss in tracking accuracy. The navigator sliding window yields marginally lower centroid displacement errors and higher Dice's coefficient compared averaged sliding method. At accelerations  $> 2x$ , the sliding window methods show improved performance and this is particular evident in the at 2.5 and 5x accelerations. In the most challenging scenario for the original non-sliding method, (i.e. image group 3 and 5x acceleration factor), the centroid displacement error reduces from 2.86 mm, without sliding window, to 1.11 mm (1.04 mm) with the averaging (navigator) sliding window implemented, while the Dice coefficient increases from 0.874, without sliding window to 0.932 (0.934).

### 5.3.3 Image Reconstruction Error – Pseudo 0.5T SNR

The results from the pseudo 0.5 T images are shown in the first row of Figure 5-8. The image reconstruction error is generally higher compared to the 3 T images due to the higher noise present in the data. There are several trends in the 0.5 T data that are similar to the 3 T data. Larger acceleration factors lead to larger image artifact powers for all methods. For a particular acceleration factor, without sliding window, there is a clear trend of increase in image artifact power as the dynamic scan progresses, i.e. from image group 1 to image group 3 as indicating in the first row of Figure 5-8. This trend is not observed for both the sliding average and navigator guided sliding window methods, which have very similar performances between groups, as indicated in the first row of Figure 5-8.

Unlike the original 3 T data, the navigator sliding window method (red bars) yields higher artifact powers compared to the sliding averaging method (green bars), as shown in Figure 5-8. The averaging sliding window method results in lower artifact power compared to the non-sliding window method, particularly in image groups 2 and 3. Again the case of group 3 and 5x acceleration presents most challenging scenario for the original non-sliding method, resulting in an artifact power of 0.110; however, the averaging and navigator sliding window approach reduce the artifact power to 0.0897 and 0.0985, respectively.

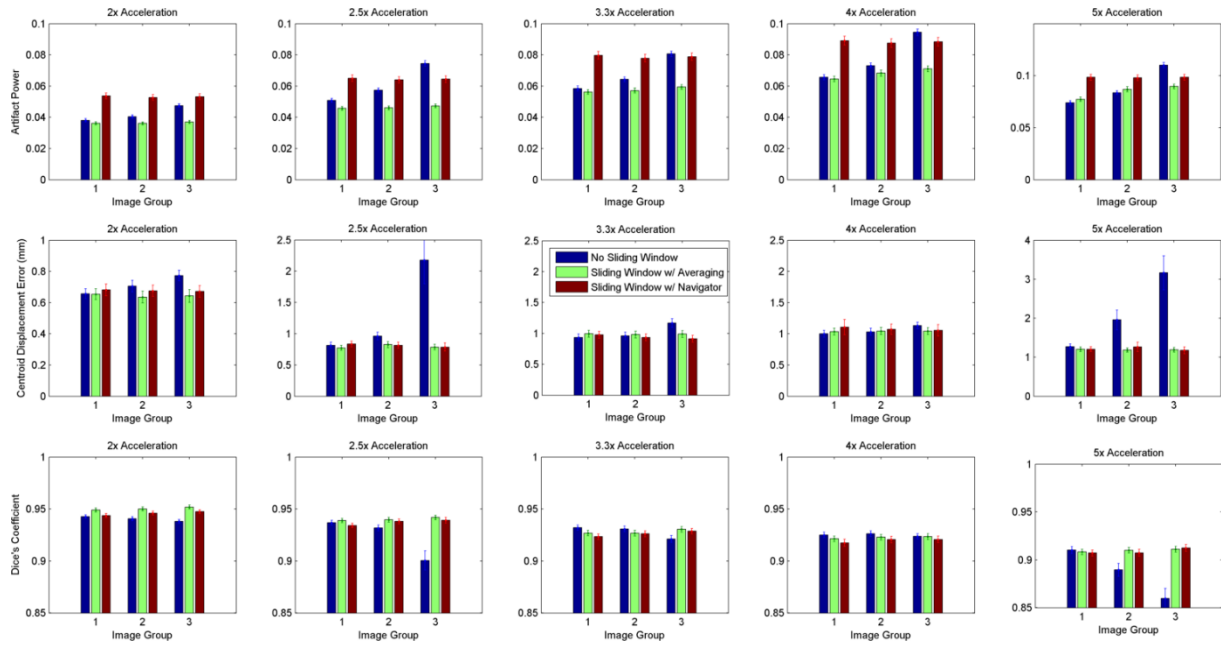


Figure 5-8 – Quantitative comparison of the 3 acceleration method for pseudo 0.5 T images. First row, Artifact power for 2 – 5x acceleration are shown. Second Row: Centroid Displacement Error (in mm) is shown. Third row, Dice’s Coefficients are shown. Image groups 1, 2, 3 represent a binned average of image 1-210, 211-420, 421-630. Error bars indicate 95% confidence intervals.

### 5.3.4 Tumour Tracking Error – pseudo 0.5T SNR

For the pseudo 0.5 T images, despite having a higher artifact power in the navigator based sliding window, the two sliding methods actually yield similar Dice coefficient and centroid displacement error with each other. Like the 3T data, the trends of reduced accuracy (increase in centroid error and decline in Dice coefficient) for outdated data of image groups 2 and 3 is observed in the 2.5x, 3x and 5x acceleration in Figure 5-8 (rows 2 and 3). The advantage of the sliding window methods is most pronounced in these cases. In the most challenging scenario for the original non-sliding method, (i.e. image group 3 and 5x acceleration factor), the centroid displacement error reduces from 3.16 mm, without sliding window, to 1.19 mm (1.17 mm) with the averaging (navigator sliding) window methods implemented, while the Dice coefficient increases from 0.859, without sliding window, to 0.911 (0.912).

### 5.3.5. Qualitative Example

The qualitative demonstration of the impact of outdated prior data, as well as the benefits of the sliding window methods are shown in Figure 5-9. Without a sliding window (Row 2), minimal artifacts are observed in group 1, but a progressive increase in artifact structures is observed in

groups 2 and 3. These artifacts are not observed in the sliding window reconstructed images.

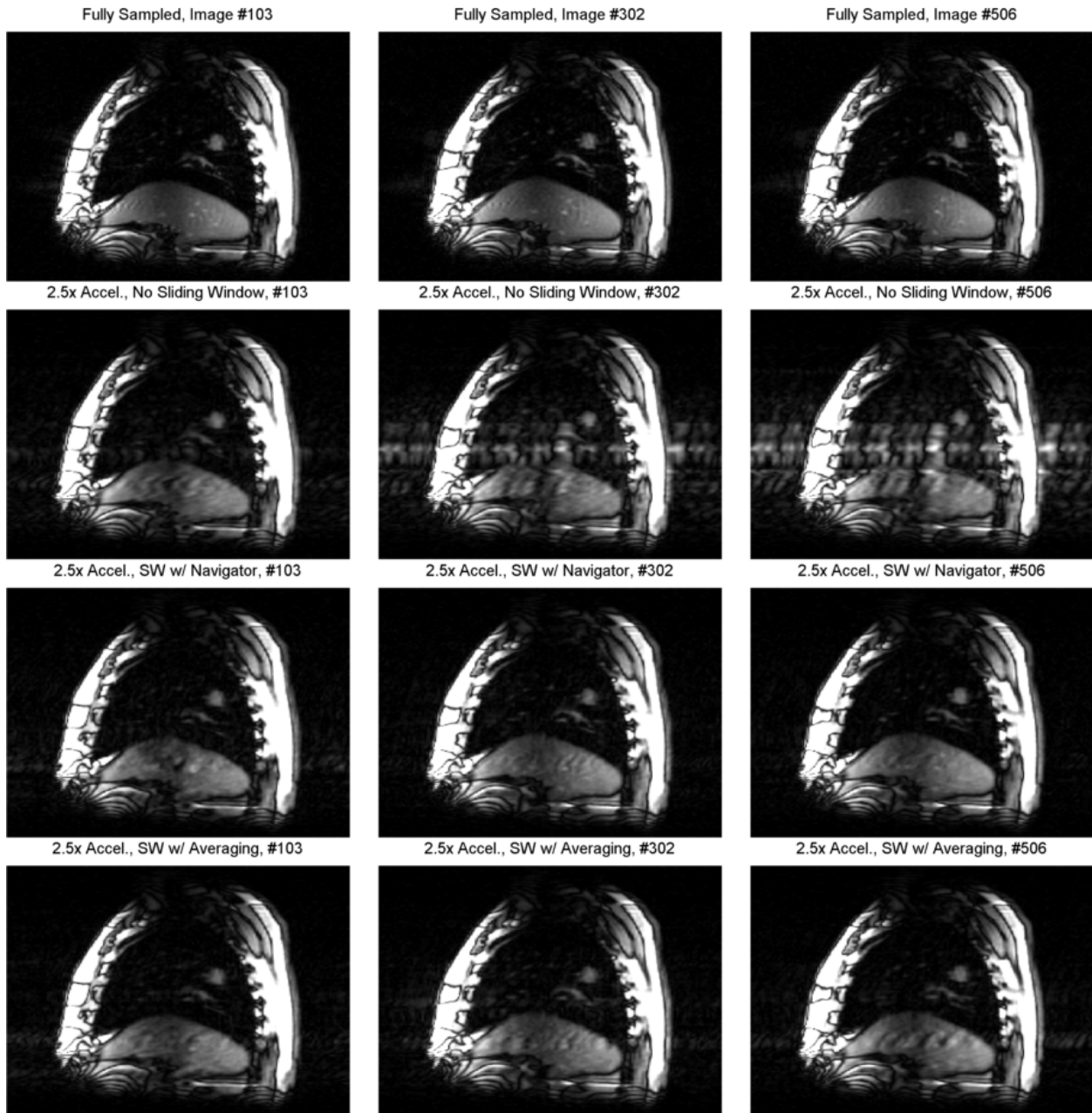


Figure 5-9 – Qualitative comparisons of representative images (chosen similar phase) from groups 1 in 3 (left to right). 2.5 accelerated images from Non Sliding window (row 2), Sliding window with navigator (row 3) and sliding window with averaging (row 4) are shown. Progressive increase in artifacts is easily observed in row 2, which are not observed in the sliding window methods.

## 5.4 Discussion

One of the objectives of this work is to evaluate the impact on PDACS reconstruction quality if prior data is not continuously updated. By separating the dynamic data into 3 groups, one can

observe a clear trend of increased image artifact power (Figures 5-7, 5-8, first row, blue bars). This trend is also clearly observed, in four of the five cases (2, 2.5, 3.3 and 5x acceleration), leading to poorer tumour tracking performance as the dynamic scan progresses (i.e. image groups 2 and 3) in the PDACS images (Figures 5-7, 5-8, second and third row), as the “prior data” gets progressively more outdated, this can also be observed qualitatively in Figure 5-9. The presence of these artifacts (Figure 5-9, row 2, column 2 and 3) indicate a limitation of the original PDACS implementation for longer duration (3 minute) dynamic scans. The original PDACS strategy of incorporating of prior data in CS (i.e. equation 4.1) has been shown to substantially improve standard CS (i.e. equation 2.99) reconstruction in our chapter, where prior data supports 1 minute of dynamic images. However, the results presented in this chapter, have revealed that incorporations of outdated prior data introduced additional artifacts to the images. The development of sliding window approach is therefore essential for implementation of PDACS in longer duration scans.

This trend of increasing artifact is greatly reduced by the two sliding window methods, at 3 T images in Figures 5-7 and by the sliding averaging method, in pseudo 0.5 T images, as shown in Figure 5-8. As shown in Figure 5.1, drift in MR signal that gradually builds up over time, possibly due to change in hardware temperature affecting  $B_0$ , (i.e., heating due rapid switching gradients<sup>79</sup>), any other form of slowly varying instability. Patient motion can also contribute to these signal drifts. While the exact cause is unknown, its effect can clearly be observed in the form of large incremental increases in artifact power of measured in the images of groups 2 and 3 in the non-sliding window results (Figure 5-7, Figure 5-8). The increase in disparity between the current data and prior data leads to a gradual increase in image artifact power that is reduced by a constantly updated pool of prior data in sliding window schemes.

It is worth noting that the global artifact power, which is often used in the literature as a measurement of the global image quality, does not always correlate to tumour tracking accuracy (Figures 5-7 and 5-8, 4x acceleration). This is because some artifacts may appear closer to the tumour (Figure 5-9, row 2, right) even though the global artifact power is small. These close by artifacts have a rather negative impact on tracking metrics compared to the distant ones such as the ones observed in the diaphragm area in the other accelerated images shown in Figure 5-9. Another interesting case showing the same effect is the pseudo 0.5T metrics (Figure 5-9) where

the navigator reconstructed images (red bar) have a larger artifact power than the averaging method (green bars), but the tracking metrics are comparable in both and better than the non-sliding window method (blue bars).. Figure 5-10 demonstrates a possible explanation of this effect. Both the navigator sliding window (left) and non-sliding window cases (right) have higher artifact power than the averaging sliding window case (center). However, in the navigator based sliding window case (left), these artifacts are random noise, where as in the non-sliding window case (right), these artifacts are structured and disruptive. The non-sliding window case therefore has lower tracking metrics compared to the other two cases. Although the global artifact power is easily computed, the two tumour tracking metrics are more relevant to the task of tumour tracking in dynamic images. However, there are several drawbacks of the tumour tracking metrics: 1) These metrics require a special algorithm for autocontouring and its validation. 2) These metrics are highly dependent on the type of autocontouring algorithm used, as a change in the contouring algorithm may lead to different results. Therefore, the combination of the two tumour tracking metrics and the overall artifact power gives a more complete picture of the reconstruction quality.

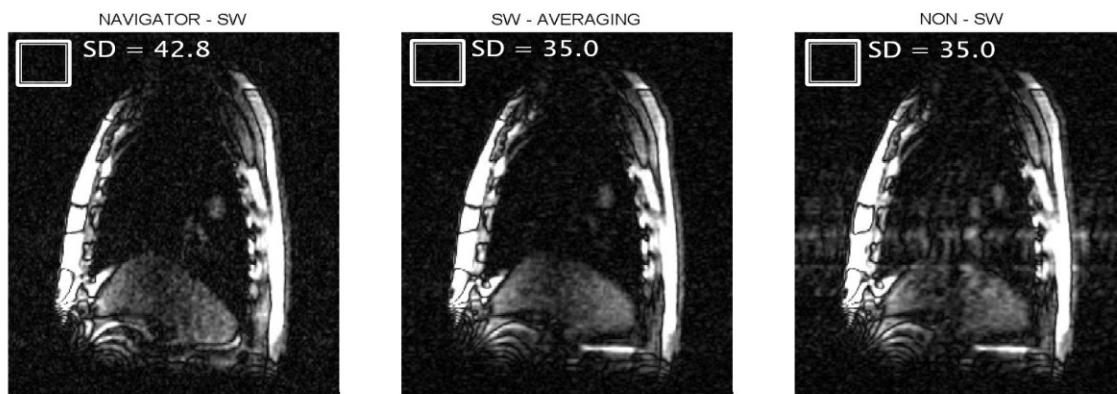


Figure 5-10 – Pseudo 0.5T image (#506) for the same patient shown in Figure 5-9 at 2.5x acceleration, reconstructed using sliding window with navigator (left), sliding window averaging (centre) and non-sliding window (right). Noise measurement is performed by calculating the standard deviation (SD) in the white box.

The pitfalls of using outdated prior data for reconstructing dynamic image series have been demonstrated in related techniques such as PICCS in CT imaging, and KEYHOLE in MRI. In CT imaging, PICCS<sup>74</sup> is a CS technique that relies on prior image and it also suffers from increased artifacts when the prior image is mis-registered with the under-sampled image<sup>82</sup>, and requires image registration to improve image quality. In MRI, analogous effects are observed in

prospective KEYHOLE imaging<sup>83</sup>, in which changes in image contrast lead to ringing artifacts due to discontinuous k-space between current and prior, reference data acquired at the beginning of a sequence. Similarly, we speculate that signal shifts may have occurred during our dynamic scans, leading to artifacts that are too coherent for the CS algorithm to remove (Figure 5-8, row 2).

It should be noted that the degree of signal drift over time may be dependent on the MR scanner and may not be the same for other MR systems (i.e. 0.5 T linac-MR). However, since the sliding window methods are relatively simple to implement, they provide a solution that continuously updates the prior data without stoppage or a change in frame rate. This would be particularly useful if the tracking scan has a long duration (> 1 minutes). In the context of radiation therapy, this could potentially include MR guided Stereotactic Body Radiation Therapy (SBRT), for which a much larger dose is given to the patient per fraction, requiring longer treatment times. Another example is the case MR guided gated treatment with a lower duty cycle. In these situations where longer scans are required, sliding window PDACS should be implemented in order to avoid unnecessary stoppages during treatment needed for re-acquisition of the prior data.

One interesting observation from our study is that the two proposed sliding window methods perform differently at different SNR levels. At 3 T SNR, the navigator guided method provides similar artifact power to average based method, but performs marginally better in terms centroid error (Figure 5-7, rows 2). Since the navigator chooses the prior data with the closest matched to the current dynamic image data, it may reduce the effect of motion blurring<sup>81</sup> in the prior data obtained with time averaging. With a dedicated navigator pulse, or an external navigator signal (i.e., respiratory belt) the benefits of the navigator could be further enhanced.

At pseudo 0.5 T, however, the navigator based approach leads to higher global artifacts, but similar tracking accuracy is achieved compared to the averaged sliding window method. (Figure 5-8). The ability of the CS algorithm to suppress artifacts is dependent on its ability to distinguish signal (high intensity) from incoherent artifacts/noise (low intensity)<sup>47</sup>. The presence of higher intensity noise therefore makes it more difficult for the algorithm to distinguish artifacts from signal. Unlike the navigator process which only uses one sample from the window (Figure 5-4, right), the averaging of many samples (Figure 5-4, left), has the effect of reducing the added noise, as noise is proportional to  $1/\sqrt{N}$ , where N is the number of samples averaged.

The increase in global artifacts may have counteracted any benefit in tracking accuracy from reduced motion blurring.

One must be cautious in interpreting the results of the pseudo 0.5 T data, which is meant to serve as a “worst case scenario” for 0.5 T performance, due to all the un-accounted factors discussed previously in section 4.4. The use of a dedicated navigator pulse, or an external navigator independent of SNR (i.e. respiratory belt) may improve performance for the navigator method at lower fields. With all these caveats, it may be premature to rule out the use of navigators at 0.5 T. Nevertheless, despite being a worst case scenario, we have presented a workable solution (sliding window with averaging) for PDACS acceleration at lower fields.

One of the motivations for developing a CS based strategy such as PDACS is the ability to accelerated k-space acquisition without specialized hardware (i.e. phase array coil and multiple receive channels), which may not be available or practical in some situations. The algorithm is therefore designed to operate on either single coil data or combined coil data from a phase array coil. In our study, the data from individual coils is combined by the manufacturer’s software to serve as the starting point of our study, essentially mimicking a single channel volume coil. The methods of combining data from individual coils, as implemented in the MRI system software, may affect the image SNR. To demonstrate our algorithm’s validity with raw coil data, we performed an additional scan with a healthy volunteer. In addition to the scanner reconstructed data, PDACS was performed on raw coil data from individual coils after a simple k-space phase normalization and summation. Please note this rudimentary coil combination strategy represents a non-optimal, worst case scenario in terms of SNR<sup>84</sup>. Compared to scanner reconstructed data, raw coil data from the individual channels resulted in reconstructed images with marginally larger artifact power from PDACS reconstruction, due to the reduced SNR. The loss in SNR may be recovered using more sophisticated coil combination strategies<sup>84</sup>, which is beyond the scope of our work. Nevertheless, this does not alter the utility of our algorithm as it has been demonstrated to work for a range of SNR values in this study.

## 5.5 Summary

Prior data assisted compressed sensing (PDACS) can improve compressed sensing reconstruction of dynamic scans by adding in prior data acquired at the beginning of a dynamic scan series, but the quality of the prior data can have a considerable impact on the reconstructed

image quality. In this chapter we demonstrated the negative impact of slow changes in MR signal in longer duration PDACS dynamic scans, which consists of increases in image artifact power and reductions in tumour tracking accuracy. A sliding window approach, using either sliding averaging at 0.5 T or preferably a navigator guided approach at 3.0 T, are solutions that allow prior data to be continuously updated. These schemes are preferred in dynamic MR tracking with durations of  $> 1$  minute, as they reconstruct images with lower artifact power and higher tracking accuracy.

## Chapter 6 Conclusions and Future Direction

This thesis describes the development and evaluation of a novel image reconstruction strategy, Prior Data Assisted Compressed Sensing or PDACS, which takes advantage of the previously acquired data to speed up the dynamic MR acquisition. It was shown in our retrospective study that at acceleration factors greater than 2x, PDACS substantially improves the image quality compared to the conventional 2D CS reconstruction. MR acquisition ultimately represents a trade-off between imaging speed and imaging quality measured in terms of image noise and/or resolution. PDACS, which incorporates the prior data and the regularized reconstruction, significantly reduces the loss of image quality from increasing acquisition speed, producing accurate images at 5x acceleration.

The original PDACS method, presented in Chapter 4, is reliant on a stable baseline signal to be averaged into the prior data, however, this has shown to be problematic in the longer duration scans (> 1minute) where a shift in bSSFP signal can be observed. In our patient study, this led to a decline of the image quality. In these cases, the sliding window implementation of PDACS, shown in Chapter 5, ensures the highest quality images.

Our experimental results of Chapter 3 support the first hypothesis that the auto-contouring algorithm is capable of auto-segmentation of tumour in the real-time MR images. In the phantom images, these contours are comparable to a gold standard in terms of tracking performance indicators: Dice's coefficient and centroid positions. In the patient images, the algorithm gives metrics comparable to the intra and inter observer variability. In chapter 4, our experimental results support the second hypothesis that the inclusion of motion averaged prior data in compressed sensing improves image quality compared to the conventional compressed sensing, in terms of the artifact power, auto-contouring Dice's coefficient and centroid displacement error. Finally, in chapter 5, our experimental results support the third hypothesis; an algorithm which constantly refreshes the prior data pool using more recent data improves compressed sensing image quality in terms of indicators stated above, especially for the longer dynamic scans. However the 2<sup>nd</sup> and 3<sup>rd</sup> hypotheses are only tested in retrospective studies. These algorithms need ultimately to be tested in the prospective real-time imaging of lung tumour patients.

Translating the PDACS method from an off-line, retrospective study to an on line, prospective approach, that is useful for tracking tumours on the Linac-MR, is suggested as a subject of future research. Some of the technical challenges include the implementation and integration of software required for the acquisition of pseudo-random k-space lines, PDACS reconstruction, auto-contouring, and MLC movement to tracked tumour position. Overcoming these challenges in the on-line implementation of this approach will allow the ultimate validation of our technique and assessment of the benefits of these methods in actual clinical practice.

Further investigation is required to determine how to best take advantage of the reduced k-space acquisition time. In addition to the obvious benefit of increased frame rate, another possible application of acceleration is in the acquisition of multiple (orthogonal) slices while maintaining a similar frame rate (4 fps). In the tumour tracking scenarios presented in this thesis, the BEV is assumed to be a sagittal plane. If that is the case, relevant motion will be captured and the benefit or additional information from orthogonal slices will be limited. However, there may be cases in which BEV is in an oblique plane that may have anatomy close to the tumour which makes it difficult to image. In that scenario, imaging in multiple planes may become necessary to capture the motion required for tumour tracking.

While one of the advantages of CS based strategies is that it is not reliant on multiple-channel coils, if available, numerous studies have indicated that coil sensitivity information and multiple coil data may be incorporated into CS reconstruction to improve image reconstruction and/or acceleration. The feasibility of incorporating parallel acquisition into PDACS warrants further investigation, with the potential benefits of enhanced acceleration/image quality to be weighed against potential increases in reconstruction time, which may make the technique less suitable for real time tracking.

For further acceleration, one could look into a potentially sacrifice of the image quality of less important anatomical regions, without compromising the image quality in the regions near the tumour. In terms of the Cartesian imaging, we could, in principle, acquire images with significant fold-over artifacts, as long as the artifact does not overlap with the anticipated tumour region of the image. In radial sampling, under-sampling leads to streaking artifacts, which tend to be a more benign artifact for the purpose of tumour tracking<sup>33</sup>. Radial acquisition also has the advantage of being less sensitive to motion artifacts<sup>33</sup>. However, the disadvantage of radial

imaging is that it covers k-space in a less efficient manner, and requires gridding reconstruction<sup>33</sup>, which is slower compared to FFT.

Despite all these acceleration techniques, true real time 4D MR imaging, in which data acquisition and reconstruction are done in real time, may not be possible at 4 fps in the foreseeable future. A combination of pre-treatment, non-real time 4D imaging (i.e. with retrospective sorting), in combination of real time, accelerated 2D imaging during treatment may be best application of current Linac-MR technology for the real time tracking of tumours.

## References

1. Canadian Cancer Society's Advisory Committee on Cancer Statistics. *Canadian cancer statistics 2015*. Canadian Cancer Society; 2015.
2. Thomson G, Young, YK. *Cancer in Canada - framing the crisis and previewing the opportunity for donors*. Charity Intelligence Canada; 2009.
3. Van Dyk J. *The modern technology of radiation oncology: A compendium for medical physicists and radiation oncologists*. Medical Physics Pub Corp; 1999.
4. Ravichandran R. Has the time come for doing away with cobalt-60 teletherapy for cancer treatments. *J Med Phys*. 2009;34(2):63-65.
5. Brahme A, Roos J, Lax I. Solution of an integral equation encountered in rotation therapy. *Phys Med Biol*. 1982;27(10):1221.
6. Convery DJ, Rosenbloom ME. The generation of intensity-modulated fields for conformal radiotherapy by dynamic collimation. *Phys Med Biol*. 1992;37(6):1359.
7. International Commission of Radiation Units and Measurements. *ICRU report 50, prescribing, recording and reporting photon beam therapy*. ICRU; 1993.
8. International Commission of Radiation Units and Measurements. *ICRU report 62, prescribing, recording and reporting photon beam therapy*. ICRU; 1999.
9. International Commission of Radiation Units and Measurements. *ICRU report 71, prescribing, recording and reporting electron beam therapy*. ICRU; 2004.

10. Dawson LA, Jaffray DA. Advances in image-guided radiation therapy. *J Clin Oncol*. 2007;25(8):938-946.
11. Langen K, Jones D. Organ motion and its management. *Int J Radiat Oncol Biol Phys*. 2001;50(1):265-278.
12. Rodgers MS, Collinson R, Desai S, Stubbs RS, McCall JL. Risk of dissemination with biopsy of colorectal liver metastases. *Dis Colon Rectum*. 2003;46(4):454-458.
13. Haddad FS, Somsin AA. Seeding and perineal implantation of prostatic cancer in the track of the biopsy needle: Three case reports and a review of the literature. *J Surg Oncol*. 1987;35(3):184-191.
14. Verellen D, De Ridder M, Linthout N, Tournel K, Soete G, Storme G. Innovations in image-guided radiotherapy. *Nat Rev Cancer*. 2007;7(12):949-960.
15. Cheng C, Wong J, Grimm L, Chow M, Uematsu M, Fung A. Commissioning and clinical implementation of a sliding gantry CT scanner installed in an existing treatment room and early clinical experience for precise tumor localization. *J Clin Oncol*. 2003;26(3):e28-e36.
16. Jaffray DA, Siewerdsen JH, Wong JW, Martinez AA. Flat-panel cone-beam computed tomography for image-guided radiation therapy. *Int J Radiat Oncol Biol Phys*. 2002;53(5):1337-1349.
17. Mackie TR, Kapatoes J, Ruchala K, et al. Image guidance for precise conformal radiotherapy. *Int J Radiat Oncol Biol Phys*. 2003;56(1):89-105.

18. Mutic S, Dempsey JF. The ViewRay system: Magnetic resonance guided and controlled radiotherapy. *Semin Radiat Oncol*. 2014;24(3):196.
19. Crijs S, Raaymakers B. From static to dynamic 1.5T MRI-linac prototype: Impact of gantry position related magnetic field variation on image fidelity. *Phys Med Biol*. 2014;59(13):3241.
20. Fallone BG. The rotating biplanar linac magnetic resonance imaging system. *Semin Radiat Oncol*. 2014;24(3):200.
21. Walter C, Boda-Heggemann J, Wertz H, et al. Phantom and in-vivo measurements of dose exposure by image-guided radiotherapy (IGRT): MV portal images vs. kV portal images vs. cone-beam CT. *Radiother Oncol*. 2007;85(3):418-423.
22. Keall PJ, Mageras GS, Balter JM, et al. The management of respiratory motion in radiation oncology report of AAPM task group 76. *Med Phys*. 2006;33(10):3874-3900.
23. Lagerwaard FJ, de Koste, John R Van Sornsen, Nijssen-Visser MR, et al. Multiple “slow” CT scans for incorporating lung tumor mobility in radiotherapy planning. *Int J Radiat Oncol Biol Phys*. 2001;51(4):932-937.
24. Underberg RW, Lagerwaard FJ, Slotman BJ, Cuijpers JP, Senan S. Use of maximum intensity projections (MIP) for target volume generation in 4DCT scans for lung cancer. *Int J Radiat Oncol Biol Phys*. 2005;63(1):253-260.
25. Hanley J, Debois MM, Mah D, et al. Deep inspiration breath-hold technique for lung tumors: The potential value of target immobilization and reduced lung density in dose escalation. *Int J Radiat Oncol Biol Phys*. 1999;45(3):603-611.

26. Willoughby TR, Kupelian PA, Pouliot J, et al. Target localization and real-time tracking using the calypso 4D localization system in patients with localized prostate cancer. *Int J Radiat Oncol Biol Phys.* 2006;65(2):528-534.
27. Shah AP, Kupelian PA, Waghorn BJ, et al. Real-time tumor tracking in the lung using an electromagnetic tracking system. *Int J Radiat Oncol Biol Phys.* 2013;86(3):477-483.
28. Adler Jr JR, Chang S, Murphy M, Doty J, Geis P, Hancock S. The cyberknife: A frameless robotic system for radiosurgery. *Stereotact Funct Neurosurg.* 1997;69(1-4):124-128.
29. Depuydt T, Verellen D, Haas O, et al. Geometric accuracy of a novel gimbals based radiation therapy tumor tracking system. *Radiother Oncol.* 2011;98(3):365-372.
30. Yun J, Yip E, Gabos Z, Wachowicz K, Rathee S, Fallone BG. Neural-network based autocontouring algorithm for intrafractional lung-tumor tracking using linac-MR. *Med Phys.* 2015;42(5):2296-2310.
31. Nishimura DG. *Principles of magnetic resonance imaging.* Lulu.com; 2010.
32. Xiang Q. *University of British Columbia Physics 542 Course Notes.* 2007.
33. Bernstein BA, King, K.F., Zhou, X.A.. *Handbook of MRI pulse sequences.* Elsevier Inc.; 2004.
34. Scheffler K, Hennig J. Is TrueFISP a gradient-echo or a spin-echo sequence? *Magn Reson Med.* 2003;49(2):395-397.

35. Gudbjartsson H, Patz S. The rician distribution of noisy MRI data. *Magn Reson Med*. 1995;34(6):910-914.
36. Redpath PW. Signal-to-noise ratio in MRI. *Br J Radiol*. 1998;71(847):704-707.
37. Bottomley PA, Hardy CJ, Argersinger RE, Allen-Moore G. A review of 1-H nuclear magnetic resonance relaxation in pathology: Are T1 and T2 diagnostic? *Med Phys*. 1987;14(1):1-
38. Levitt MH. *Spin dynamics: Basics of nuclear magnetic resonance*. John Wiley & Sons; 2001.
39. Hutchinson M, Raff U. Fast MRI data acquisition using multiple detectors. *Magn Reson Med*. 1988;6(1):87-91.
40. Kwiat D, Einav S, Navon G. A decoupled coil detector array for fast image acquisition in magnetic resonance imaging. *Med Phys*. 1991;18(2):251-265.
41. Pruessman K, Weigner M, Scheidegger M, Boesiger P. SENSE: Sensitivity encoding for fast MRI. *Magn Reson Med*. 1999;42:952-962.
42. Sodickson DK, Manning WJ. Simultaneous acquisition of spatial harmonics (SMASH): Fast imaging with radiofrequency coil arrays. *Magn Reson Med*. 1997;38(4):591-603.
43. Jakob PM, Grisowld MA, Edelman RR, Sodickson DK. AUTO-SMASH: A self-calibrating technique for SMASH imaging. *Magn Reson Mater Phy*. 1998;7(1):42-54.
44. Heidemann RM, Griswold MA, Haase A, Jakob PM. VD-AUTO-SMASH imaging. *Magn Reson Med*. 2001;45(6):1066-1074.

45. Griswald M, Jakob P, Heidemann R, et al. Generalized autocalibrating partially parallel acquisitions (GRAPPA). *Magn Reson Med.* 2002;47:1202-1210.
46. Blaimer M, Breuer F, Mueller M, Heidemann RM, Griswold MA, Jakob PM. SMASH, SENSE, PILS, GRAPPA: How to choose the optimal method. *Top Magn Reson Imaging.* 2004;15(4):223-236.
47. Lustig M, Donoho D, Pauly J. Sparse MRI: The application of compressed sensing for rapid MR imaging. *Magn Reson Med.* 2007;58:1182-1195.
48. Donoho D. Compressed Sensing IEEE trans. inf. theory. *IEEE Trans Inf Theory.* 2006;52:1289-1306.
49. Yuan M, Yang B, Ma Y, Zhang J, Zhang R, Zhang C. Compressed sensing MRI reconstruction from highly undersampled-space data using nonsubsampling shearlet transform sparsity prior. *Math Probl Eng.* 2015;2015.
50. Qu X, Zhang W, Guo D, Cai C, Cai S, Chen Z. Iterative thresholding compressed sensing MRI based on contourlet transform. *Inverse Probl Sci Eng.* 2010;18(6):737-758.
51. Kim Y, Narayanan SS, Nayak KS. Accelerated three-dimensional upper airway MRI using compressed sensing. *Magn Reson Med.* 2009;61(6):1434-1440.
52. Goldstein T, Osher S. The split bregman method for L1-regularized problems. *SIAM J Imaging Sci.* 2009;2:323-343.

53. Tsao J, Kozerke S. MRI temporal acceleration techniques. *J Magn Reson Imaging*. 2012;36(3):543-560.
54. Riederer SJ, Tasciyan T, Farzaneh F, Lee JN, Wright RC, Herfkens RJ. MR fluoroscopy: Technical feasibility. *Magn Reson Med*. 1988;8(1):1-15.
55. van Vaals J, Brummer M, Dixon W. "Keyhole" method for accelerating imaging of contrast agent uptake. *J Magn Reson Imaging*. 1993;3:671-675.
56. Korosec FR, Frayne R, Grist TM, Mistretta CA. Time-resolved contrast-enhanced 3D MR angiography. *Magn Reson Med*. 1996;36(3):345-351.
57. Kellman P, Epstein FH, McVeigh ER. Adaptive sensitivity encoding incorporating temporal filtering (TSENSE). *Magn Reson Med*. 2001;45(5):846-852.
58. Breuer FA, Kellman P, Griswold MA, Jakob PM. Dynamic autocalibrated parallel imaging using temporal GRAPPA (TGRAPPA). *Magn Reson Med*. 2005;53(4):981-985.
59. Madore B, Glover GH, Pelc NJ. Unaliasing by fourier-encoding the overlaps using the temporal dimension (UNFOLD), applied to cardiac imaging and fMRI. *Magn Reson Med*. 1999;42(5):813-828.
60. Tsao J, Boesiger P, Pruessmann KP. K-t BLAST and k-t SENSE: Dynamic MRI with high frame rate exploiting spatiotemporal correlations. *Magn Reson Med*. 2003;50(5):1031-1042.
61. Lustig M, Santos J, Donoho D, Pauly J. K-T SPARSE: High frame rate dynamic MRI exploiting spaatial-temporal sparsity. *Proc to ISMRM*. 2006:2420.

62. Jung H, Sung K, Nayak K, Kim E, Ye J. K-t FOCUSS: A general compressed sensing framework for high resolution dynamic MRI. *Magn Reson Med.* 2009;61:103-116.
63. Lingala S, Hu Y, DiBella E, Jacob M. Accelerated dynamic MRI exploiting sparsity and low-rank structure: K-t SLR. *IEEE Trans Med Imaging.* 2011;30:1042-1054.
64. Feng L, Axel L, Chandarana H, Block KT, Sodickson DK, Otazo R. XD-GRASP: Golden-angle radial MRI with reconstruction of extra motion-state dimensions using compressed sensing. *Magn Reson Med.* 2016;75(2):775-788.
65. Yun J, Yip E, Wachowicz K, et al. Evaluation of a lung tumor autocontouring algorithm for intrafractional tumor tracking using low-field MRI: A phantom study. *Med Phys.* 2012;39(3):1481-1494.
66. Otsu N. A threshold selection method from gray-level histograms. *Automatica.* 1975;11(285-296):23-27.
67. Och JG, Clarke GD, Sobol WT, Rosen CW, Mun SK. Acceptance testing of magnetic resonance imaging systems: Report of AAPM nuclear magnetic resonance task group no. 6. *Med Phys.* 1992;19(1):217-229.
68. Hatabu H, Alsop DC, Listerud J, Bonnet M, Geftter WB. T2\* and proton density measurement of normal human lung parenchyma using submillisecond echo time gradient echo magnetic resonance imaging. *Eur J Radiol.* 1999;29(3):245-252.
69. Schmidt HC, Tscholakoff D, Hricak H, Higgins CB. MR image contrast and relaxation times of solid tumors in the chest, abdomen, and pelvis. *J Comput Assist Tomogr.* 1985;9(4):738-748.

70. Suh Y, Dieterich S, Cho B, Keall PJ. An analysis of thoracic and abdominal tumour motion for stereotactic body radiotherapy patients. *Phys Med Biol*. 2008;53(13):3623.
71. Kiricuta IC, Jr, Simplaceanu V. Tissue water content and nuclear magnetic resonance in normal and tumor tissues. *Cancer Res*. 1975;35(5):1164-1167.
72. Louie AV, Rodrigues G, Olsthoorn J, et al. Inter-observer and intra-observer reliability for lung cancer target volume delineation in the 4D-CT era. *Radiother Oncol*. 2010;95(2):166-171.
73. Bjerre T, Crijiins S, Rosenschold P, et al. Three-dimensional MRI-linac intra-fraction guidance using multiple orthogonal cine-MRI planes. *Phys Med Bio*. 2013;58:4943-4950.
74. Chen G, Tang J, Leng S. Prior image constrained compressed sensing (PICCS): A method to accurately reconstruct dynamic CT images from highly undersampled projection data sets. *Med Phys*. 2008;35(2):660-663. doi: <http://dx.doi.org/10.1118/1.2836423>.
75. Chan RW, Ramsay EA, Cheung EY, Plewes DB. The influence of radial undersampling schemes on compressed sensing reconstruction in breast MRI. *Magn Reson Med*. 2012;67(2):363-377.
76. Santos JM, Cunningham CH, Lustig M, et al. Single breath-hold whole-heart MRA using variable-density spirals at 3t. *Magn Reson Med*. 2006;55(2):371-379.
77. Bernstein MA, Huston J, Ward HA. Imaging artifacts at 3.0 T. *J Magn Reson Imaging*. 2006;24(4):735-746.

78. Yip E, Yun J, Wachowicz K, et al. Prior data assisted compressed sensing: A novel MR imaging strategy for real time tracking of lung tumors. *Med Phys*. 2014;41(8):082301.
79. El-Sharkawy AM, Schar M, Bottomley PA, Atalar E. Monitoring and correcting spatio-temporal variations of the MR scanner's static magnetic field. *Magn Reson Mater Phy*. 2006;19(5):223-236.
80. Yun J, Wachowicz K, Mackenzie M, Rathee S, Robinson D, Fallone B. First demonstration of intrafractional tumor-tracked irradiation using 2D phantom MR images on a prototype linac-MR. *Med Phys*. 2013;40(5):051718.
81. Wang Y, Riederer SJ, Ehman RL. Respiratory motion of the heart: Kinematics and the implications for the spatial resolution in coronary imaging. *Magn Reson Med*. 1995;33(5):713-719.
82. Nett B, Tang J, Aagaard-Kienitz B, Rowley H, Chen G. Low radiation dose C-arm cone-beam CT based on prior image constrained compressed sensing (PICCS): Including compensation for image volume mismatch between multiple data acquisitions. *Proc SPIE*. 2009; 725803.
83. Bishop JE, Santyr GE, Kelcz F, Plewes DB. Limitations of the keyhole technique for quantitative dynamic contrast-enhanced breast MRI. *J Magn Reson Imaging*. 1997;7(4):716-723.
84. Roemer PB, Edelstein WA, Hayes CE, Souza SP, Mueller O. The NMR phased array. *Magn Reson Med*. 1990;16(2):192-225.